

# **PARTICLE-LADEN FLUIDS: FUNDAMENTALS AND ENGINEERING APPLICATIONS**

A Dissertation  
Presented to  
The Academic Faculty

by

Qi Liu

In Partial Fulfillment  
of the Requirements for the Degree  
Doctor of Philosophy in the  
School of Civil and Environmental Engineering

Georgia Institute of Technology  
August 2018

**COPYRIGHT © 2018 BY QI LIU**

# **PARTICLE-LADEN FLUIDS: FUNDAMENTALS AND ENGINEERING APPLICATIONS**

Approved by:

Dr. J. Carlos Santamarina, Advisor  
School of Civil and Environmental  
Engineering  
*Georgia Institute of Technology*

Dr. Susan E. Burns  
School of Civil and Environmental  
Engineering  
*Georgia Institute of Technology*

Dr. J. David Frost  
School of Civil and Environmental  
Engineering  
*Georgia Institute of Technology*

Dr. Guillermo Goldsztein  
School of Math  
*Georgia Institute of Technology*

Dr. Sheng Dai  
School of Civil and Environmental  
Engineering  
*Georgia Institute of Technology*

Date Approved: April 25, 2018

*To my wife and daughter.*

## ACKNOWLEDGEMENTS

I would like to express my gratitude to my advisor, Dr. J. Carlos Santamarina for his support, patience, and encouragement throughout my graduate studies. I am always impressed by his knowledge, curiosity, and dedication. It has been a privilege for me to spend past 5 years working with and learning from such a great scientist and wise man.

My thanks go to my other thesis committee members, Dr. J. David Frost, Dr. Susan E. Burns, Dr. Sheng Dai, and Dr. Guillermo H. Goldsztein, for their insightful and helpful comments and suggestions.

I would like to thank all group members of the Particulate Media Research Laboratory in Georgia Tech and the Energy Geoengineering Laboratory at KAUST. I am grateful to my colleagues Zhonghao Sun and Dr. Budi Zhao for our frequent discussions and fruitful collaborations. Also, I would like to thank Gabrielle E. Abelskamp for editing this thesis.

Last but not least, I would like to thank my wife, Lu Xu, and my parents for their unconditional love and support. Special thanks to my daughter Youyou Liu for bringing so much happiness to me. I could not have completed this work without their support.

## TABLE OF CONTENTS

ACKNOWLEDGEMENTS	iv
LIST OF TABLES	x
LIST OF FIGURES	xi
SUMMARY	xviii
CHAPTER 1. INTRODUCTION	1
1.1 Motivation	1
1.2 Thesis Organization	2
CHAPTER 2. THE MECHANICAL RESPONSE OF NANOPARTICLE-COATED INTERFACES	4
2.1 Introduction	4
2.2 Film Formation	5
2.3 Experimental Study: Materials and Procedures	7
2.3.1 Materials	7
2.3.2 Setup	8
2.4 Experimental Results	9
2.4.1 Shrinkage of a nanofluid drop in oil	9
2.4.2 Shrinkage of an oil drop in nanofluid	10
2.4.3 Expansion of a particle-coated interface	11
2.5 Analyses and Discussion	12

2.5.1	Packing and time effect	12
2.5.2	Asymmetric behaviour	15
2.5.3	Buckling patterns	18
2.6	Effects on Immiscible Displacement	19
2.7	Conclusions	21
CHAPTER 3. NANOPARTICLE TRANSPORT IN POROUS MEDIA		32
3.1	Introduction	32
3.2	Experimental Study: Materials and Procedures	33
3.2.1	Materials	34
3.2.2	Characterization Methods	34
3.2.3	Adsorption Column	35
3.3	Results and Analyses	36
3.3.1	Zeta potential of silica and carbonate grains	36
3.3.2	Adsorption behaviour analysed with DLVO theory	37
3.3.3	Nanoparticle transport and adsorption behaviour	39
3.4	Transport and Adsorption Model	42
3.5	Conclusions	44
CHAPTER 4. PARTICLE MIGRATION AND CLOGGING IN POROUS MEDIA		55
4.1	Introduction	55
4.2	Particle Retardation and Capture	56
4.2.1	Particle level forces	56
4.2.2	Particle retardation	57
4.2.3	Particle capture	59

4.3	Experimental Study: Materials and Methods	60
4.3.1	Fabrication of microfluidic chips	60
4.3.2	Materials	61
4.3.3	Test protocol	61
4.3.4	Image analysis	62
4.4	Results: Clogging at the Pore-scale	62
4.5	Results: Clogging at the Meso-scale	63
4.5.1	Permeability reduction	64
4.5.2	The effect of flow rate	64
4.5.3	The effect of radial flow	66
4.6	Dependent Clogging: Image Analyses and Simulations	67
4.6.1	Experimental results	67
4.6.2	Pore network simulation	68
4.7	Conclusions	70
	 CHAPTER 5. PARTICLE FILTRATION: MUDCAKE GROWTH	 91
5.1	Introduction	91
5.2	Model Development	92
5.2.1	Eulerian system	92
5.2.2	Lagrangian system	94
5.2.3	Dimensionless analysis	96
5.3	Clay Behavior- Constitutive Equations	96
5.3.1	Clay structure	97
5.3.2	Compressibility	98

5.3.3	Fluid flow: permeability versus void ratio	98
5.3.4	Temperature: clay rheology and fluid viscosity	99
5.3.5	Fluid chemistry: pH and ionic concentration	100
5.4	Cake Formation- Model Prediction	101
5.4.1	Filtration pressure and filtration time	101
5.4.2	Depth	102
5.4.3	Viscosity of the continuous phase	102
5.4.4	Permeability	103
5.5	Implications	103
5.5.1	Cementation: mud replacement and cake removal	103
5.5.2	Differential pressure sticking	105
5.6	Conclusions	106
CHAPTER 6. MAGNETIC WATER BASED DRILLING MUD		124
6.1	Introduction	124
6.2	Materials and Methods	125
6.2.1	Materials	125
6.2.2	Suspension preparation	126
6.2.3	Rheology measurement	126
6.2.4	Magnetic hysteresis measurement	126
6.3	Results and Analyses	127
6.3.1	Dispersion stability	127
6.3.2	Rheological properties	128
6.3.3	Magnetic properties	129



6.4	Discussion	130
6.4.1	Bentonite-surfactant-Fe <sub>3</sub> O <sub>4</sub> interactions	130
6.4.2	Magnetic properties	132
6.5	Conclusions	133
CHAPTER 7. MAGNETIC TOOL FOR WELLBORE MONITORING		141
7.1	Introduction	141
7.2	Well Completion Evaluation Tools: Overview	142
7.3	Magnetic Sensing Tools: Overview	143
7.3.1	Magnetic Sensors	144
7.3.2	Downhole Applications	145
7.4	The KAUST Magnetic Logging Tool	145
7.4.1	Sensor selection and calibration	145
7.4.2	Multi-sensor probe	146
7.4.3	Deployment and data processing	146
7.5	Casing Selection: Shield Effect	147
7.6	Applications	149
7.6.1	Fracture Detection	149
7.6.2	Cement Job Evaluation	151
7.7	Conclusions	154
CHAPTER 8. CONCLUSIONS		167
REFERENCES		171

## LIST OF TABLES

Table 3.1	Mass analyses for the adsorption of nanoparticles in carbonate. Injection fluid: pH=10.	46
Table 3.2	Adsorption parameters used in the model.	47
Table 5.1	Summary of constitutive equations in compressible cake models. Compressibility and Permeability.	108
Table 5.2	Model parameters.	110
Table 7.1	Sensitivity of different magnetic sensors. The orange and blue bands indicate the strength of the bio's magnetic field and the Earth's magnetic field.	156
Table 7.2	Relative permeability of common materials.	157

## LIST OF FIGURES

Figure 2.1	Interfacial energy change. (a) Transfer of a spherical particle from water to water-oil interface. (b) The influence of the contact angle on the interfacial energy change. Note: the radius $a=100\text{nm}$ , water oil interfacial tension $\gamma_{ow}=30\text{mN/m}$ .	23
Figure 2.2	Film formation. (a) Particle-surfactant interactions. (b) The formation of the shell-like interface.	23
Figure 2.3	Experimental setup.	24
Figure 2.4	. Droplet deformation studies. (a) Shrinkage of a nanofluid drop in oil. (b) Shrinkage of an oil drop in nanofluid; (c) Expansion of a nanofluid drop in oil.	26
Figure 2.5	The evolution of surface coverage and particle packing during the compression of a particle-coated interface.	27
Figure 2.6	Time effects. (a) Relationships between $R1/R0$ , $R2/R0$ , and $R2/R1$ and adsorption time. (b) Surface coverage as a function of adsorption time.	27
Figure 2.7	Asymmetric behavior. (a) A single particle at the fluid-fluid interface. (b) Capillary force and polar angle. (c)-(e) The deformation of a particle chain with or without particle-interface interactions. (f) The maximum force the particle chain can withstand without deformation. Case parameters: interfacial tension $\gamma=0.05\text{ N/m}$ , particle radius $R=50\text{ nm}$ , contact angle $\theta=135^\circ$ , rolling friction $f=10^{-10}\text{ N}$ .	28
Figure 2.8	. Buckling and crumpling patterns. (a) The influence of boundary conditions. (b) The influence of the initial surface coverage: the initial surface coverage increases from left to right.	29
Figure 2.9	The nanoparticle-coated interface traverses a pore throat.	30
Figure 2.10	Viscous fingering. (a) Normal fingering: water displaces mineral oil. (b) Abnormal fractal fingering: nanofluid (0.5% Silica nanoparticle, $8\times 10^{-5}\text{M}$ CTAB) displaces mineral oil.	31

Figure 3.1	Concentration determination. (a) UV-vis adsorption spectra of nanofluids with different concentrations. (b) The linear relationship between concentration and absorbance at 212nm.	48
Figure 3.2	Experimental setup.	49
Figure 3.3	The zeta potential of silica and carbonate. (a) Effect of pH on the zeta potential of silica nanoparticles. (b) Effect of NaCl concentration on the zeta potential of silica nanoparticles and carbonate. (c) Effect of CaCl <sub>2</sub> concentration on the zeta potential of silica nanoparticles and carbonate.	50
Figure 3.4	Silica particle-surface interaction energy in 1:1 electrolyte solution calculated with DLVO theory. (a) Effect of ionic concentration (constant surface potential). (b) Effect of surface potential (constant ionic concentration).	51
Figure 3.5	Breakthrough curves for adsorption column tests. Dashed lines are reference curves, solid lines are model fittings. (a) Breakthrough curves for nanoparticle injections with pH=3 and pH=0 solution in silica porous media. (b) Breakthrough curves for nanoparticle injections with pH=3 and pH=10 solution in carbonate porous media. (c) Breakthrough curves for nanoparticle injections with pH=10 solution in carbonate porous media. Nanofluids have different salt concentration and types.	52
Figure 3.6	SEM images of silica sand grains before and after nanofluid injections.	53
Figure 3.7	SEM images of carbonate sand grains after nanofluid injection and flushing: a) clean carbonate, b) outlet pH=3, c) outlet pH=10, d) outlet pH=10, c(CaCl <sub>2</sub> )=0.01M, e) inlet pH=10, c(NaCl <sub>2</sub> )=0.6M, f) outlet pH=10, c(NaCl <sub>2</sub> )=0.6M.	54
Figure 3.8	Adsorption sites available on the mineral substrate.	54
Figure 4.1	Particle Retardation. (a) The effect of local particle concentration on pore throat clogging. (b) Gravity effects. (c) Inertial effects.	72
Figure 4.2	Inertial effect. (a) The geometry of the pore constriction. (b) Average fluid velocity and particle velocity along the pore constriction. (c) Particle retention due to the inertial effect.	73
Figure 4.3	Particle capture by direct interception. (a) Sketch of direct interception. The streamlines followed by the particle define the limiting streamline. (b) The particle capture efficiency by direct	74

interception  $\eta_{DI}$  depends on *the* Reynolds number  $Re$  and the relative radius of the migrating particle  $rp=Rp/R$ .

Figure 4.4	Soft lithography protocol. Modified from Mazutis et al. 2013.	75
Figure 4.5	Microfluidic chips. (a) Design sketch. (b) Cross-section of a constriction. (c) Close up view of a chip after fabrication.	76
Figure 4.6	Experimental setup. (a) All components. (b) Schematic. (c) Close up view of a chip before and after testing.	77
Figure 4.7	Image analyses. (a) Clogged pores and detection algorithm. (b) Distribution of clogged constrictions in chip.	78
Figure 4.8	Typical pore-scale clogging patterns. (a) 10 $\mu\text{m}$ glass particles. (b) 5 $\mu\text{m}$ glass particles (no clogging occurs). (c) 10 $\mu\text{m}$ latex particles. (d) 5 $\mu\text{m}$ latex particles.	79
Figure 4.9	Two different mechanisms responsible for the clogging at pore constrictions. (a) Direct bridging: glass particle. (b) Deposition: latex particle.	80
Figure 4.10	Evolution of particle capture and clogging at constrictions. 10 $\mu\text{m}$ latex particles.	81
Figure 4.11	Influence of existing clogging on flow tortuosity and particle retardation. Note: arrows mark clogged pore throats	82
Figure 4.12	Clogging evolution. (a) Pressure and clogging numbers increase with time. (b) Permeability reduces with an increased clogging ratio.	83
Figure 4.13	The distribution of the Reynolds number in the microfluidics chip. Flow rates: 20 $\mu\text{L}/\text{min}$ , 40 $\mu\text{L}/\text{min}$ , and 60 $\mu\text{L}/\text{min}$ .	83
Figure 4.14	The effect of flow rate on the evolution of clogging. (a) 10 $\mu\text{m}$ glass particles. (b) 10 $\mu\text{m}$ latex particle.	84
Figure 4.15	The influence of radial flow on the clogging of glass particles. (a) The distribution of row clogging ratios per unit pore volume suspension at 500 pore volumes. (b) The distribution of row clog ratios at 500 pore volumes. Flow rates: 20 $\mu\text{L}/\text{min}$ , 40 $\mu\text{L}/\text{min}$ and 60 $\mu\text{L}/\text{min}$ .	85
Figure 4.16	The evolution of the distribution of row clogging ratios for latex particles. Flow rates: 60 $\mu\text{L}/\text{min}$ .	86

Figure 4.17	Schematic diagram of dependent and independent clogging.	87
Figure 4.18	Dependent and independent clogging probability for 10 $\mu\text{m}$ glass particles. Flow rates: (a) 20 $\mu\text{L}/\text{min}$ , (b) 40 $\mu\text{L}/\text{min}$ , and (c) 60 $\mu\text{L}/\text{min}$ .	88
Figure 4.19	Dependent and independent clogging probability for 10 $\mu\text{m}$ latex particles. Flow rates: (a) 40 $\mu\text{L}/\text{min}$ and (b) 60 $\mu\text{L}/\text{min}$ .	89
Figure 4.20	Permeability reduction with $P_{\text{dep}}=P_{\text{ind}}$ , $5P_{\text{ind}}$ , $10P_{\text{ind}}$ , and $100P_{\text{ind}}$ . Note: $P_{\text{dep}}$ is the probability of dependent clogging and $P_{\text{ind}}$ is the probability of independent clogging.	90
Figure 5.1	Piston model. (a) Schematic representation of the piston model. (b) An infinitesimal element in the Eulerian system. (c) An infinitesimal element in the Lagrangian system.	111
Figure 5.2	Constitutive equations of sodium bentonite. (a) Effective stress vs. void ratio. (b) Permeability vs. void ratio. (Data from: Sharma and Zongming 1991, Sherwood et al. 1991, Sherwood and Meeten 1997, Sivapullaiah, Sridharan et al. 2000)	112
Figure 5.3	Impact of environmental factors on the bentonite fabric: dispersed and aggregated clay platelets.	112
Figure 5.4	Environmental factor: ionic concentration. (a) The influence of the salt concentration on the liquid limit of sodium bentonite. Data from: Schmitz et al., 2003. (b) Odometer curves for bentonite reconstituted with and immersed in NaCl solutions at various concentrations. (Data from: Di Maio et al., 2004)	113
Figure 5.5	Viscosity and filtration loss properties at 4% bentonite as a function of the amount of exchangeable calcium. Filtration loss in API tests. (Data from: Williams et al. 1953).	114
Figure 5.6	Cake formation: the influence of filtration time. Void ratio profiles at 50s, 200s, 800s and 3,200s for a 2MPa filtration pressure. Constitutive parameters are in Table 2.	115
Figure 5.7	Cake formation: the effect of filtration pressure. Void ratio contours versus wellbore depth presented in terms of filtration pressure. Filtration time=2.8hr at all depths.	116
Figure 5.8	Cake formation: the effect of time. (a) Case: from 400m to 600m depth and rate of penetration ROP=20m/hr. (b) Increasing	117

mudcake thickness ( $e=10$ ) with increasing still-time from 0hr to 24hr.

- Figure 5.9 The influence of the liquid viscosity on the filtration behavior. (a) Void ratio profile. (b) Cumulative filtration volume. Fluid viscosities between 0.3cp and 100cp, filtration pressure=1MPa and filtration time=1hr. 118
- Figure 5.10 The influence of permeability on the filtration response. (a) Void ratio distribution. (b) Cumulative filtration volume. Reference permeability  $k_0=1\times 10^{-5}\text{mD}$ ,  $5\times 10^{-5}\text{mD}$  and  $1\times 10^{-4}\text{mD}$ , filtration pressure=1MPa and filtration time=1hr. 119
- Figure 5.11 Thixotropic behavior of bentonite suspension with void ratio  $e=19, 23, 32$  and  $49$ . Solid lines are the model prediction (Equation 12) and symbols are measured values. (Data from: El Mohtar and Yoon 2013) 120
- Figure 5.12 Yield Strength. Effective stress dependency in the cake, and thixotropic time-dependency in the mud. 121
- Figure 5.13 Residual cake thickness after cement invasion. Black lines: shear stress imposed by the invading cement. Blue line: cake-mud shear strength (refer to Figure 5.12). 122
- Figure 5.14 “Stuck pipe” by differential pressure sticking. (a) Fluid pressure against the casing for a 1MPa filtration pressure. (b) The effect of the still-time  $t$  on the total force against the pipe  $T$ . 123
- Figure 6.1 Molecular structures of SDS, CTAB and Tween 20. 134
- Figure 6.2 Ionic concentration (ppm). Major element in the bentonite sample. 134
- Figure 6.3 Terminal velocity as a function of particle radius and fluid viscosity. Note: the analytical solution is valid for individual spherical particles. 135
- Figure 6.4 The influence of surfactant types on the stability of bentonite- $\text{Fe}_3\text{O}_4$  suspensions. Note: 5%  $\text{Fe}_3\text{O}_4$ , 2% bentonite and 8mM surfactant. 136
- Figure 6.5 The influence of the SDS concentration on the stability of benotnite- $\text{Fe}_3\text{O}_4$  suspensions. 136

Figure 6.6	The influence of the SDS concentration on the stability of bentonite-Fe <sub>3</sub> O <sub>4</sub> suspensions. (a) Based on 2% bentonite mud. (b) Based on 3% bentonite mud.	137
Figure 6.7	The influence of temperature on the viscosity of bentonite suspensions (3% bentonite+5% Fe <sub>3</sub> O <sub>4</sub> particles+ 8mM SDS).	138
Figure 6.8	Magnetic properties of magnetic mud as a function of Fe <sub>3</sub> O <sub>4</sub> concentration. (a) Hysteresis curves. (b) Saturation magnetization and residual magnetization.	139
Figure 6.9	Magnetic hysteresis curves of 10% Fe <sub>3</sub> O <sub>4</sub> samples at T=250k and T=300k.	140
Figure 7.1	Potential events result from poor cement jobs.	158
Figure 7.2	Sensitivity of fluxgate and magnetic tunnel junction. (a) Along the main axis. (b) Transverse to the main axis. (c) Directivity.	158
Figure 7.3	The multi-sensor probe.	159
Figure 7.4	Shield effect. (a) 3-D modeling of the shield effect of a casing. (b) Numerical simulation: the influence of casing material on the projection of the magnetic field generated by a solenoid. The iron casing completely shields the internal magnetic field. The stainless steel casing has a negligible influence. (c) Lab experiments.	160
Figure 7.5	Magnetization of a fracture filled with a ferromagnetic tracer. From left to right: a permanent magnet travels upward through the fracture.	161
Figure 7.6	Geometric definition of a fracture.	162
Figure 7.7	Magnetic field strength along the center axis of fractures access a well of varying radius R <sub>2</sub> . Solid lines are analytical solutions and dots are experimental results.	162
Figure 7.9	Inverse solution. (a) 3D-2D simplification. (b) Residuals determined with L <sub>2</sub> error norm.	163
Figure 7.8	Magnetic field strength of a dipole. (a) Coordinate system. (b) Response map.	164



Figure 7.10 Magnetic logging of an asymmetric accumulation. (a) Model and magnetic material distribution. (b) Raw data. (c) Inversion of raw data to determine the spatial distribution of the magnetic material. 165

Figure 7.11 Magnetic logging of a thin fracture. (a) Model and magnetic material distribution. (b) Raw data. (c) Inversion of raw measurement data to determine the spatial distribution of the magnetic material. 166

## SUMMARY

Particle-laden fluids pervade oil/gas drilling and production, such as drilling fluids, fracturing fluids, and fines migration in the reservoir formation. Particle types include nanoparticles, clay minerals, and fines, with particle sizes spanning from nanometer to millimeters. These particles may interact among themselves, with other particles, the porous medium, and the liquid-fluid interface. Research tools used in this study include adsorption columns, microfluidics, analytical solutions, and numerical simulations.

Surface modified nanoparticles show a strong affinity for the water-oil interface. Particle accumulation at the interface alters the capillary behavior and immiscible fluid displacement. Experimental results identify the inherent asymmetric behavior of the particle-coated interface, and the modified interface can resist a substantial pressure difference. The adsorption of nanoparticles onto mineral surfaces is a major constraint for applications of nanoparticles which require a long transport distance, e.g. groundwater remediation and enhanced oil recovery. Adsorption column tests suggest that pH, ion type/concentration, and the mineral composition of the porous medium influence the adsorption and transport of nanoparticles. Migrating particles may plug pore constrictions and reduce permeability when the constriction-to-particle size ratio is small. Transparent microfluidic chips allow the visual observation of pore clogging and its development; image analyses demonstrate that pore constrictions located near clogged pores have a higher probability of clogging compared to pores at any other random location. A filter cake eventually builds up on the surface of a porous medium when extensive clogging develops as a slurry presses against the medium. A comprehensive new mudcake growth

model evaluates the influence of time, pressure and environmental factors on the filtration behavior of drilling muds. Subsequent analyses explore critical drilling and completion issues that include mud shearing and differential pressure sticking.

Finally, the rapid development of high-resolution magnetic sensors provides an opportunity to develop innovative magnetic logging tools for the quality control of drilling and completion operations. A new magnetic mud is engineered to serve as a tracer material. A multi-sensor probe conducts 3-D measurements of the magnetic field strength along a cased borehole. An efficient inverse algorithm solves the distribution of magnetic materials around the well with high spatial resolution.

## CHAPTER 1. INTRODUCTION

### 1.1 Motivation

The interaction of particles with the porous medium is a scientifically challenging problem of great engineering importance. Migrating particles experience physical and chemical interactions among themselves, with other particles, the porous medium, and liquid-fluid interfaces.

Particle-laden fluids pervade oil/gas drilling and production, such as drilling fluids, fracturing fluids, and fine migration in the reservoir formation. The filter cake provides a physical barrier to seal permeable formations and improve wellbore integrity in drilling operations (Cook *et al.*, 2011).

Fines migrate during oil/gas production and may clog formations, reduce permeability, and cause productivity decline (Krueger, 1988; Zeinijahromi *et al.*, 2012). The unique properties of engineered nanoparticles have applications in both enhanced oil recovery (Zhang *et al.*, 2014; Nazari *et al.*, 2015) and environment remediation (Khin *et al.*, 2012). However, the adsorption of nanoparticles is a major limitation for applications of nanoparticles which require a long transport distance.

Surface modified particles can further interact with the oil-water interface under multiphase flow conditions. The assembly of a monolayer of particles at liquid-fluid interfaces can stabilize emulsions (Pickering emulsions, see Binks, 2002) and alter immiscible displacement (Luo *et al.*, 2016).

The phenomena listed above are complex and require detailed experimental studies and careful analyses. These are the central focus of this thesis.

## **1.2 Thesis Organization**

The research presented in this thesis addresses the interactions of particle-laden fluids with the porous medium and their implications for energy geoengineering. A brief summary of the individual chapters follows.

Chapter 2 investigates the interactions of nanoparticles and the oil-water interface with the focus on the formation mechanism and the mechanical properties of the nanoparticle-coated interface. Experimental results identify an asymmetric behavior of the particle-coated interface and show that it can resist a substantial pressure difference. The influence of the particle-coated interface on immiscible displacement is also discussed.

Chapter 3 explores the transport and adsorption behavior of nanoparticles in a porous medium made of natural minerals. Adsorption column tests reveal the effect of pH, ion concentration, and ion type. Grain-scale and macroscale analyses provide physical insight into ongoing adsorption and transport processes. Chapter 2 and Chapter 3 are collaborative studies with Zhonghao Sun. In particular, Chapter 2 is a joint publication and it is reproduced here as well as in Sun's Dissertation.

Chapter 4 concentrates on micron-size particle transport and clogging. Pore-scale and meso-scale studies performed with microfluidics chips identify the fundamental clogging mechanisms for glass particles and latex particles. Image analyses reveal the interactions between successive pore-scale clogging events. The reported investigation was performed in collaboration with Dr. Budi Zhao.

Chapter 5 focuses on surface filtration. A comprehensive mudcake growth model is advanced based on robust constitutive equations. The model evaluates the influences of time, pressure and environmental factors such as temperature and salinity on the filtration behavior of drilling muds. Subsequent analyses explore critical drilling and completion issues that include mud shearing and differential pressure sticking.

Chapter 6 documents an economical and stable ferromagnetic drilling fluid engineered for wellbore monitoring. Micron-size iron oxide ( $\text{Fe}_3\text{O}_4$ ) particles are suspended in bentonite mud; surfactants help stabilize the  $\text{Fe}_3\text{O}_4$ -bentonite suspension. A systematic study of the suspension stability, rheological properties, and magnetic hysteresis of the magnetic sensitive guides the engineering of optimal magnetic sensitive drilling fluid. This chapter was developed in collaboration with Dr. Anant Ghumare.

Chapter 7 develops a magnetic logging system for wellbore monitoring. A multi-sensor tool and inversion algorithms were developed for fracture detection and cement job quality control.

Finally, Chapter 8 summarizes salient conclusions from this study.

## CHAPTER 2. THE MECHANICAL RESPONSE OF NANOPARTICLE- COATED INTERFACES

*Note: the study documented in this Chapter is a collaborative effort with Zhonghao Sun. The joint publication is reproduced herein as well as in Sun's Dissertation.*

### 2.1 Introduction

The assembly of a monolayer of particles at liquid/liquid or liquid/gas interfaces has attracted great attention in recent years due to its distinctive properties and number of potential applications. These assembled layers have been described as particle rafts (Cicuta and Vella, 2009), granular rafts (Jambon-Puillet, 2016), and particle-laden interfaces (Razavi et al., 2015). They form particle-coated droplets (Deshmukh et al., 2015), particle-covered bubbles (Abkarian et al., 2007), armored droplets (Sicard and Striolo, 2017), and liquid marbles (Aussillous and Quere, 2001). The particle-coated interface stabilizes emulsions and foams (Pickering emulsions and foams; see Binks 2002 and Chevalier and Bolzinger 2013), and could enhance oil recovery (Luo et al., 2016) and drag delivery (Frelichowska et al., 2009).

The deformation of the particle-coated interface is intriguing. The particle-coated interface undergoes a transition from liquid-like to shell-like behavior as the particle coverage increases when the size of the interface decreases (Datta et al., 2010). Further compression leads to a collapse of the interface due to buckling instabilities or particle expulsion (Razavi et al., 2015). Previous experiments studied the deformation of the

particle-coated interface primarily with a Langmuir trough setup and analyzed the surface pressure  $\Pi=\gamma_0-\gamma$  curve (Santini et al., 2011; Deak et al., 2007; Horozov et al., 2006). The particle-coated interface has been modeled as an elastic sheet (Vella et al., 2004; Pocivavsek et al., 2008; Cicutta et al., 2003). A few studies also investigated the deformation of bubbles or droplets coated with particles (Asekomhe et al., 2005; Monteux et al., 2007; Datta et al., 2010).

However, some suggest that measurements with the Langmuir trough and Wilhelmy plate are distorted, and that the surface pressure is not uniform throughout the trough due to the granular character of the particle-coated interface (Cicutta and Vella, 2009; Pocivavsek et al., 2008; Aumaitre et al., 2011). Moreover, experimental conditions in the trough differ from most applications where the interface is curved (small droplets, bubbles, and pore constrictions). Furthermore, elastic models ignore the granular nature of the particle shell and the complexity of particle-interface interactions (Leaby et al., 2010; Dasgupta et al., 2017; Bresme and Oettel, 2007; Jambon-Puillet et al., 2017).

This study uses a different approach to investigate the mechanical properties of silica nanoparticle-coated interfaces. We simultaneously measure fluid pressure responses and morphology changes of a water or oil droplet covered with nanoparticles during droplet shrinkage and expansion. This chapter starts with a review of film formation followed by the experimental study.

## **2.2 Film Formation**



The hydrophobicity of particles determines their affinity to the water-oil interface. Let's consider the interfacial energy change caused by the transfer of a particle from the water phase to the oil-water interface (Figure 2.1(a)). The total interfacial energy  $E_A$  of a solid particle of radius  $a$  and contact angle  $\theta$  is:

$$E_A = 4\pi a^2 \gamma_{ws} + \gamma_{ow} \pi a^2 \sin^2 \theta \quad (2.1)$$

The total interfacial energy  $E_B$  of a solid particle at the interface with the contact angle  $\theta$  is:

$$E_B = 2\pi a^2 \gamma_{os} (1 - \cos \theta) + 2\pi a^2 \gamma_{ws} (1 + \cos \theta) \quad (2.2)$$

Young's equation relates  $\gamma_{ow}$ ,  $\gamma_{os}$ , and  $\gamma_{ws}$  as  $\gamma_{ow} \cos \theta = \gamma_{os} - \gamma_{ws}$ . Then the free energy change  $\Delta E = E_B - E_A$ . Finally, we are able to express  $\Delta E_p$  as follows:

$$\Delta E = -\pi a^2 \gamma_{ow} (1 - \cos \theta)^2 \quad (2.3)$$

Figure 2.1(b) shows the influences of contact angles on the interfacial energy change. Completely hydrophobic ( $\theta=180^\circ$ ) or hydrophilic ( $\theta=0^\circ$ ) particles are immersed in oil or water. Only particles are partially hydrophobic attach to the interface.

Hydrophilic silica nanoparticles do not show any significant adsorption to the water/oil interface. Surfactants modifies the wettability of nanoparticles due to the adsorption of surfactant molecules onto the particle surface, a process which is surfactant concentration-dependent. Figure 2.2(a) shows the interaction mechanisms between negatively charged silica nanoparticles and cationic surfactant hexadecyl-trimethyl-

ammonium bromide (CTAB). CTAB interacts with silica nanoparticles through electrostatic forces until the CTAB saturates the nanoparticle surface (hemimicelle). Hydrophobic interactions between carbon chains lead to the adsorption of additional CTAB molecules and the formation of ad-micelles at high CTAB concentration. As a result of this process, the wettability of the particle changes from hydrophilic to hydrophobic with the increase in the CTAB concentration and turns to hydrophilic again at very high CTAB concentrations (A. Maestro et al., 2012).

## **2.3 Experimental Study: Materials and Procedures**

We carefully expand and shrink a nanoparticle-coated water/oil droplet to understand the mechanical response of the particle-coated interface during deformation. Details of the experimental setup and materials follow.

### *2.3.1 Materials*

Experiments use silica nanoparticles (fumed silica from Sigma-Aldrich) with a hydraulic diameter of 100 nm measured with the dynamic light scattering method (Zetasizer Nano ZS, Malvern Instruments). The silica nanoparticles are tuned with CTAB to promote adsorption onto the interface. The CTAB has a purity >99% (Sigma-Aldrich).

Nanofluids are prepared by mixing nanoparticles with CTAB solution and then sonicated for 40mins. The solution includes NaCl and NaOH to promote the adsorption of surfactants and increase the nanofluid stability. All solutions have a salt concentration

$C_{\text{NaCl}}=1\text{mM}$  and  $\text{pH}=10$  (Ravera et al., 2006). Nanofluids used in this study have 0.5% nanoparticles by weight and different concentrations of CTAB ( $10^{-6}$ - $2\times 10^{-3}$  M).

Mineral oil (Mineral Oil Light, from Sigma-Aldrich) has a density of  $877\text{ kg/m}^3$  and interfacial tension of  $34.2\text{ mN/m}$  measured by the pendent drop method (Attension Theta optical tensiometer, Biollin Scientific).

Borosilicate glass capillaries (from Drummond Scientific Company) has ID= $0.56\text{ mm}$  and OD= $0.79\text{ mm}$ . We use FDTS-coated capillaries for nanofluid in oil experiments and normal capillaries for oil in nanofluid experiments to ensure a stable and smooth droplet expansion and shrinkage.

### 2.3.2 Setup

Figure 2.3 shows the experimental setup which consists of a syringe pump, pressure transducer, and a glass capillary immersed in a reservoir. The experiment starts by filling the reservoir with either mineral oil or the nanofluid. A syringe pump delivers other fluids to the capillary tip. A droplet with the desired volume is created at a constant flow rate. The droplet is kept at rest for a certain time  $t_{\text{ad}}$  to allow nanoparticles to adsorb to the interface. Then we reduce the volume of the droplet by the withdrawal of the fluid with a flow rate  $q=0.2\text{ml/hr}$ . This slow rate ensures that the nanofilm is in a quasi-static condition throughout the withdrawal operation. After the entire droplet is withdrawn into the capillary, we may inject more fluids to expand the nanofilm. A microscope (ZEISS, Stemi 2000-CS) records the deformation of the droplet during expansion or shrinkage. A pressure transducer (OMEGA, PX40) measures the fluid pressure. The droplet may undergo several expansion and shrinkage cycles.

## 2.4 Experimental Results

We conduct film formation experiments under CTAB concentrations which range from  $10^{-6}\text{M}$  to  $2 \times 10^{-3}\text{M}$ . The interface behaves as a liquid-liquid interface when the concentration of CTAB is low (less than  $10^{-5}\text{ M}$ ). The shell-like interfaces exist when the concentration of CTAB is between  $10^{-5}$  and  $2 \times 10^{-4}\text{ M}$  (Figure 2.2(b)). All other experiments use a CTAB concentration of  $8 \times 10^{-5}\text{ M}$ , as particles show strongest adsorption at this level. The study encompasses more than thirty droplet shrinkage and expansion tests, with both nanofluid droplet in oil and oil droplet in nanofluid settings. The adsorption time  $t_{ad}$  ranges from 5 min to 120 min. The test results are highly repeatable for same experimental conditions. Although the droplet does not deform identically in each test, the response shows similar features which relate to the mechanical properties of the particle-coated interface. Sections 2.4.1 to 2.4.3 present typical examples.

### 2.4.1 Shrinkage of a nanofluid drop in oil

Shrinkage of a nanofluid drop in oil have been tested with different adsorption time  $t_{ad} = 5, 10, 30$  and  $120$  mins. Figure 2.4(a) presents the fluid pressure response and drop morphologies for  $t_{ad} = 10$  mins. Based on the evolution of pressure and drop morphology, we identify four stages that characterize the interface deformation.

*Stage 1* (point 1-2): the drop retains the spherical shape and the pressure remains almost constant. This behavior is the same as the shrinkage of a water drop in oil which indicates

the water-oil interfacial tension still governs the interface. The surface coverage of particles increases due to the reduction of the total interface area.

*Stage 2* (point 2-3): the drop remains spherical; however, the pressure starts to decrease. This observation suggests that the surface coverage of particles reaches a significant value and require a non-trivial pressure to overcome the particle-particle interactions (Luu et al., 2013). Therefore, the overall interfacial tension decreases, and lowers the pressure.

*Stage 3* (point 3-5): the interface begins to wrinkle when the pressure falls close to 0 Pa. The pressure remains constant as the interface buckles. The low pressure indicates the vanishing of the overall interfacial tension and suggests a compression stress in the particle ensemble. The surface coverage of particles reaches the maximum level. A shell-like membrane is clearly visible. Both crumpling and mirror buckling are observed in different experiments.

*Stage 4* (post point 5): a further decrease in pressure is required to withdraw the film into the capillary.

#### *2.4.2 Shrinkage of an oil drop in nanofluid*

By contrast to the experiments above, we reduce the volume of a mineral oil drop in a nanofluid reservoir. Figure 2.4(b) shows the experimental results after  $t_{ad} = 10$  mins. The mechanical behavior is strikingly different from the nanofluid drop-in-oil case.

*Stage 1* (before point 1): the drop keeps the spherical shape, and the pressure remains constant. This is similar to the nanofluid drop-in-oil case.

*Stage 2* (point 1-4): at the beginning, the pressure decreases while the top of the oil drop (the side farthest from the capillary) retains a relatively constant curvature. As the pressure drops to 0 Pa (point 2 in Figure 2.4(b)), several wrinkles appear at the bottom of the oil drop (the side close to the capillary). Eventually, the drop deforms from a sphere to a semi-sphere (point 3). The pressure decreases below zero, and indicates an overall negative interfacial tension and substantial compression stress inside the particle ensemble. A further decrease in pressure causes localized wrinkles of the particle-coated interface which initiates from the bottom of the sphere and develops to the top (point 4). The particle ensemble sustains a pressure difference larger than 200 Pa (the pressure difference between points 1 and 4).

*Stage 3* (point 4-5): finally, the drop becomes unstable and the film suddenly breaks off. A fresh water-oil interface forms and the pressure increases (point 5). A comparison of drop shapes between points 5 and 4 also shows a relaxation of the localized wrinkles after the failure. The broken film remains outside of the capillary thereafter.

### *2.4.3 Expansion of a particle-coated interface*

We perform expansion tests by increasing the volume of the drop after drop withdrawal tests. Figure 2.4(c) displays the result for a nanofluid drop in the oil reservoir. The interface is initially inside the capillary tube. At first, the pressure is slightly above zero (point 1). The folded film expands and forms a relatively smooth interface as the volume of the drop increases (point 1 to 2). Meanwhile, the pressure also increases. However, the pressure does not reach the maximum level when the curvature of the interface reaches the largest point. This deviates from the prediction of the Young-Laplace equation, therefore the

interface is still shell-like. Suddenly the film folded inside turns out, which creates a hump at the interface (point 3). The hump gradually becomes flat and the interface becomes spherical (points 3-5). This process causes the particle-coated interface to rupture. Pieces of particle aggregations are clearly seen floating on the interface. The pressure reaches the maximum at point 5 and then starts to decrease, which suggests that the interface becomes more fluid-like.

## 2.5 Analyses and Discussion

Particle-coated interfaces shift from fluid-like to shell-like during shrinkage. Although this mechanical response has been studied with the Langmuir trough method and modeled as an elastic film, the effect of the granular character and the interface curvature remains unclear. Our results showed distinct stages of drop deformation. We demonstrated a marked difference in the mechanical response between the nanofluid drop-in oil and oil drop-in-nanofluid cases. In this section, we analyze results and consider the granular character and particle-interface interactions.

### 2.5.1 *Packing and time effect*

The mechanical response of the particle-coated interface is determined by the particle packing—the arrangement pattern of particles on the interface. The particle packing becomes denser because the surface area of the particle-coated interface decreases and the surface coverage of particles increases. This process resembles the consolidation of granular materials in 2D, where particles are packed and undergo an in-plane

rearrangement. It has been observed in previous experiments (Monteux et al., 2007). The consolidation results in increased inter-particle stresses. The packing gradually reaches the densest state, and further shrinkage results in the collapse of the interface (Bordacs et al., 2006; Deshmukh et al., 2015).

Let's define the state of a particle-coated interface as  $(R, c)$ , where  $R$  is the drop radius and  $c = A_{\text{particle}}/A_{\text{interface}}$  is the surface coverage of particles. Three key points mark the transition of the behavior of the particle-coated interface, which are identified from the unique pressure signature and morphology evolution. Particles are randomly distributed on the interface (point 1 in Figure 2.4(a)) at the initial state  $(R_0, c_0)$ . A clear decrease in pressure (point 2 in Figure 2.4(a)) marks a loose packing state  $(R_1, c_1)$ , which indicates particles are subject to compression. Finally, the interface reaches a dense packing state  $(R_2, c_2)$ , which is the densest packing the system can achieve and indicates the onset of buckling (point 3 in Figure 2.4(a)). Figure 2.5 illustrates the entire process.

The surface coverage can be inferred from the relationship between the radius and surface coverage, which is:

$$\frac{R_a}{R_b} = \sqrt{\frac{c_b}{c_a}} \quad (2.4)$$

So the expression of the initial surface coverage  $c_0$  is:

$$c_0 = c \frac{R^2}{R_0^2} \quad (2.5)$$



We assume a square packing  $c_1 = 78.5\%$  for a loose packing state and a triangular packing  $c_2 = 90.7\%$  for a dense packing state. It should be noted that inter-particle interactions and collapse can occur at a surface coverage smaller than the ideal values assumed here (Berhanu and Kudrolli, 2010).

We measure the  $R_0$ ,  $R_I$ , and  $R_2$  with adsorption time  $t_{ad}=5, 10, 30$ , and  $120$  mins to understand the kinetics of particle adsorption. Figure 2.6(a) shows the evolution of  $R_2/R_0$ ,  $R_I/R_0$ , and  $R_2/R_I$  with adsorption time. The  $R_2/R_I$  is around  $0.9$  and is independent of the adsorption time and is consistent with the model prediction:

$$\frac{R_2}{R_I} = \sqrt{\frac{c_1}{c_2}} = 0.93 \quad (2.6)$$

Both  $R_I/R_0$  and  $R_2/R_0$  increase with the adsorption time, which indicates an increase of the initial surface coverage with adsorption time. Figure 2.6(b) plots the initial surface coverage calculated from  $R_2/R_0$  and the surface coverage  $c_2$  based on Eq. (2.5).

The diffusion with a Stokes-Einstein diffusion coefficient cannot describe the adsorption process. The diffusion-controlled adsorption at the early stage changes to an interaction-controlled assembly as the surface coverage of nanoparticle increases (Ferdous et al., 2011). The presence of an energy barrier to adsorption gives an effective diffusion coefficient orders of magnitude smaller than the Stokes-Einstein diffusion coefficient (Kutuzov et al., 2007; Ward and Tordai, 1946). The results agree with previous studies using the pendant drop method (Maestro et al., 2014; Du et al., 2010; Kutuzov et al., 2007; Ferdous et al., 2011), interfacial rheology (Yazhgur et al., 2013) and TEM image (Boker et al., 2007).

### 2.5.2 *Asymmetric behaviour*

Discrete particles can form stable arch structures and withstand a substantial load. The ratio of the arch length to the particle size rarely exceeds 8 for spherical particles (Valdes and Santamarina, 2008; Garcimartin et al., 2010). The stability of the granular arch depends on the particle shape and inter-particle friction (Lozano et al., 2012). When a particle chain is under normal compression conditions, an out-of-plane deformation of particles can cause a rolling or sliding failure of the chain as shown in Figure 2.7(c).

However, the ratio of the diameter of the capillary tube to the nanoparticle size exceeds 5000 in our experiments. Therefore, other mechanisms must contribute to the stability of the particle chain. Large pressure differences and the effect of the interfacial tension indicate that the particle shells are able to withstand a large normal force. In addition, the particle-coated interface shows an asymmetric behavior where the pressure difference is larger in the oil drop-in-nanofluid case than that in the nanofluid drop-in-oil case. We consider the inter-particle contact, wettability and the capillary interaction between particles and the interface in the analyses follows.

A single particle at the fluid-fluid interface experiences a capillary force normal to the interface when it is out of the equilibrium position. Consider a spherical particle with radius  $R$  at the water-oil interface and the polar angle is  $\phi$  (Figure 2.7(a)). To move the particle to a specific polar angle, the force needed to balance the vertical component of the capillary force is (Rapacchietta and Neumann, 1977):

$$F = 2\pi RT \sin(\theta - \phi) \sin(\phi) \quad (2.7)$$

where  $\gamma$  is the water-oil interfacial tension, and  $\theta$  is the contact angle. Figure 2.7(b) shows the force required to move the particle to a specific polar angle. The force first increases with the polar angle, then drops after it reaches a maximum value.

This capillary force caused by the out-of-plane deformation not only maintains the equilibrium of a single particle, but also stabilizes particle chains. Consider a chain of particles under normal compression. Let's assume that the water-oil interface is flat between particles given the fact that the radius of interface curvature (in the order of 1 mm) is much larger when compared to the size of the particle (100 nm). The relative position of a particle at the interface depends on the contact angle  $\theta$ . This configuration of the liquid interface with particles has been seen in optical microscopy images (Bordacs et al., 2006), freeze-fracture SEM images (Subramaniam et al., 2006) and cyro-SEM images (Deshmukh et al., 2015). We assume an out-of-plane perturbation of particles chain defects with an angle  $\alpha$  (Figure 2.7(d) and 2.7(e)). The movement of the particle into one fluid out of its equilibrium position causes a counter-force induced by capillarity.

The capillary force in the presence of the water-oil interface stabilizes the chain of particles. The stabilization mechanism is curvature-dependent. The rolling friction between particles, which may also help to stabilize the chain, depends on particle size and is in the order of  $10^{-10}$  N for 100 nm particles (Heim and Blum, 1999; Dominik and Tielens, 1995). We can compute the normal force in the equilibrium condition based on the force balance (Figure 2.7(d) and 2.7(e)):

$$F_N = \frac{F}{2 \sin \frac{\alpha}{2}} + \frac{f_{rolling}}{\sin \alpha} \quad (2.8)$$

The computed maximum normal force with an out-of-plane angle  $\alpha$  is shown in Figure 2.7(f). The effect of rolling friction vanishes as the angle  $\alpha$  increases. If the particle chain deforms towards the oil, the normal force required to further bend the chain decreases as  $\alpha$  increases. In other words, a continuous failure will happen once the normal force reaches the maximum force in the initial equilibrium condition. However, if it deforms towards the water, the force required to bend the chain increases with  $\alpha$  until a maximum value is reached. Therefore, the particle chain is a self-stabilizing system and can withstand more loading.

The computed normal force is in line with our experimental measurements. First, the asymmetric behavior matches the model prediction that the oil drop in the nanofluid case can withstand a higher pressure difference. In addition, the inter-particle contact force  $F_N$  can be evaluated from the experimentally measured pressure difference  $\Delta p$ :

$$\Delta p \cdot \pi r^2 + 2\pi r \cdot T = N \cdot F_N \quad (2.9)$$

where  $N$  is the number of particles in one circumference, and  $N=\pi r/R$ . So we have:

$$F_N = (\Delta p \cdot r + 2T) \cdot R \quad (2.10)$$

$F_N=1.2 \times 10^{-8}$  N when the pressure difference is 100 Pa. This value coincides with our analytical model, though our model is 1D and the experimental condition is 2D.

Although our model did not consider other possible particle-interface interaction mechanisms (e.g., adhesion forces, pinning of interfaces and contact angle hysteresis, Bresme and Oettel, 2007; Guo et al., 2004), our analyses highlight that particle-interface interactions affect the global mechanical behavior and causes the asymmetric behavior. This finding is consistent with other studies. Datta et al. (2010) suggested that the buckling and crumpling of nanoparticle-coated droplets are supported by both localized stresses in particle rafts and capillary forces. Studies of capillary wave propagation along the particle-coated interface suggest the particle size, surface tension and contact angle control the bending stiffness of the interface (Planchette et al., 2011). In a recent molecular dynamics simulation (Sicard and Striolo, 2017), the role of the fluid-fluid interface to the buckling of particle-stabilized droplets is clearly shown. In addition, the formation of particle-stabilized emulsions from oil in water to water in oil depends on the wettability of the particle (Binks and Murakami, 2006; Kralchevsky et al., 2005), which may relate to the asymmetric behavior described here. Note that a similar asymmetric behavior has been observed in membrane bending by protein-protein crowding (Stachowiak et al. 2012, J. Derganc et al. 2013).

### 2.5.3 *Buckling patterns*

The buckling patterns of thin elastic films strongly depend on the boundary conditions (Niezgodzinski and Swiniarski, 2010), initial size and surface coverage, deformation rates (Vliegthart and Gompper, 2011), and the Föppl–von Kármán (FvK) number which describes the ratio of stretching energy to bending energy.

Two distinct patterns have been observed among all experiments: buckling and crumpling. Here we refer to buckling as a mirror-like deformation with countable depressions and crumpling as deformations with numerous wrinkles. A hydrophilic glass capillary results in buckling and a hydrophilic FDTS coated glass capillary always leads to crumpling patterns (Figure 2.8(a)). The wettability of capillary tubes modifies the boundary conditions with changes to the interaction between the particle-coated film and the boundary. The hydrophobic interaction (Meyer, Rosenberg and Israelachvili, 2006) between the FDTS and the CTAB-modified silica particles may generate a non-slip boundary condition. The slip boundary condition exists in the case of glass capillary.

Furthermore, we are able to manipulate the number of depressions during buckling with the control of the initial surface coverage of particles. Figure 2.8(b) presents buckling patterns with a different number of depressions ( $N > 4$ ,  $N = 3$ , and  $N = 2$ ). From left to right, the initial surface coverage of particles increases. All buckling patterns are symmetric. A large initial surface coverage results in a small number of depressions. Further studies are required to fully understand the relationship between the mechanical properties of the nanoparticle-coated interface and buckling patterns.

## **2.6 Effects on Immiscible Displacement**

Nanofluids and nanoparticle-stabilized emulsions have been applied in laboratory studies of enhanced oil recovery (Zhang et al., 2010; Luo et al., 2016). However, the underlying mechanisms remain unclear. There are wettability alterations and decreases in the interfacial tension (Al-Anssari et al., 2016; Moghaddam et al., 2016), but few studies consider the transport of particle-coated interfaces or droplets in porous media (Gai et al.,

2017; Mei et al., 2016). Note that in oil systems, asphaltenes, biofilms, and fine particles can also adsorb to the oil-water interface and form a composite with similar properties of particle-coated interfaces (Gao et al., 2009; Kim et al., 2013; Ruhs et al., 2013; Kang et al., 2008).

Pores in sediments have converging-diverging cross-sections, interfaces expand or shrink during traveling through porous media. Localized instabilities such as Haines jumps and snap-offs occur during fluid displacement due to the interaction of interfaces with the non-uniform pore geometry (Jang et al., 2016). These microscale instabilities affect macroscale displacement patterns (Holtzman and Segre, 2015).

The particle-coated interface can alter both the multiphase flow through a converging-diverging pore and the fingering pattern in a fracture. When a particle-coated interface passes through a pore throat, the shrinkage and expansion of the interface is similar to the drop experiments previously discussed. Figure 2.9 presents the status of the interface and the pressure changes during the transport process. In stage 1, the capillary pressure increases due to a reduction in the radius. In stage 2, increased surface particle coverage leads to the formation of a solid-like film. The formation of the film lowers the interfacial tension. After the film passes the pore throat, the shell-like film returns to the status of a normal spherical oil-water interface (stage 3). The asymmetrical behavior is also observed which suggests the interface behavior when passing through the pore throat depends on the curvature of the interface and also the wettability of the particle.

In addition, Saffman-Taylor fingering occurs in Hele-Shaw cell studies when a low viscosity fluid displaces a high viscosity fluid, and thus results in a large portion of residual

liquid (Saffman and Taylor, 1958). These instabilities hinder resource recovery. Fractal-like fingering patterns are observed during nanofluids displacing oil in a Hele-Shaw cell with Plexiglas plates, which is different to the Saffman-Taylor instabilities in water displacing oil (Figure 2.10). A better understanding of the effects of particle-coated interfaces on multiphase flow in porous media will lead to the development of potential applications for oil/gas recovery, CO<sub>2</sub> geological storage, and ground contamination remediation.

## 2.7 Conclusions

This chapter documented the study of silica nanoparticle-coated interfaces. The experimental approach analyzed the pressure signature and morphology of an oil or water drop covered with nanoparticles during shrinkage and expansion. Salient results follow.

The interface undergoes a transition from fluid-like to solid-like as the volume of the droplet reduces. Analyses suggest that nanoparticles evolve from loose packing to dense packing with increases in surface coverage. Further compression of the closely packed particles results in the buckling of the particle-coated interface.

The adsorption kinetics of nanoparticles at the interface is studied by comparing the mechanical response of droplets with different adsorption times. Our results are consistent with previous studies and confirm a diffusive, time-dependent rate of coverage.

The particle-coated interface exhibits an asymmetric, curvature-dependent mechanical behavior: the response of a nanofluid drop in oil and an oil drop in nanofluid



show salient differences during shrinkage. For an oil drop in nanofluid, the particle-coated interface withstands a significant pressure difference before collapse. However, the nanofluid drop in oil buckles at a negligible pressure difference. Analyses of the stability of particle chains demonstrate that the particle-interface interaction provides an additional supporting force to prevent the particle chain failure and is responsible for this asymmetric behavior.

Our work emphasizes the granular character of the particle-coated interface, the effects of particle-particle/interface interactions on the global behavior, and its inherent asymmetric behavior. Findings in this study have wide relevance to practices related to Pickering emulsions and studies on particle-coated interface transport in porous media.

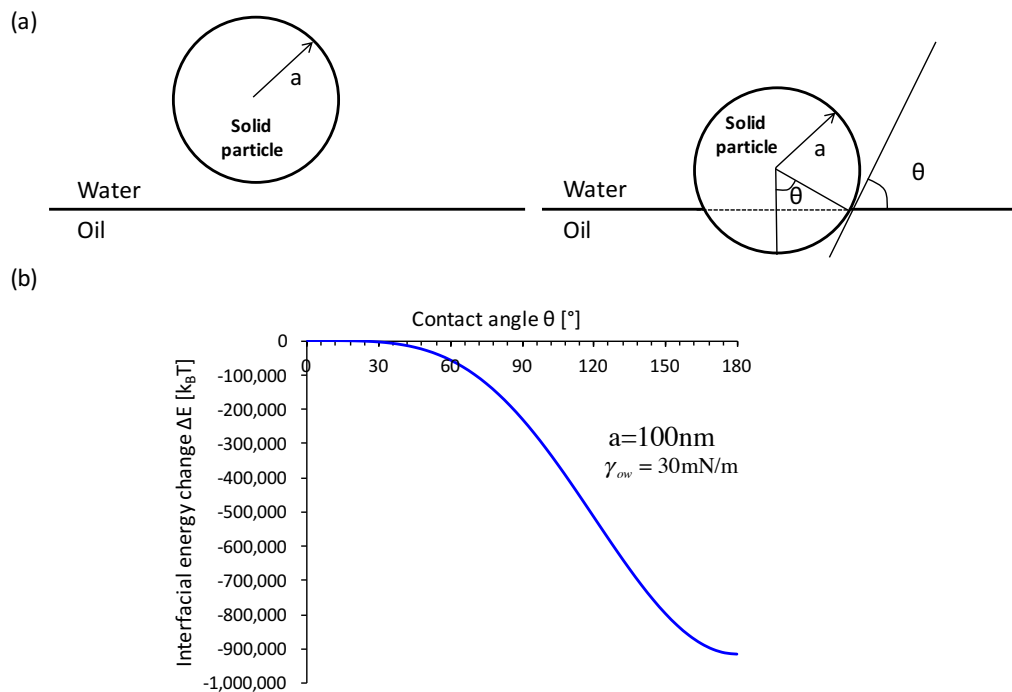


Figure 2.1. Interfacial energy change. (a) Transfer of a spherical particle from water to water-oil interface. (b) The influence of the contact angle on the interfacial energy change. Note: the radius  $a=100\text{nm}$ , water oil interfacial tension  $\gamma_{ow}=30\text{mN/m}$ .

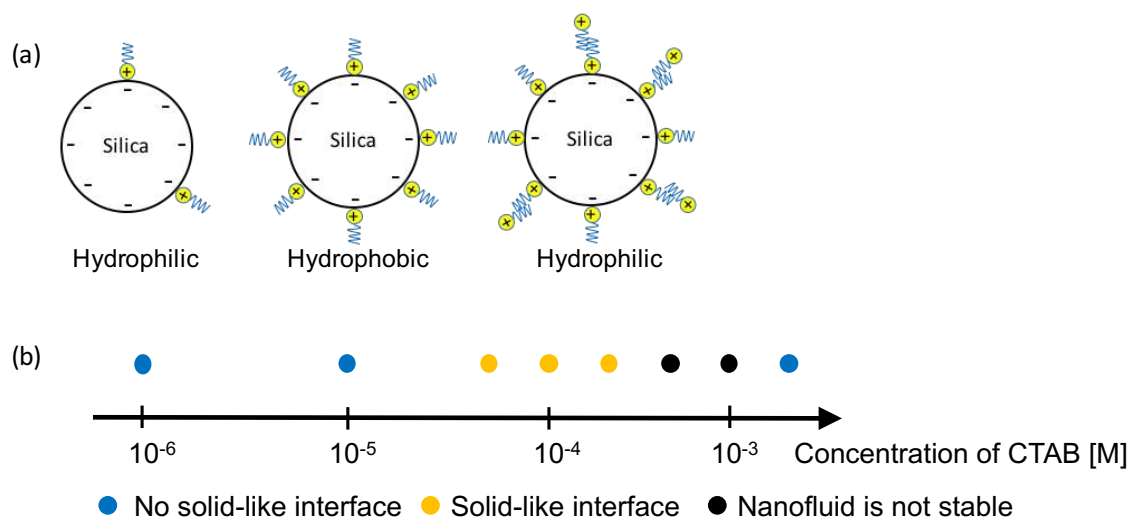


Figure 2.2. Film formation. (a) Particle-surfactant interactions. (b) The formation of the shell-like interface.

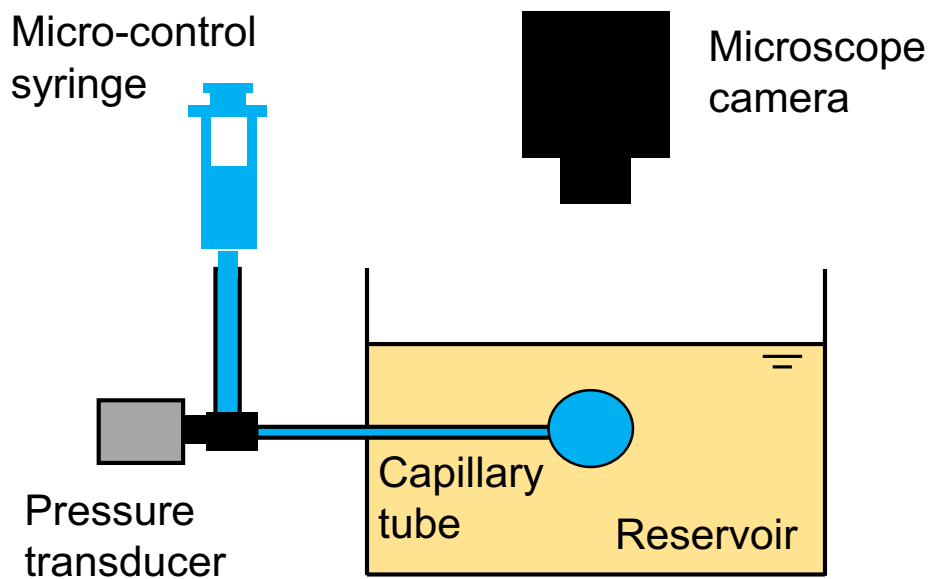
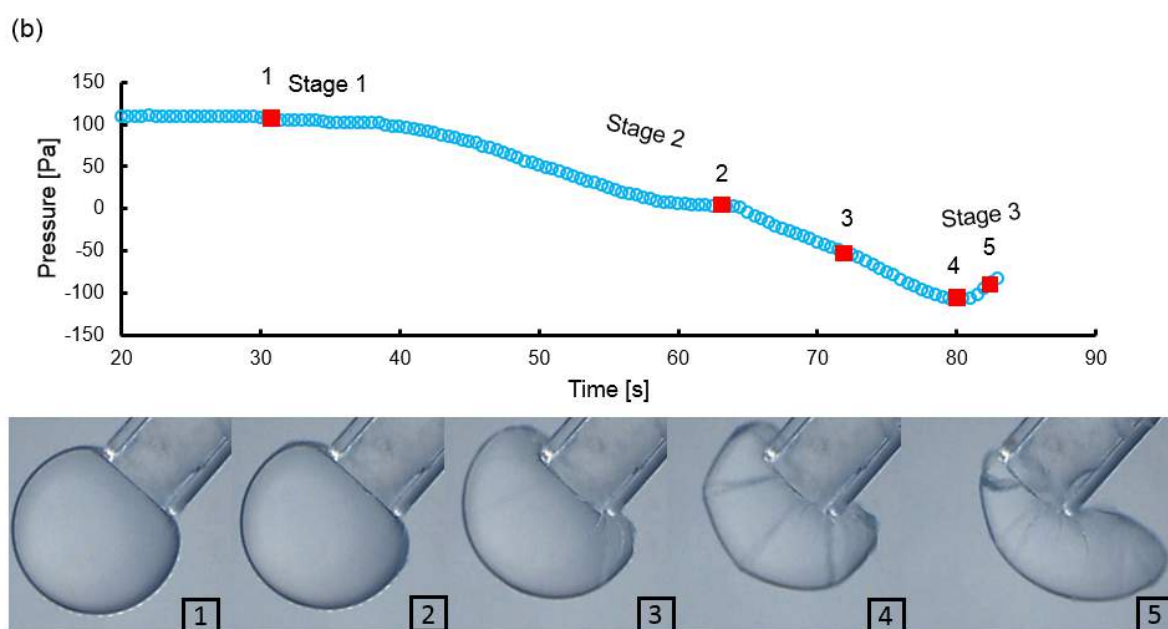
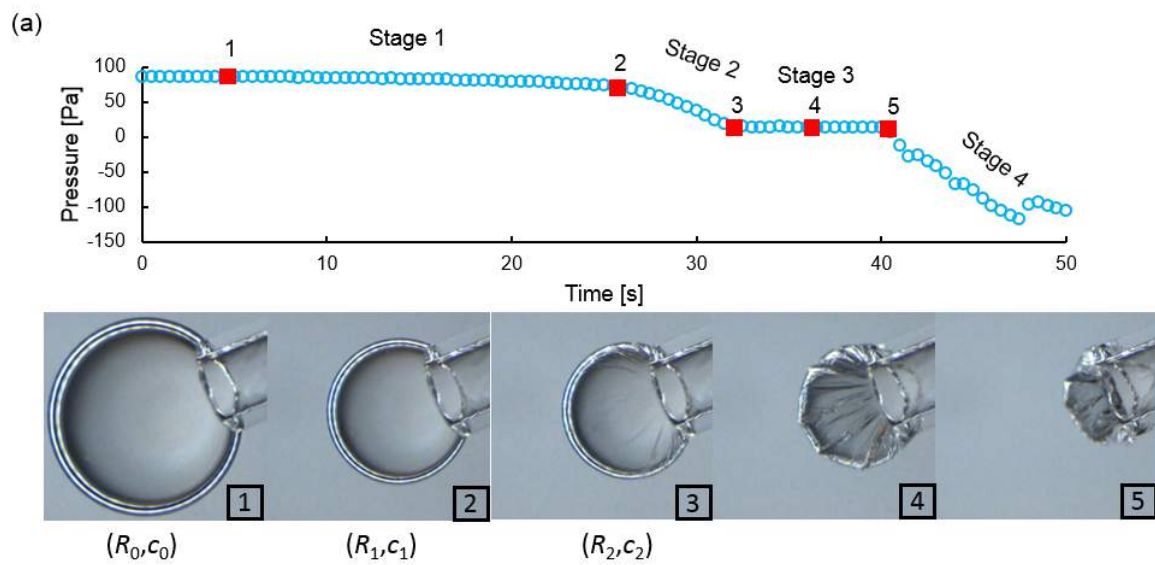


Figure 2.3. Experimental setup.



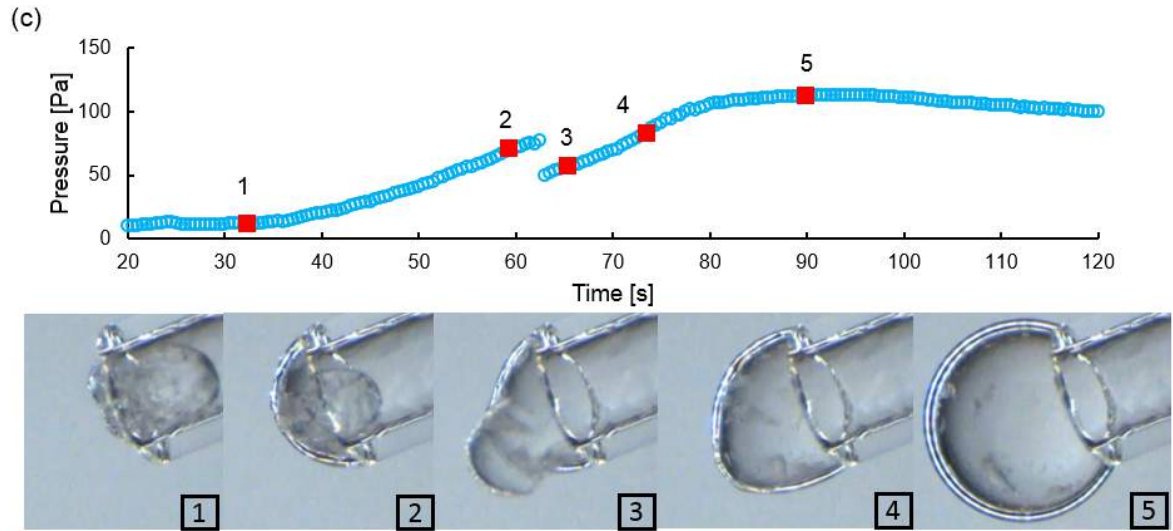


Figure 2.4. Droplet deformation studies. (a) Shrinkage of a nanofluid drop in oil. (b) Shrinkage of an oil drop in nanofluid; (c) Expansion of a nanofluid drop in oil.

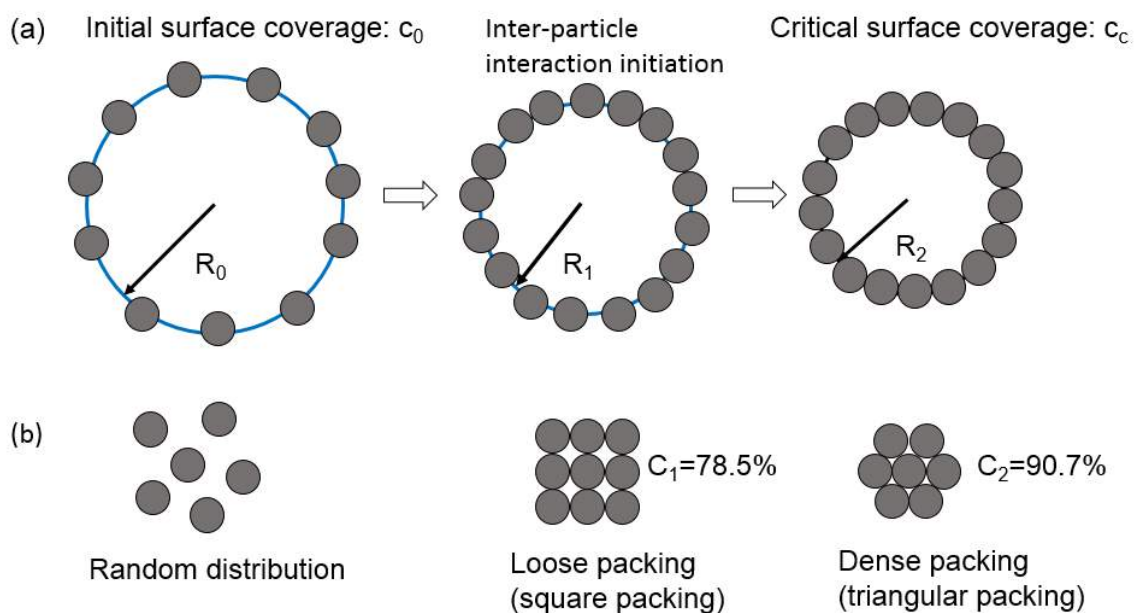


Figure 2.5. The evolution of surface coverage and particle packing during the compression of a particle-coated interface.

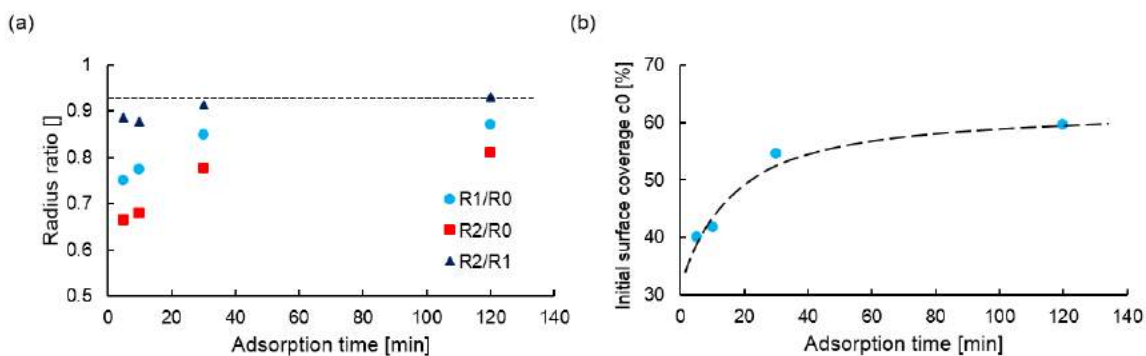


Figure 2.6. Time effects. (a) Relationships between  $R_1/R_0$ ,  $R_2/R_0$ , and  $R_2/R_1$  and adsorption time. (b) Surface coverage as a function of adsorption time.

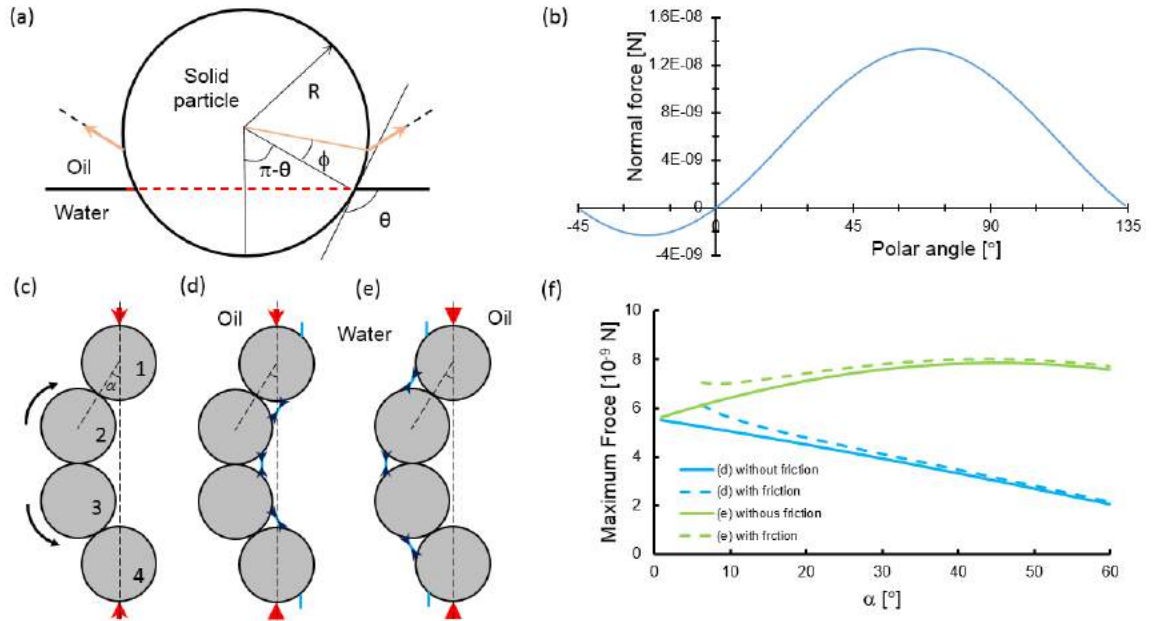


Figure 2.7. Asymmetric behavior. (a) A single particle at the fluid-fluid interface. (b) Capillary force and polar angle. (c)-(e) The deformation of a particle chain with or without particle-interface interactions. (f) The maximum force the particle chain can withstand without deformation. Case parameters: interfacial tension  $\gamma=0.05$  N/m, particle radius  $R=50$  nm, contact angle  $\theta=135^\circ$ , rolling friction  $f=10^{-10}$  N.

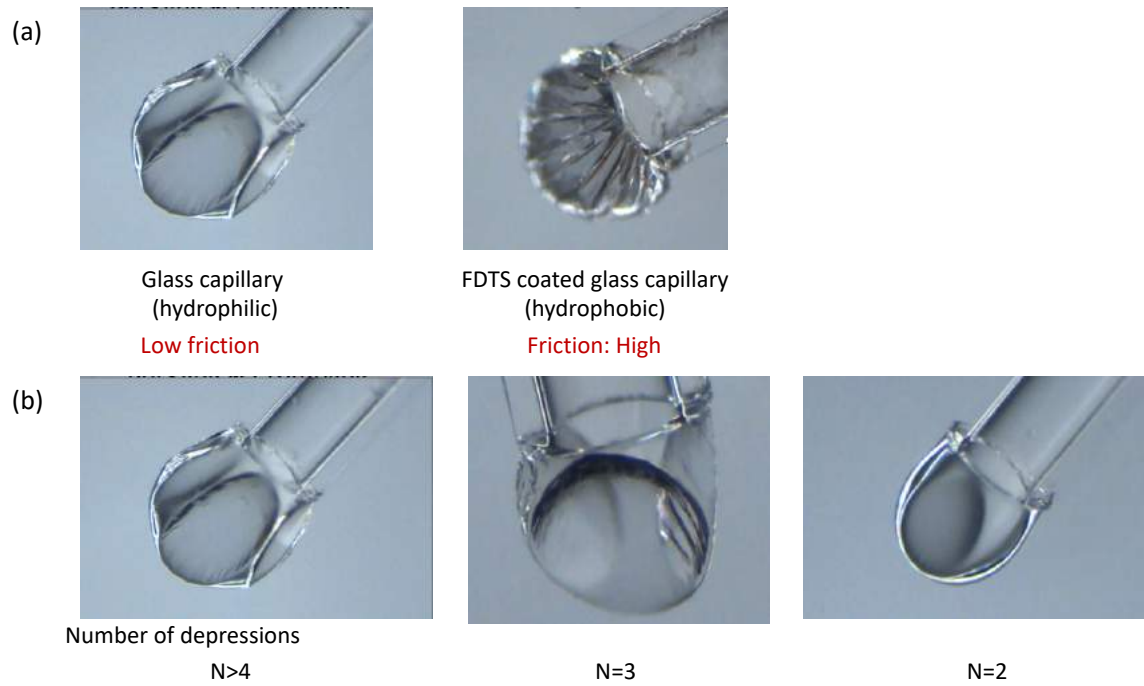


Figure 2.8. Buckling and crumpling patterns. (a) The influence of boundary conditions. (b) The influence of the initial surface coverage: the initial surface coverage increases from left to right.



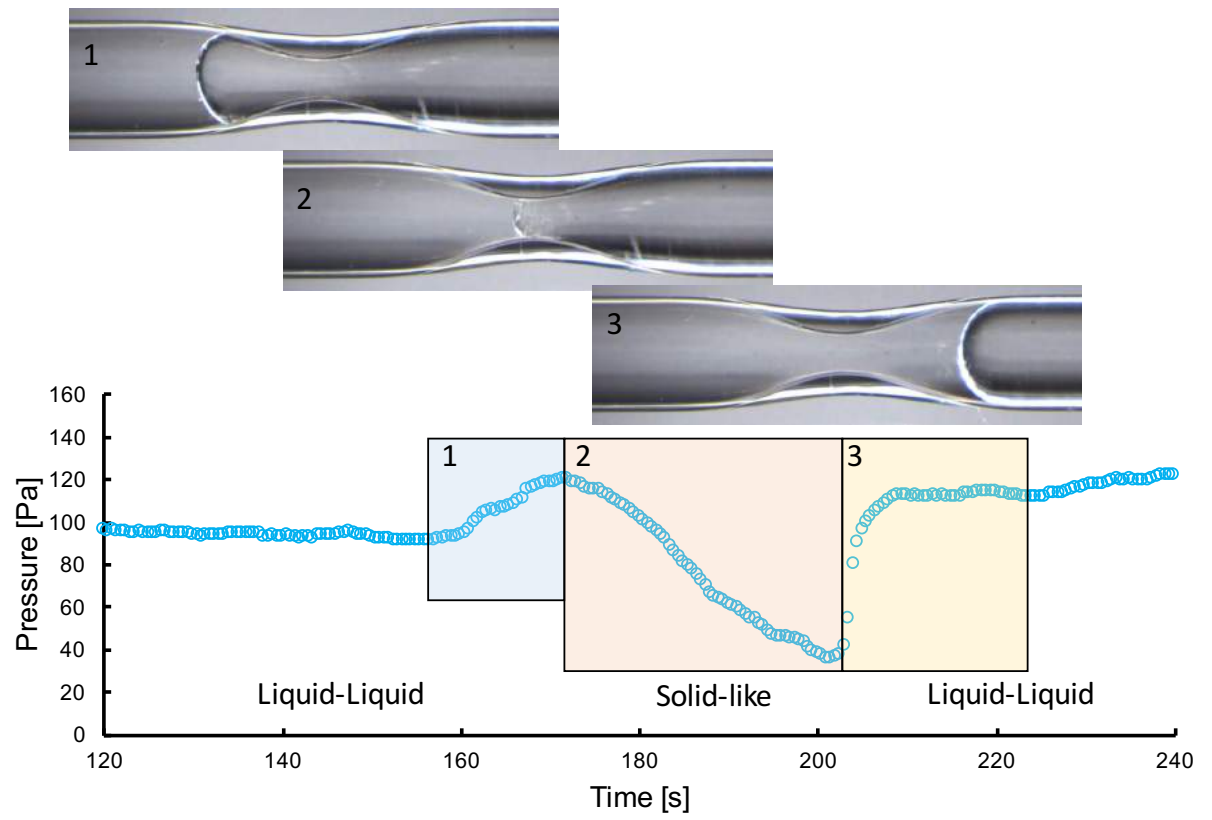


Figure 2.9. The nanoparticle-coated interface traverses a pore throat

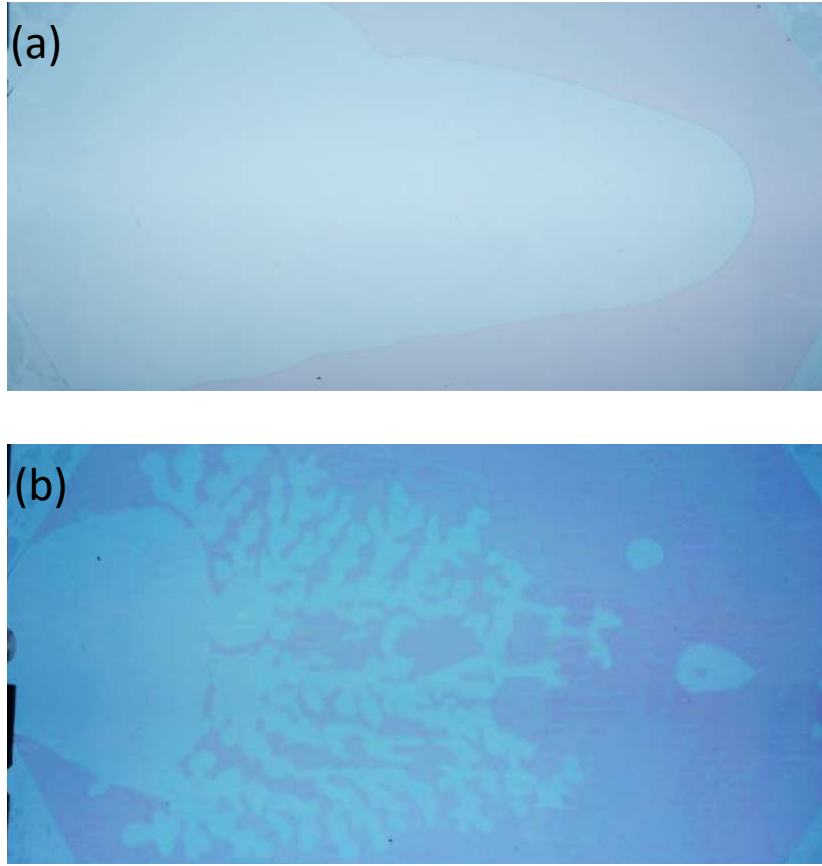


Figure 2.10. Viscous fingering. (a) Normal fingering: water displaces mineral oil. (b) Abnormal fractal fingering: nanofluid (0.5% Silica nanoparticle,  $8 \times 10^{-5} \text{M}$  CTAB) displaces mineral oil.

## **CHAPTER 3. NANOPARTICLE TRANSPORT IN POROUS MEDIA**

### **3.1 Introduction**

Nanoparticles can be engineered for environmental remediation and enhanced oil recovery (Karn et al., 2009; Khin et al., 2012; Ayatollahi and Zerafat, 2012; He et al., 2015). For example, nanoscale zero-valent iron can be used for groundwater remediation and wastewater treatment due to its high specific surface area and surface reactivity (Zhang, 2003; Cundy et al., 2008; Fu et al., 2014). On the other hand, nanoparticles show great potential in enhanced oil recovery (EOR) (Zhang et al., 2014; Roustaei and Bagherzadeh, 2015; Mohajeri et al., 2015; Zhang et al., 2016): wettability alteration (Karimi et al., 2012; Monfared et al., 2016; Al-Anssari et al., 2016), interface tension reduction (Hendraningrat et al., 2013; Mohajeri et al., 2015), enhanced spreading (Wasan and Nikolov, 2003; Nikolov and Zhang, 2015; Luo et al., 2016), and alteration of rheological properties (Newtonian to non-Newtonian, Suleimanov et al., 2011; Wei et al., 2016).

Carbonate reservoirs contain more than 60% of the world's recoverable oil and 40% of the world's gas. In addition, carbonates host 70% of conventional oil reservoirs in the Middle East (Schlumberger, 2007). Laboratory core flooding tests demonstrate that the injection of nanofluids can increase the oil recovery efficiency by almost 10% in carbonate rocks in the EOR stage (Bayat et al., 2014; Roustaei and Bagherzadeh, 2015; Moghaddam et al., 2015).

However, adsorption of nanoparticles onto mineral surfaces is a major constraint for the application requires a long transport distance. Indeed, small size nanoparticles (10-

100 nm) can easily fit through pore throats (Lonoy, 2006), however physiochemical adsorption causes particle retention on the mineral surfaces and the loss of nanoparticles during flow in porous media (McDowell, 1986; Lecoanet et al., 2004; Guzman et al., 2006). In addition, large aggregates form in unstable nanofluids and induce particle straining and clogging (Hendraningrat et al., 2013; Hosseini and Tosco, 2013).

There are only a few experimental studies of nanoparticle transport in carbonates (Petosa et al., 2010). Adsorption of nanoparticles on limestone affects the contact angle between oil and nanofluids and alters the recovery efficiency (Bayat et al., 2014). Adsorption experiments with silica nanoparticles and calcite highlighted strong fluid chemistry effects: decreases in the pH and increases in the ionic strength enhanced the nanoparticle adsorption (Monfared et al., 2015).

This chapter aims to investigate the transport and adsorption behavior of silica nanoparticles in carbonates. We explore the effect of pH, ion concentration, ion type, and run complementary flow experiments through silica sand and carbonate sand to assess the differences between siliceous and carbonate reservoirs. Finally, grain-scale and macroscale analyses provide physical insight into ongoing adsorption and transport processes.

### **3.2 Experimental Study: Materials and Procedures**

### 3.2.1 *Materials*

The silica nanoparticles used in this study are spherical and have uniform particle size of 11 nm (Sigma-Aldrich). The average aggregate size is around 100 nm measured with dynamic light scattering (DLS) analysis of suspended particles (Zetasizer Nano ZS, Malvern Instruments). Nanofluids were prepared by mixing nanoparticles with test solutions and then ultrasonicated for 40mins (Fisher Scientific Model 505 Sonic Dismembrator).

Silica sand or carbonate sand form unconsolidated sand columns. The particle size for both sands is between 0.42 and 0.71 mm, the specific surface is  $\sim 22 \text{ cm}^2/\text{g}$  which assumes spherical particles. The carbonate sand (Jeddah, Saudi Arabia) contains both calcite ( $\text{CaCO}_3$ , 47.2%) and dolomite ( $\text{CaMg}(\text{CO}_3)_2$ , 52.8%) based on XRD analysis (Rigaku MiniFlex 600).

### 3.2.2 *Characterization Methods*

Zeta potential. An electrical double layer forms around a charged particle submerged in water. The zeta potential at the slip plane provides critical information on the electrostatic interactions between particles and the stability or adsorption of particles. The zeta potential of silica nanoparticles and carbonate grains is measured by determining the electrophoretic mobility and then applying the Henry equation (Zetasizer Nano ZS, Malvern Instruments). All samples for zeta potential measurements were prepared at a concentration of 2g per liter.

Concentration. UV-vis spectroscopy (Cary 500 UV-vis-NIR spectrophotometer, Agilent Technologies) determines the concentration of nanoparticles. The absorbance is a function of molar absorptivity  $\epsilon$ , the length of solution the light passes through  $l$ , and the concentration  $c$ .

$$A = \log_{10} \frac{I_0}{I} = \epsilon \cdot l \cdot c \quad (3.1)$$

Figure 3.1(a) shows the UV-vis adsorption spectra of nanofluids with particle mass concentration from 0.1g/L to 2g/L. The absorbance  $A$  at wave length 212nm has a linear relationship with the particle concentration (Figure 3.1(b)).

Scanning electron microscopy. SEM (FEI Quanta 600 FEG) iamges characterize the adsorption layout of nanoparticles on sand grains.

### 3.2.3 Adsorption Column

Figure 3.2 shows a sketch of the adsorption columns, the peristaltic pump, and a fraction collector. The sand column has a length  $L=150\text{cm}$  and a diameter  $D=6.35\text{mm}$ . Silica and carbonate porous media are made by filling the adsorption column with silica sand and carbonate sand. Both porous media have a pore volume of  $18\text{cm}^3$ . The effluent solution is collected by the fraction collector equipped with 80 8ml test tubes (Model 2110, BIO-RAD) for concentration analysis.

All column experiments follow the same test protocol. A slow injection of at least 5 pore volumes of test solution (W/O nanoparticles) saturates the sand column, followed by a

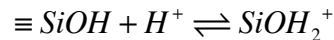
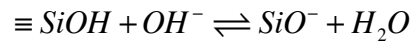
90ml (5 pore volume) injection of nanofluid, at a flow rate of 1ml/min. Finally, 5 pore volumes of test solution flush the sand column. Sands at the inlet and the outlet are dried and characterized by the SEM (Quanta 600 FEG). A tracer test of injecting 0.5M NaCl solution into the deionized water saturated adsorption column provides a reference curve for the advection-dispersion transport and the dispersion coefficient  $D$ .

### 3.3 Results and Analyses

#### 3.3.1 Zeta potential of silica and carbonate grains

The zeta potential of silica nanoparticles and carbonate as a function of both the pH and ionic concentration of the fluid provides quantitative information for the stability (particle-particle interaction) and adsorption (particle-surface interaction) analyses.

Figure 3.3(a) shows the zeta potential of silica nanoparticles at a different pH. The silica nanoparticles are highly negatively charged in alkaline conditions, and become slightly positively charged at low pH. The corresponding pH of a zeta potential of zero is termed the isoelectric point. The isoelectric point of silica is approximately pH=4. In silica particles, the  $\text{SiO}_4^{4-}$  tetrahedron is imperfect. In aqueous suspensions of silica particles, these free bonds are neutralized by  $\text{H}^+$  and  $\text{OH}^-$  and form silanol groups  $[\text{Si}(\text{OH})_n]$ .  $\text{H}^+$  and  $\text{OH}^-$  behave as potential determining ions (PDI) due to the reactions of silanol groups in aqueous suspensions (Junior and Baldo, 2014; Melanson et al., 2001):



Figures 3.3(b) and (c) present the effect of the ion concentration on the zeta potential of silica and carbonate. For both silica and carbonate, NaCl has a negligible effect on the zeta potential until its concentration exceeds 0.01 M. Significant effects were observed at 1 M when the zeta potential of both silica and carbonate reduces towards 0 mV. Compared to NaCl,  $\text{CaCl}_2$  has a more significant effect on the zeta potential of silica and carbonate. The zeta potential reduces even at an extremely low  $\text{CaCl}_2$  concentration ( $10^{-4}$  M). The zeta potential becomes positive when  $c(\text{Ca}^{2+})=1$  M for silica, and  $c(\text{Ca}^{2+})=0.01$  M for carbonate. The binding affinities of alkali cations on the silica surface follow the trend:  $\text{Ca}^{2+} > \text{Mg}^{2+} > \text{K}^+ > \text{NH}_4^+ > \text{Na}^+ > \text{Li}^+$  (Tadros and Lyklema, 1967; Melanson et al., 2001). Calcite is soluble in aqueous solutions and the lattice ions  $\text{Ca}^{2+}$  and  $\text{CO}_3^{2-}$  release into solutions which are PDIs for calcite. There are reactions of carbonate ions that generate  $\text{HCO}_3^-$  (Elimelech et al., 2013). Solubility, which is a function of pH, determines the equilibrium concentration of  $\text{Ca}^{2+}$  and  $\text{CO}_3^{2-}$  in aqueous solutions. Note:  $\text{H}^+$  and  $\text{OH}^-$  are not PDIs for calcite. Experimental studies show that the zeta potential of calcite is independent of the pH if the concentration of calcium remains constant (Al Mahrouqi D et al., 2017).

### 3.3.2 Adsorption behaviour analysed with DLVO theory

For nanoparticles, gravitational and drag forces are negligible compared to particle interactions (Santamarina, 2003). The total interaction energy  $U_T$  describes particle interactions, and is the sum of the London-van der Waals interaction energy  $U_{\text{VDW}}$  and the electrostatic double layer energy  $U_{\text{EDL}}$ :



$$U_T = U_{VDW} + U_{EDL} \quad (3.2)$$

Since the radius of the sand grain is over 1000 times larger than the nanoparticle, the interaction between the two can be treated as a sphere-flat surface interaction. For a sphere with radius  $a$ , and minimum distance  $D$  to a flat surface, the van der Waals interaction energy is (Bhattacharjee and Elimelech, 1997; Guzman et al., 2006):

$$U_{VDW} = -\frac{A_H}{6} \left[ \frac{a}{D} + \frac{a}{D+2a} + \ln\left(\frac{D}{D+2a}\right) \right] \quad (3.3)$$

where  $A_H$  is the Hamaker constant. By linear superposition approximation, the electrostatic double layer interaction energy in a 1:1 electrolyte solution can be expressed as (Adamczyk, 2003; Bhattacharjee and Elimelech, 1997; Israelachvili, 2011):

$$U_{EDL} = 64\pi a \varepsilon_0 \varepsilon_r \tanh\left(\frac{e\psi_s}{4kT}\right) \tanh\left(\frac{e\psi_p}{4kT}\right) \left(\frac{kT}{e}\right)^2 \exp(-\kappa D) \quad (3.4)$$

where  $\varepsilon_r$  is the relative dielectric permeability,  $\psi_s$  is the surface potential of the sphere,  $\psi_p$  is the surface potential of the flat surface,  $k$  is the Boltzmann constant ( $k=1.38 \times 10^{-23}$  J/K),  $e$  is the elementary charge ( $e=1.6 \times 10^{-19}$  C),  $T$  is temperature, and  $\kappa$  is the inverse Debye length:

$$\kappa^{-1} = \left( \frac{\varepsilon_0 \varepsilon_r kT}{2N_A e^2 c} \right) \quad (3.5)$$

where  $N_A$  is the Avogadro number, and  $c$  is the ion concentration for 1:1 electrolytes.

Figure 3.4 presents the normalized interaction energy versus the normalized distance for the silica sphere-silica surface condition computed by the above expressions. In Figure 3.4(a), the surface potential is constant and the energy barrier for adsorption decreases as the ionic concentration increases. The electrostatic double layer repulsion vanishes at high ionic concentrations. The ionic concentration is constant in Figure 3.4(b). The energy barrier is large with a high surface potential and vanishes when the surface potential is smaller than 10 mV.

In summary, the decrease in pH and the increase in the ionic concentration reduces the zeta potential, and the increase in the ionic concentration inhibits the electrostatic double layer repulsion. These effects result in a lower energy barrier and more favorable adsorption/aggregation. These findings are consistent with the results of adsorption column tests presented below.

### 3.3.3 Nanoparticle transport and adsorption behaviour

Silica sand Figure 3.5(a) shows the breakthrough curves for nanoparticles injections with pH=3 and pH=9 solutions in silica porous media. The x-axis of the plot is the injection volume  $V$ , and the y-axis is the relative concentration  $C/C_0$ ,  $C$  and  $C_0$  are the effluent and influent concentrations of nanoparticles respectively. The surface of the silica sand and nanoparticles are highly negatively charged at pH=9 (-60mV in Figure 3.3(a)). The high electrostatic repulsion creates a high energy barrier which prevents the adsorption of nanoparticles. pH=3 is close to the isoelectric point of silica particles at which we expect little repulsion and the energy barrier to vanish (Figure 3.5(b)). Therefore, the nanofluid

with pH=9 exhibits a very slight adsorption, while the nanofluid with pH=3 has a more severe adsorption. The integration of the breakthrough curves provides the mass of nanoparticles transported through the adsorption column. The silica sand column adsorbs 2.2% of nanoparticles in a pH=9 test and 16.7% of nanoparticles in a pH=3 test. Experimental data are fitted with the transport model discussed in subsequent sections.

The sand grains after the pH=3 nanofluid injections are fuzzy in comparison to the clean silica sand examined with the SEM (Figure 3.6). SEM images show a monolayer adsorption of silica nanoparticles onto the surface. We observe that the absorption of nanoparticles at pH=9 is reversible as large amounts of nanoparticles are recovered after flushing. However, the absorption of nanoparticles at pH=3 is irreversible as very little amounts of nanoparticles are released during flushing.

Carbonate sand Figure 3.5(b) shows the breakthrough curves for nanoparticle injections in carbonate porous media at pH=3 and pH=10. The dissolution of calcite and dolomite at pH=3 releases  $\text{Ca}^{2+}$  and  $\text{Mg}^{2+}$  into the aqueous solution and are responsible for the more severe adsorption of nanoparticles compared with the pH=10 solution. Fine particles released from the carbonate porous media interfere in measurements of nanoparticle concentrations and result in  $C/C_0 > 1$  of effluent solutions due to the dissolution of carbonate throughout the injection of pH=3.

Figure 3.5(c) presents the breakthrough curves for nanoparticle injections in carbonate porous media with no salt, 0.01M  $\text{CaCl}_2$ , 0.01M NaCl, and 0.6M NaCl. The addition of salts enhances the adsorption of nanoparticles.  $\text{Ca}^{2+}$  reduces the surface

potential of carbonate more effectively than  $\text{Na}^+$  as it is a PDI of carbonate. As a result, more adsorption of nanoparticles is observed for the  $\text{CaCl}_2$  solution than the  $\text{NaCl}$  solution although the salt concentration is the same ( $C=0.01\text{M}$ ). Although  $C(\text{Na}^+)=0.6\text{M}$  does not reduce the zeta potential to the same level as  $C(\text{Ca}^{2+})=0.01\text{M}$ , we did not observe any break through of nanoparticles in the experiment with  $0.6\text{M}$   $\text{NaCl}$  nanofluid. This is because the high ionic concentration inhibits the double layer repulsion and prompts the adsorption shown in Figure 3.4(a). The vanish of the electrostatic repulsion makes aggregation of particles and multi-layer adsorption more likely to occur.

Figure 3.7 presents the SEM images of carbonate sand grains at both the inlet and outlet after nanofluid injections. Results indicate a monolayer adsorption of nanoparticles on the surface for nanofluids without salt and a multi-layer adsorption of nanoparticles for nanofluid with  $0.01\text{M}$   $\text{CaCl}_2$ . Results indicate thick layers of silica nanoparticles on the surface of the carbonate sand at the inlet for nanofluid with  $0.6\text{M}$   $\text{NaCl}$ . The clean surface of the carbonate sand at the outlet confirms the adsorption of all nanoparticles before the outlet. Both monolayer and multi-layer adsorption were observed in experiments.

Table 3.1 summarizes the adsorption proportions of nanoparticles in carbonate experiments. Generally, silica nanoparticles show a strong adsorption tendency in carbonate sand. Calculations of the adsorption area use the mass of adsorbed particles. In carbonate, monolayer adsorption occurs in injections of  $\text{pH}=10$  solutions without salt. However, the ratio of the adsorption area to the total surface area indicates multilayer adsorption in experiments with salt. A 100% loss of nanoparticles follows the  $0.6\text{M}$   $\text{NaCl}$  injection, in which the ratio of the adsorption area to the total surface area is larger than 3.3. The SEM images confirm these observations.

### 3.4 Transport and Adsorption Model

The general form of the advection-dispersion-adsorption model is:

$$\frac{\partial C}{\partial t} = D \frac{\partial^2 C}{\partial x^2} - v \frac{\partial C}{\partial x} - \frac{\rho(1-w)}{w} \frac{\partial S}{\partial t} \quad (3.6)$$

where  $C$  is the concentration of the solute in units of mass per volume of aqueous phase,  $S$  is the adsorbed phase concentration in units of mass of adsorbed particles per mass of porous medium,  $D$  is the dispersion coefficient,  $v$  is the seepage velocity,  $\rho$  is the solid density of the porous medium and  $w$  is the volumetric water content.

The local equilibrium is assumed between the adsorbed and solution concentrations if the adsorption occurs on a fast time scale compared to that of dispersion and advection. The equilibrium model is:

$$S = k_3 \left( \frac{w}{\rho(1-w)} \right) C \quad (3.7)$$

where  $k_3$  is the equilibrium constant. The instantaneous equilibrium adsorption results in a delay in breakthrough.

On the other hand, a first-order kinetic model can describe the adsorption behavior with adsorption rate  $k_1$  and desorption rate  $k_2$ :

$$\frac{\partial S}{\partial t} = k_1 \frac{\rho(1-w)}{w} C - k_2 S \quad (3.8)$$

The kinetic adsorption leads to not only the delay in breakthrough, but also the plateau concentration decrease (less than the injection concentration).

Experimental results show both a delay in the breakthrough and a decrease in the plateau concentration in breakthrough curves, which indicates that instantaneous equilibrium and kinetic adsorptions coexist in the transport of nanoparticles in porous media. A model which combines equilibrium and kinetic adsorption is below (modified from Cameron and Klute, 1977):

$$\frac{\partial S}{\partial t} = k_1 \frac{\rho(1-w)}{w} C - k_2 S + k_3 \frac{\rho(1-w)}{w} \frac{\partial C}{\partial t} \quad (3.9)$$

The analytical solution for the combined first order irreversible kinetic and equilibrium model is:

$$T = vt / L \quad B = vl / 4D \quad \xi = z / L \quad K_1 = Lk_1 / v \quad K_3 = k_3 \quad C = C_s / C_0$$

$$C(\xi, T) = \frac{1}{2} \left\{ \exp[2B\xi(1-M)] \operatorname{erfc} \left[ \xi(B/T')^{1/2} - M(BT')^{1/2} \right] + \exp[2B\xi(1+M)] \operatorname{erfc} \left[ \xi(B/T')^{1/2} + M(BT')^{1/2} \right] \right\} \quad (3.10)$$

where  $M = (1 + K_1/B)^{1/2}$  and  $T' = T/(1 + K_3)$ .

We applied this model to fit breakthrough curves (Figure 3.5(a) and Figure 3.5(c)). Table 3.2 lists values of the kinetic adsorption rate  $k_1$  and the equilibrium constant  $k_3$  used for modeling.  $k_3$  increases as the tendency of particle adsorption increases;  $k_1$  increases when second or third-layer adsorption occur. Favorable particle depositions on the surface cause instantaneous adsorption for clean sand. However, the charge distribution on the

surface of the sand surface is heterogeneous which may lead to different available adsorption sites in porous media (Song et al., 1994). Adsorption is kinetic when the particle-surface interaction is unfavorable and the possibility of particle capture becomes smaller (Elimelech and O'Melia, 1990). Second and third-layer adsorption is expected to be more difficult to occur than first-layer adsorption and may happen kinetically (Figure 3.8).

### **3.5 Conclusions**

We investigated the transport of nanoparticles in a long granular column, with emphasis on the adsorption onto silica and carbonate substrates. The effect of pH and ionic concentration on the adsorption behavior manifests in breakthrough curves and SEM images, and relates to changes in zeta potential.

particle-surface and particle-particle interactions control the adsorption/deposition of nanoparticles and the stability of nanofluids. The zeta potential is a key measurement for interpretations of electrostatic interactions. The zeta potential of silica is pH dependent; however, other PDIs, e.g.  $\text{Ca}^{2+}$ ,  $\text{Mg}^{2+}$  and  $\text{CO}_3^{2-}$  determine the zeta potential of carbonate rather than the pH. The increase in ion concentration reduces the zeta potential of both silica and carbonate. The effect of pH and ions on the zeta potential reflects the different surface chemistry between the silica and carbonate.

The adsorption tendency can be quantitatively analyzed by the particle-surface interaction energy. The reduction of the surface potential and the increase in ionic

concentration inhibit the electrostatic double layer repulsion and lower the energy barrier for adsorption.

The breakthrough curves show strong adsorption of nanoparticles in low pH solutions in silica sand and high salinity solutions in carbonate sand. The intensity of adsorption is consistent with the adsorption tendency characterized by the zeta potential measurement and DLVO analyses. Alkaline and low salinity conditions (especially PDIs) favor nanoparticles transport in carbonate reservoirs.

The adsorption of nanoparticles is not purely mono-layered. Multi-layer adsorption occurs at a high adsorption tendency. Equilibrium and kinetic adsorption coexist in nanoparticle transport in porous media. A transport model combining both adsorption mechanisms fits the experimental data well. A high adsorption tendency increases the equilibrium adsorption constant and multi-layer adsorption increases the kinetic adsorption rate.



Table 3.1. Mass analyses for the adsorption of nanoparticles in carbonate. Injection fluid: pH=10.

	No salt	0.01M CaCl <sub>2</sub>	0.01M NaCl	0.6M NaCl
Injection mass	0.18g	0.18g	0.18g	0.18g
Collected mass	0.125g	0.063g	0.094g	0g
Trapped mass	0.055g	0.117	0.086	0.18g
Adsorption proportion	30.50%	65%	47.80%	100%
Total surface area	2860cm <sup>2</sup>	2860cm <sup>2</sup>	2860cm <sup>2</sup>	2860cm <sup>2</sup>
Adsorption area*	2887cm <sup>2</sup>	6142cm <sup>2</sup>	4515cm <sup>2</sup>	9449cm <sup>2</sup>
Ratio	1.01	2.15	1.56	3.30

\*Assumption: monolayer adsorption

Table 3.2. Adsorption parameters used in the model.

		Kinetic adsorption rate	Equilibrium constant
		$k_1$ [ $s^{-1}$ ]	$k_3$ []
Silica	pH=3	$6 \times 10^{-5}$	1
	pH=9	0	0.2
Carbonate	No salt	$6 \times 10^{-5}$	1.4
	0.01M NaCl	$1 \times 10^{-4}$	2
	0.01M $CaCl_2$	$2.5 \times 10^{-4}$	2.7

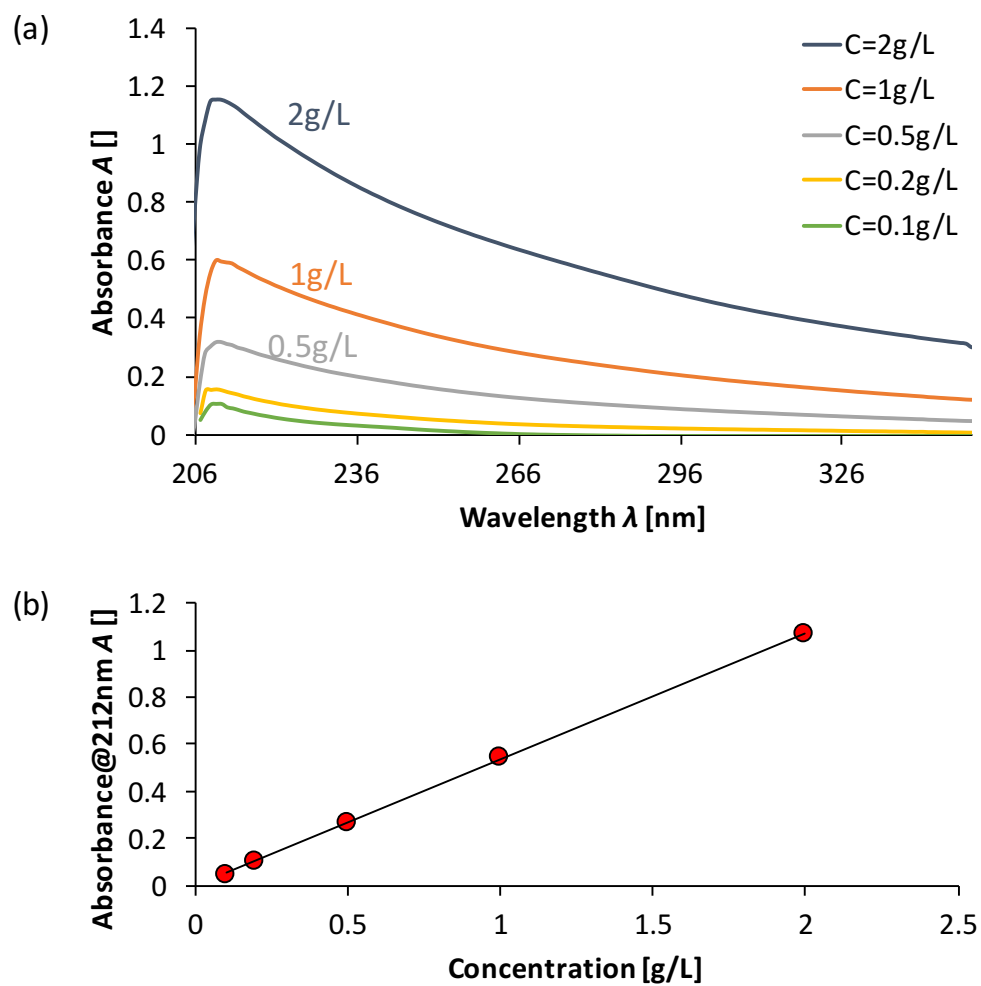


Figure 3.1. Concentration determination. (a) UV-vis adsorption spectra of nanofluids with different concentrations. (b) The linear relationship between concentration and absorbance at 212nm.

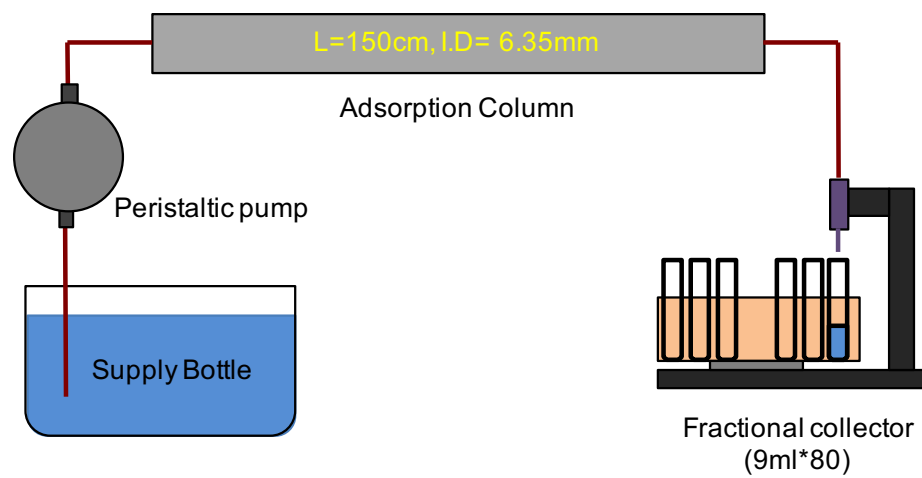


Figure 3.2. Experimental setup.

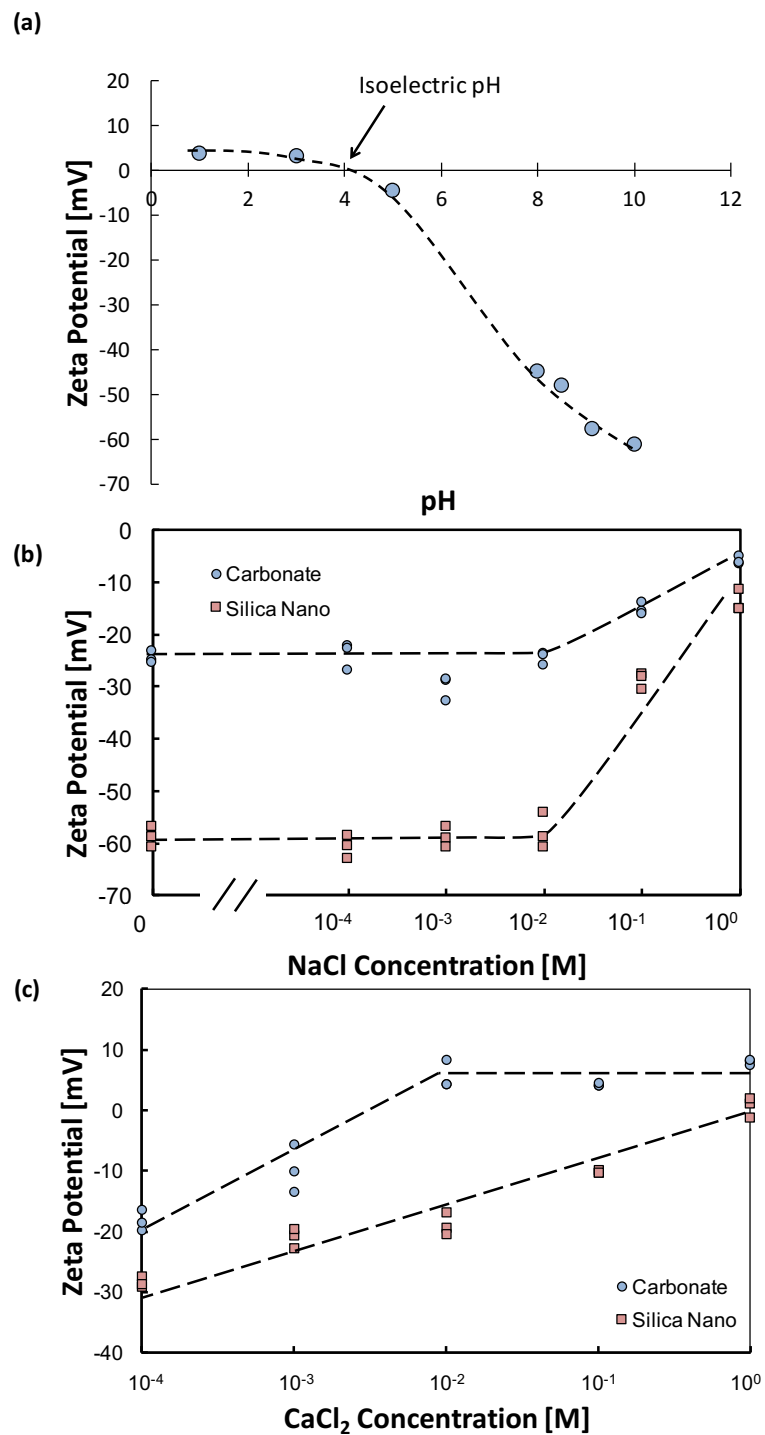


Figure 3.3. The zeta potential of silica and carbonate. (a) Effect of pH on the zeta potential of silica nanoparticles. (b) Effect of NaCl concentration on the zeta potential of silica nanoparticles and carbonate. (c) Effect of  $\text{CaCl}_2$  concentration on the zeta potential of silica nanoparticles and carbonate.

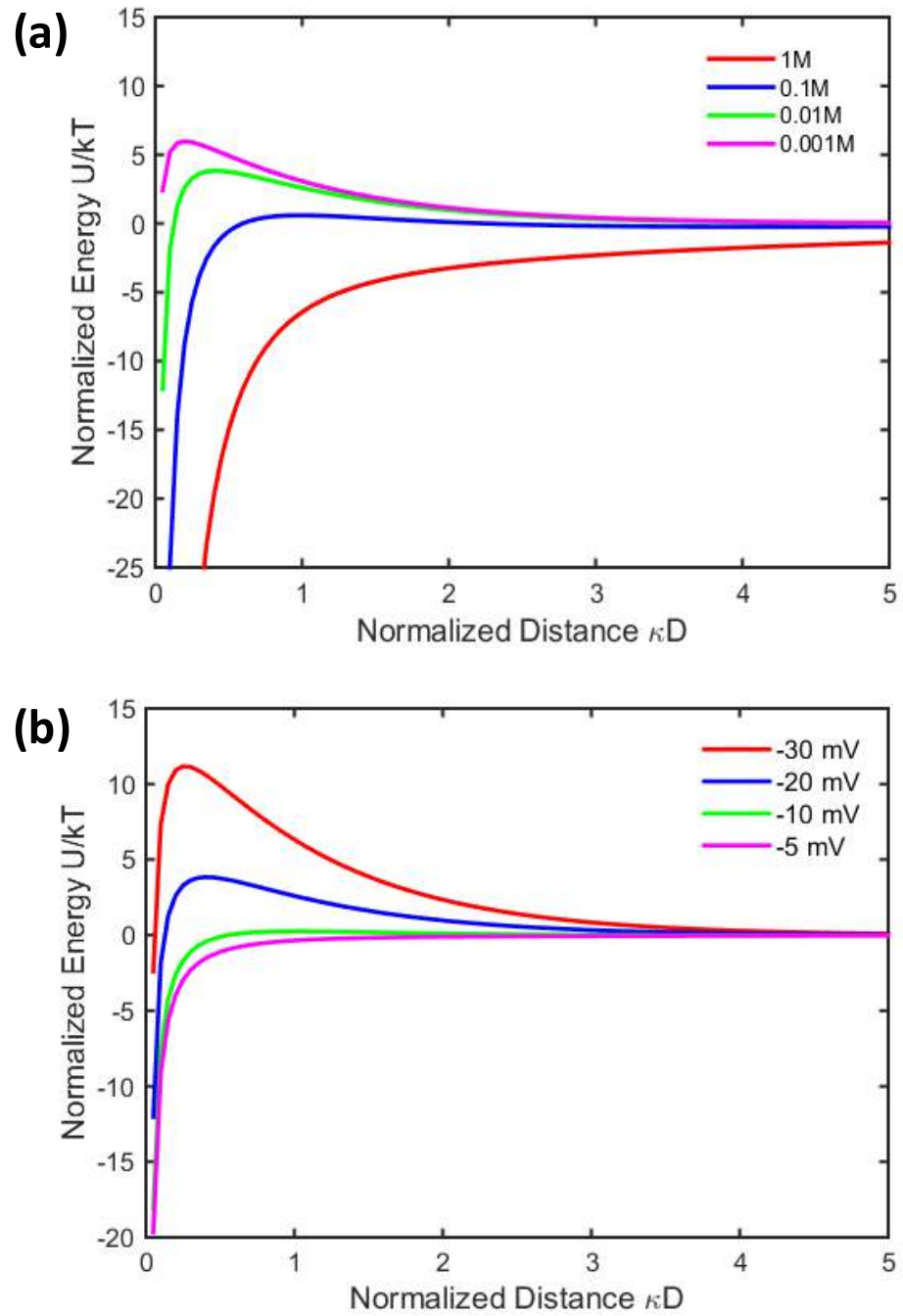


Figure 3.4. Silica particle-surface interaction energy in 1:1 electrolyte solution calculated with DLVO theory. (a) Effect of ionic concentration (constant surface potential). (b) Effect of surface potential (constant ionic concentration).

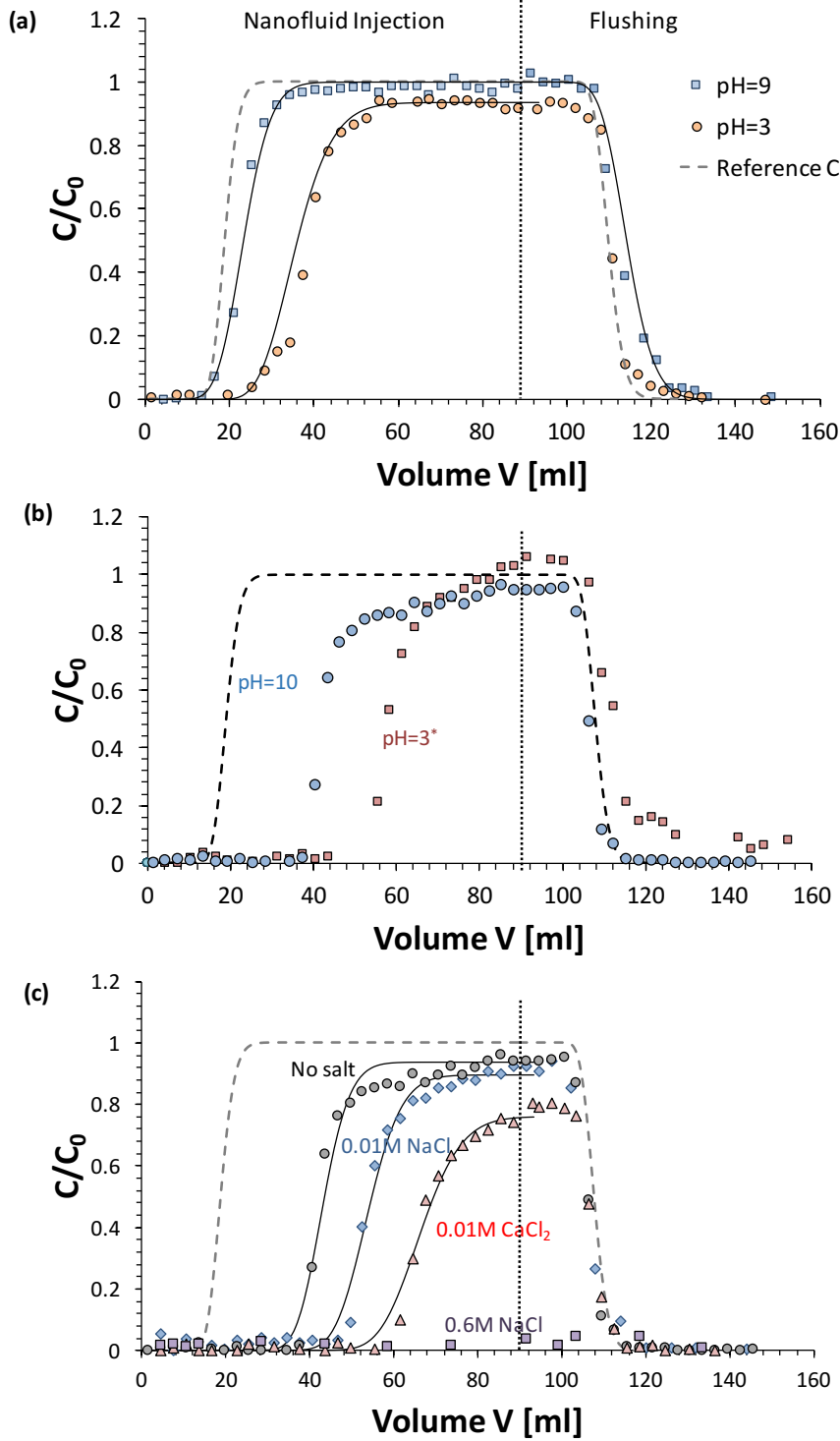
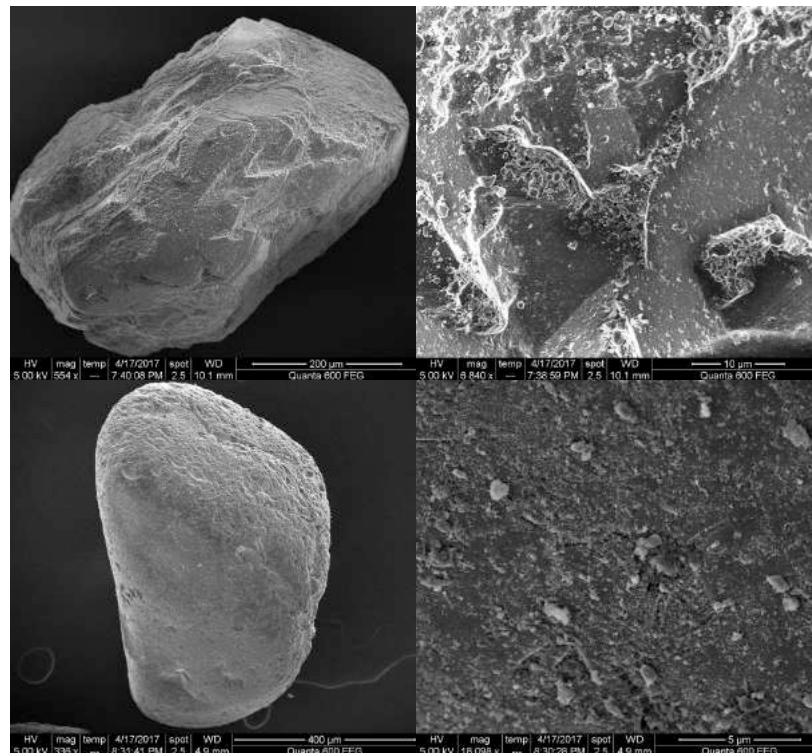


Figure 3.5. Breakthrough curves for adsorption column tests. Dashed lines are reference curves, solid lines are model fittings. (a) Breakthrough curves for nanoparticle injections with pH=3 and pH=9 solution in silica porous media. (b) Breakthrough curves for nanoparticle injections with pH=3 and pH=10 solution in carbonate porous media. (c) Breakthrough curves for nanoparticle injections with pH=10 solution in carbonate porous media. Nanofluids have different salt concentration and types.

Clean Sand



After pH=3 test

Figure 3.6. SEM images of silica sand grains before and after nanofluid injections



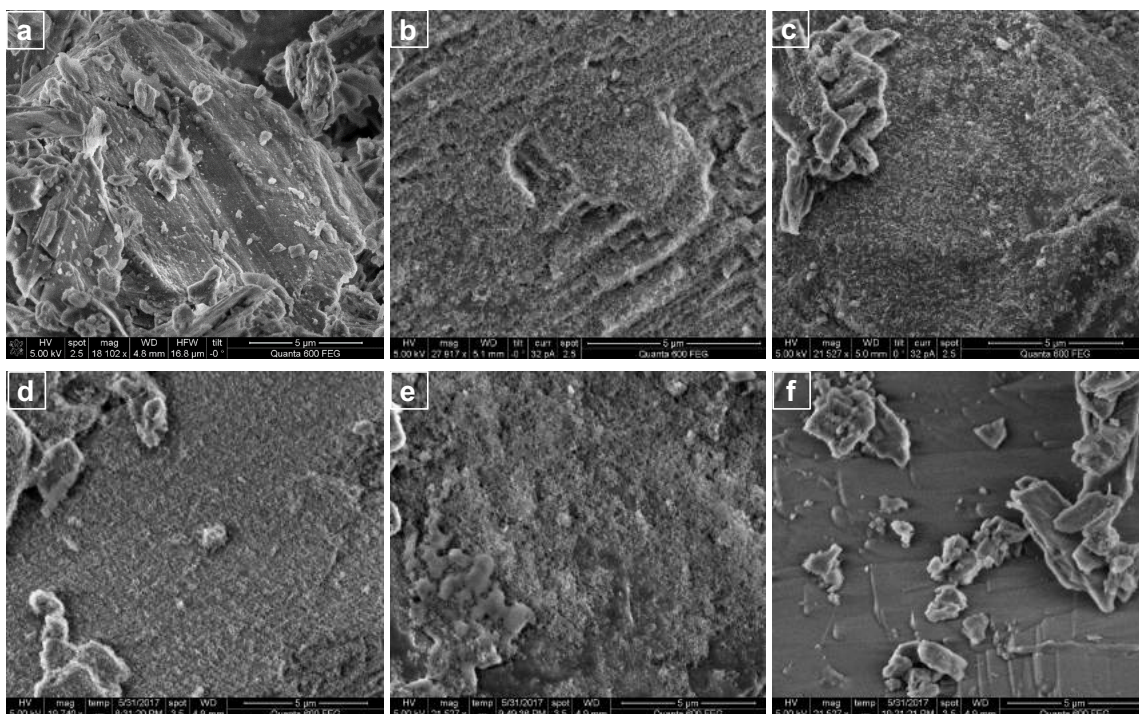


Figure 3.7. SEM images of carbonate sand grains after nanofluid injection and flushing: a)clean carbonate, b)outlet pH=3, c)outlet pH=10, d)outlet pH=10,  $c(\text{CaCl}_2)=0.01\text{M}$ , e)inlet pH=10,  $c(\text{NaCl}_2)=0.6\text{M}$ , f)outlet pH=10,  $c(\text{NaCl}_2)=0.6\text{M}$ .

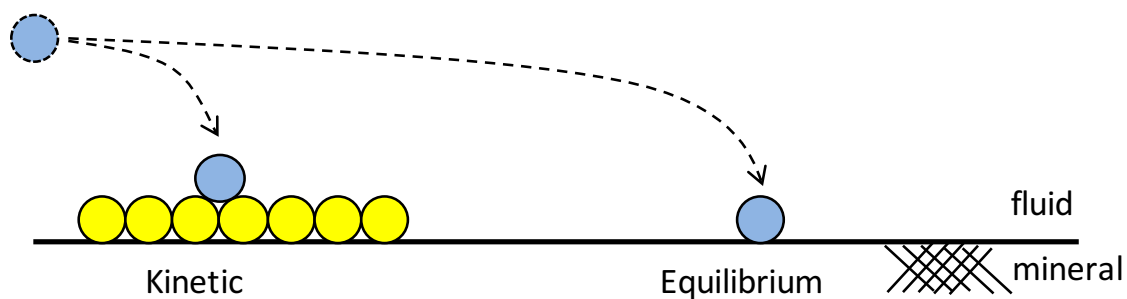


Figure 3.8. Adsorption sites available on the mineral substrate.

## CHAPTER 4. PARTICLE MIGRATION AND CLOGGING IN POROUS MEDIA

### 4.1 Introduction

The migration and retention of fine particles in porous media are fascinating phenomena of both scientific and engineering importance. Fines migration/retention is central to soil erosion (Aitchison and Wood, 1965; Jones, 1971), groundwater flow (Ryan and Elimelech, 1996), oil production (Mungan, 1965; Khilar and Fogler, 1983), and filters (Kenney and Lau, 1986; Reddi *et al.*, 2000). Clogging develops at pore throats and reduces the permeability of the medium, changes flow patterns, and alters particle migration (Muecke, 1979; Krueger, 1988). Clearly, fines migration/retention has important desirable or unwanted-consequences in all these processes.

A migrating particle experiences physical and chemical interactions with fluids, pore walls and other particles inside a porous medium (McDowell - Boyer, Hunt and Sitar, 1986). The resulting particle-level forces include buoyant weight, inertial force during accelerations, drag, and electrical attraction-repulsion forces. In all cases, the constriction-to-particle size ratio  $d_c/d_p$  plays a central role in clogging (Sakthivadivel and Einstein, 1970; Sherard, Dunnigan and Talbot, 1984; Valdes and Santamarina, 2008). Furthermore, clogging depends on the volume fraction of particles (Valdes and Santamarina, 2006; Wyss *et al.*, 2006), inertial retardation (Valdes and Carlos Santamarina, 2007), pore connectivity, path tortuosity (Kampel, Goldsztein and Santamarina, 2009; Bacchin *et al.*, 2014), and variations in the field variations (Valdes and Santamarina, 2006; Zuriguel *et al.*, 2014).

This pore-scale study explores particle migration and retention in radial-flow microfluidic chips. Radial flow is the prevailing flow condition in water extraction and oil production operations. We use direct microscopy observation to identify governing pore-scale phenomena, such as retardation, capture, and clogging. Then we extract statistical data from image analysis to identify underlying causal relationships across multiple clogging events which occur over time. Finally, we implement the observed response on a pore network model.

## 4.2 Particle Retardation and Capture

### 4.2.1 Particle level forces

A migratory particle in porous media experiences drag force, buoyancy, inertia, and electrical interaction forces with pore walls (McDowell *et al.*, 1986). These forces all scale with the size of particle  $d_p$  according to power-law equations in the form  $F = \alpha d_p^\beta$ . The buoyant weight depends on the mass density of the particle  $\rho_s$  and the fluid  $\rho_f$ ;  $F_B = \pi d^3 g (\rho_s - \rho_f)/6$ , where  $g$  is the gravitational acceleration and  $d$  is the particle diameter. The drag force is proportional to the difference between the fluid velocity and the particle velocity,  $F_D = 3\pi\mu d(v_f - v_p)$ , where  $\mu$  is the apparent fluid viscosity. The inertial force is the product of the mass of the particle and its acceleration  $F_I = \pi\rho_s r^3 x''$  (Valdes and Santamarina, 2006). Three dimensionless ratios (Archimedes number  $Ar$ , Froude number  $Fr$ , and Reynolds number  $Re$ ) govern the relative balance among these forces:

$$Ar = \frac{gL^3\rho_l(\rho_p - \rho_l)}{\mu^2} \quad (4.1)$$

$$Fr = \frac{v}{\sqrt{g_0 d_p}} \quad (4.2)$$

$$Re = \frac{vd_p\rho_f}{\mu} \quad (4.3)$$

#### 4.2.2 Particle retardation

Retardation refers to the delay between the particle and fluid displacement in this study. The particle retardation will lead to the gradual increase in particle concentration in most cases. It is obvious that the probability of bridging formation increases with the local particle concentration (Figure 4.1(a)). Several mechanisms are susceptible to particle retardation, which include gravity effects, collisions, inertial effects, flow field disruption, and eddy formation.

Gravity and sliding friction effects Consider a particle of density  $\rho_s$  which migrates through the porous media carried by the fluid with density  $\rho_f$ . If  $\rho_s = \rho_f$ , the particle always flows along streamlines and the local concentration of particles will remain constant everywhere. If  $\rho_s/\rho_f > 1$ , the particle will also fall towards the direction of the gravity field and reach its terminal velocity when the drag force and the buoyant weight reach equilibrium (Figure 4.1(b)).

$$v_T = \frac{d^2(\rho_s - \rho_f)g}{18\mu} \quad (4.4)$$

The particles deposited on the subsurface will slow down due to the collision/sliding friction. The ratio between the particle migration velocity and the terminal velocity:  $v_s/v_T$ , determines the influence of the gravity effect. The gravity effect is negligible when  $v_s/v_T \gg 1$ .

Inertial effect In addition to gravity effects, inertia effects develop as  $\rho_s/\rho_f \gg 1$ . Significant retardation develops at the location where the streamline curves and the flow velocity changes (Figure 4.1(c)). Consider a pore constriction with the sinusoid pore geometry (Figure 4.2(a)). The particle will move downstream according to Newton's law (Kampel, Goldsztein and Santamarina, 2009):

$$\frac{4}{3}\pi\rho_p r_p^3 x'' = 6\pi r_p \mu (v^*(x) - x') \quad (4.5)$$

where  $v^*(x)$  is the average fluid velocity determined by the channel geometry, and  $x'(0) = v^*(0)$ . The particle velocity  $x'$  can be solved by the finite difference method (Figure 4.2(b)). Particles have the same velocity as the fluid at the entrance of the channel. The inertial effect leads to the difference in velocity between the fluid phase and the solid particle phase as the fluid being accelerated and results in more particles entering the constriction (left boundary:  $x=0$ ) than particles leaving the constriction (right boundary:  $x=100$ ) (Figure 4.2(c)). Particles continuously accumulate in the pore body.

### 4.2.3 Particle capture

Particle capture refers to the physical process that occurs when particles come into contact with a solid structure (“collector”) and adhere to the collector’s surface (Figure 4.3(a)). All particles are captured when they contact the collector under the assumption of perfect particle-collector adhesion. The capture efficiency ( $\eta$ ) of a cylindrical collector is defined as the ratio of the number of particle captured ( $N_c$ ) to the number of particles ( $N_a$ ). In general, capture efficiency depends on four parameters:

$$\eta = \frac{N_c}{N_a} = \eta(R_p / R, \rho_p / \rho_l, Re, Pe) \quad (4.6)$$

where  $R_p$  and  $R$  are the radius of particles and the collector,  $Re$  is the Reynolds number of the collector and  $Pe$  is the Péclet number for particle transport. Values of these parameters define three particle capture mechanisms (Sheldon, 2000): inertial impaction, diffusional deposition and direct interception. Particle inertia can be neglected for neutrally-buoyant particles. Brownian diffusion is also small relative to direction interception unless  $Re$  and  $Pe$  are small (Friedlander, 1967). Direct interception is recognized as the most important capture mechanism (Palmer *et al.*, 2004). It assumes that particles follow streamlines exactly and have a negligible influence on the flow field.

The outermost streamlines that permit capture of a particle are the limiting streamlines for that particle (Figure 4.3(a)) The capture efficiency by direct interception ( $\eta_{DI}$ ) is defined as:

$$\eta_{DI} = \frac{2h}{D} \equiv \frac{h}{R} \quad (4.7)$$

where  $2h$  is the distance between the upstream limiting streamlines. The radial velocity of any captured particle should be negative (towards the cylinder surface). Therefore, particles capture can only occur on the front of the collector within  $-\alpha_c \leq \alpha \leq \alpha_c$ , where  $\alpha_c$  is the maximum angle of capture. The particle capture efficiency of direct interception  $\eta_{DI}$  can be expressed as a function of  $r_p = R_p/R$  and  $Re$  (Espinosa-Gayosso *et al.*, 2012):

$$\eta_{DI}(r_p, Re) \approx \frac{1}{2.002 - \ln(Re) + f(Re)} \frac{r_p^2}{(1 + r_p)^{k(Re)}} \quad (4.8)$$

where

$$f(Re) = 0.953 \ln(6.25 + Re) - 1.62$$

$$k(Re) = 0.872 \ln(19.1 + Re) - 1.92$$

Figure 4.3(b) shows that the particle capture efficiency of direct interception  $\eta_{DI}$  increase with increased  $Re$  and  $r_p$  (valid for  $Re \leq 47$ ).

### 4.3 Experimental Study: Materials and Methods

#### 4.3.1 Fabrication of microfluidic chips

We use soft lithography to fabricate the radial flow microfluidic chip with radial symmetry. The process includes: (i) mask design with computer-aided design software, (ii) mask printing, (iii) fabrication of the silicon wafer master with negative photoresist (SU-8 2050),

(iv) polymerization of polydimethylsiloxane (PDMS) using the master as a mold, (v) bonding of the PDMS slabs to a glass substrate with the use of oxygen plasma (Figure 4.4, see Mazutis et al. 2013 for a detailed protocol). Figure 4.5 illustrates the chip design. The microfluidic chip consists of sixty  $300\text{ }\mu\text{m}$  disk-shaped “grains” separated by  $d_c=40\text{ }\mu\text{m}$  wide pore constrictions; all pore channels are  $50\text{ }\mu\text{m}$  high (Figure 4.5(b)). The empty space above the porous-network pattern ensures a uniform flow field.

#### 4.3.2 Materials

The migrating glass particles (Sigma-Aldrich, specific gravity  $G_s=2.60$ ) and polystyrene latex particles (Magsphere,  $G_s=1.05$ ) are either  $d_p=10\text{ }\mu\text{m}$  or  $5\text{ }\mu\text{m}$  in diameter to simulate constriction-to-particle size ratios  $d_c/d_p=4$  and  $8$ . All particle suspensions are prepared with D.I. water of  $0.2\%$  mass concentration.

#### 4.3.3 Test protocol

Figure 4.6 shows the experimental setup. We saturate the microfluidic chip with D.I. water (trapped air escapes through the gas permeable PDMS walls), and use a peristaltic pump (PeriWave microfluidic pump) to withdraw the suspensions from the central port at a constant flow rate. A micro pressure sensor (uPS0250, LabSmith) monitors the pressure at the central port. We use a magnetic stirrer to stabilize suspensions from settlement or coagulation. Digital video microscopy records particle movements within pores and emerging clogging patterns under convergent radial flow at the chip-scale.



#### 4.3.4 Image analysis

Image processing automatically determines the clogging events at chip-scale to interpret their spatial and temporal correlations. The entrance area of pore-network is not included to eliminate boundary effects. A total number of 1078 constrictions parallel to the flow direction are monitored. We extract the image of each constriction and interpret its grey value distribution (Figure 4.7(a)). The clog/unclog state is determined by: 1) the differences between the maximum, minimum and Otsu threshold grey values; 2) the total number of pixels in the dark area. Figure 4.7(b) shows an example of plugged constrictions (red circles) identified by the image analysis algorithm.

### 4.4 Results: Clogging at the Pore-scale

The formation of clogging at the pore-scale is explored first. 10  $\mu\text{m}$  glass and latex particles readily bridge across pore constrictions ( $d_c/d_p=4$  - Figure 4.8 (a) and (c)). A few clogged pore constrictions gradually appear for the 5  $\mu\text{m}$  latex particles ( $d_c/d_p=8$ - Figure 4.8(d)). Two distinct mechanisms are responsible for the clogging at pore constrictions for glass particles and latex particles: *direct bridging* and *particle deposition* (Figure 4.9).

Direct bridging requires high particle fraction. Fluid flow in a porous media involves sudden changes in both the flow rate and direction across constrictions and sharp turns. Glass particles deposit on the glass substrate and slow down due to friction at high terminal velocity. Non-buoyant glass particles deviate from flow lines (inertia versus drag forces) and collide against pore walls. Therefore, glass particles experience retardation in

tortuous flow paths and there is a gradual increase in the local mass fraction of migrating particles. The particles slow down relative to the flow at pores and accumulate at constrictions as illustrated in Section 2. Figure 4.8(a) shows the high particle concentration in pore spaces. High local concentrations near pore constrictions facilitate the formation of granular bridging.

On the other hand, quasi-buoyant latex particles ( $G_s=1.05$ ) follow flow lines and experience negligible retardation. There is no visible local increase in particle concentration throughout the radial flow microfluidics chip. However, we observe that the latex particles can be captured by the PDMS walls which result from direct interception. The hydrophobic interaction between PDMS and latex enhances the particle-surface adhesion (Cejas *et al.*, 2017). The hydrophobic interaction is also responsible for particle-particle interaction which results in aggregates near constrictions. Captured particles reduce the size of openings and facilitate bridge formation (Figure 4.9(b)). The time-lapse photos recorded in the experiment clearly demonstrate the deposition-clogging process of multi constrictions (Figure 4.10). This deposition-clogging mechanism even occurs in tests with a large particle-opening size ratio ( $d_o/d_p=8$ , 5  $\mu\text{m}$  latex particles, Figure 4.8(d)).

#### 4.5 Results: Clogging at the Meso-scale

Clogging in the porous network reflects the underlying changes in local particle concentration, flow rate and pressure. Newly clogged pores alter flow conditions in nearby open paths (i.e., tortuosity), affect retardation and local particle concentration (Figure

4.11). The permeability reduction, clogging development, and the interaction between clogging events are investigated at the meso-scale use advanced image analysis.

#### *4.5.1 Permeability reduction*

Clogging gradually reduces the permeability of the porous medium because there are fewer open pore throats and there is an increase in global tortuosity. Two stages describe this procedure (Figure 4.12). Stage-1: clogging occurs randomly throughout the chip. Then, the higher probability of dependent clogging promotes the growth of clogging clusters. The localized clogging patterns lead to an effective permeability reduction. The most significant feature of this stage is that permeability decreases almost linearly with the increase of the clogging numbers in a semi-log plot. Permeability reduced by 85% when half of the constrictions were clogged. Stage-2: the increase of clogging numbers slows down. However, the rate of permeability reduction speeds up. A few available flow paths have a very large flow rate and display tortuosity after extensive clogging. Then, the pivotal pore throats for these paths begin to block. By the end of the experiment, a few plugs occurred and completely blocked the chip at a certain distance from the discharge point.

#### *4.5.2 The effect of flow rate*

Particle injection tests with flow rate 20  $\mu\text{L}/\text{min}$ , 40  $\mu\text{L}/\text{min}$ , and 60 $\mu\text{L}/\text{min}$  reveal the influence of the flow rate on the clogging behaviours of glass and latex particles. Figure 4.13 plots the distributions of the Reynolds number ( $\text{Re}=\rho\text{UD}/\mu$ ) in the microfluidic chip under different flow rates. The Reynolds number varies from 1 to 35 in experiments.

Glass particles Figure 4.14(a) shows the relationship between the total clogging number and the permeated volume of 10  $\mu\text{m}$  glass particles. The parameter permeated volume is used instead of time to ensure that the same amount of particles transport through the microfluidic chip under different flow rates. After the injection of 600 pore volumes particle suspension, the total clogging numbers of 20  $\mu\text{L}/\text{min}$ , 40  $\mu\text{L}/\text{min}$  and 60  $\mu\text{L}/\text{min}$  respectively are 632, 339, and 170. A High flow rate leads to less total clogging number under the same permeated volume. The increased flow rate raises the ratio between the transport velocity and the terminal velocity of particles  $v_s/v_T$ . High  $v_s/v_T$  minimizes the effect of gravity effect on particle retardation. The large hydrodynamic force generated by the high flow rate also destabilizes the formation of multi-grain bridge.

Latex particles Surprisingly, the flow rate has a reversed effect on the clogging behavior of latex particles compared to glass particles (Figure 4.14(b)). The total clogging number increases with the increased flow rate in the range 20  $\mu\text{L}/\text{min}$ ~60  $\mu\text{L}/\text{min}$ . A high flow rate actually promotes the formation of clogging.

High flow velocity compresses streamlines and increases particle capture efficiency by direct interception. Figure 4.2(b) shows that the particle capture efficiency increases with increased Reynolds number. Single channel microfluidics studies evidence that high flow rates promote the deposition of latex particles on PDMS surface (Gudipaty *et al.*, 2011; Dressaire and Sauret, 2017).

#### 4.5.3 *The effect of radial flow*

Radial flow is the prevailing flow condition in underground water extraction and oil production. The spatially varying velocity field inherently influence the transport and retention of particles.

Glass particles Gravity plays the most critical role in particle retardation and further extensive clogging for glass particles. The radial flow feature of the chip causes the fluid velocity to increase with the decrease in the distance from the central port. As the flow velocity increases, particles experience weaker retardations. Figure 4.15(a) plots the row clogging ratios per unit pore volume suspension. It is clear that the probability of clogging decreases with a decreased distance from the central port, which is consistent with the conclusion from the effect of flow rate.

The formation of a clogging results from the clogging probability and number of particles traversing the constriction. Although the clogging probability decreases towards the center, the number of particles traversing a constriction increases as  $r$  decreases. These two counter effects make the clog clogging ratio remain uniform throughout the chip at three different flow rates: 20, 40, and 60  $\mu\text{L}/\text{min}$  (Figure 4.15(b)), which indicates that clogging growth is nearly homogeneous in the chip.

Latex particles Figure 4.16 shows the evolution of the distribution of row logging ratios along the radius direction at the flow rate= 60  $\mu\text{L}/\text{min}$ . The row clogging ratio increases with the decreased distance from the central port (0 to 100 PV). The latex particles experience negligible retardation and the velocity variation caused by the radial flow

mainly alters the particle capture efficiency. High flow velocity increases the particle capture efficiency. However, clogging is less likely to develop when the number of constrictions which remain open in each row is small ( $<7$ ). The high local pressure difference may prevent the formation of a stable bridge.

## 4.6 Dependent Clogging: Image Analyses and Simulations

Clogged pores may alter flow conditions in nearby open paths (i.e., tortuosity), affect retardation, and promote associated changes in local particle concentration.

### 4.6.1 *Experimental results*

We apply the image processing algorithm to automatically recognize underlying relationships across multiple clogging events which occur over time. “Dependent” and “independent” cloggings are defined here to clarify this process. A new clogging is ‘dependent’ if one or more of its closest constrictions were clogged, otherwise the new clogging event is “independent” (Figure 4.17). The occurrence probability of each clogging type in every five minutes is calculated as  $P = \Delta N / N_{\text{ava}}$ , where  $\Delta N$  is the incremental number of clogged pore constrictions, and  $N_{\text{ava}}$  is the number of pore constrictions that remain available to develop dependent/independent clogging.

Figure 4.18 shows the dependent and independent clogging probability of glass particles under the flow rate 20  $\mu\text{L}/\text{min}$ , 40  $\mu\text{L}/\text{min}$ , and 60  $\mu\text{L}/\text{min}$ . Dependent clogging is dominant in all three experiments. Figure 4.19 shows the dependent and independent clogging probability of a latex particle under the flow rate 40  $\mu\text{L}/\text{min}$  and 60  $\mu\text{L}/\text{min}$ . In

general, dependent clogging is less significant for latex particles due to the different clogging mechanisms for glass and latex particles.

Clogging promotes retardation in the surrounding region with increase in the variation of flow rate and direction. Then retardation increases the local concentration of particles and accelerates the nearby clogging formation. However, the variation of flow rate and direction has a limited influence on the capture of latex particles at the pore constriction.

#### 4.6.2 Pore network simulation

The pore network model provides a convenient tool for the simulation of clogging at the pore scale. The pore network model used in this study accommodates the increased probability of clogging due to the existence of neighboring clogged pores. This study uses a 50×50 2-D normal square network with a uniform tube radius. The flow rate  $q_{ij}$  at the pore throat between the  $i$ th and the  $j$ th nodes obeys the Hagen-Poiseuille equation:

$$q_{ij} = -\frac{\pi r_{ij}^4}{8\mu l_{ij}} \Delta p_{ij} = -g_{ij} \Delta p_{ij} \quad (4.9)$$

where the  $r_{ij}$  and  $l_{ij}$  is the radius and length of the tube;  $\Delta p_{ij} = p_j - p_i$  is the pressure difference between the  $i$ th and the  $j$ th node;  $\mu$  is the effective viscosity. The mass balance requires that, at each node:

$$Q_i = \sum_{j=\text{throats}} q_{ij} = 0 \quad (4.10)$$

where  $j$  is the number of pore throats connected to node  $i$ . The flow equation is a linear system of the form  $\mathbf{AP}=\mathbf{B}$ , where  $\mathbf{A}$  is generated with tube connectivity  $g_{ij}$ ,  $\mathbf{P}$  is the vector of unknown pressures at internal nodes and  $\mathbf{B}$  includes known boundary pressures.  $\mathbf{P}$  can be solved as  $\mathbf{P}=\mathbf{A}^{-1}\mathbf{B}$ . We obtain the global flow rate  $Q$  by adding the flow rate  $q$  in all tubes that cross a plane normal to the flow direction (Suchomel, Chen and Allen Iii, 1998; Jang, Narsilio and Santamarina, 2011). If a clogging event occurs at the pore constriction between the  $i$ th and the  $j$ th node, then  $g_{ij}=0$ .

Experimental observations suggest that the ratio between the probability of a dependent clog ( $P_{dep}$ ) and independent clog ( $P_{ind}$ ) relies on the particle type and flow rate. The ratio  $P_{dep}/P_{ind}$  indicates the extent of the influence from a neighboring clogged pore throat. Each clogging event is treated as an independent event and the clogging site is randomly selected based on the probability of clogging.

$P_{dep}/P_{ind}=1, 5, 10$  and  $100$  are tested to show the effect of dependent clogging on the permeability reduction and macro-scale clogging patterns. The permeability of the network decreases with an increased clogging ratio which agrees with experimental results. Simulation results suggest dependent clogging lowers the permeability of the porous media more effectively than independent clogging (Figure 4.20).



## 4.7 Conclusions

This study investigates particle migration and retention at pore-scale and meso-scale with microfluidic chips. Pore-scale observations identify different clogging mechanisms for glass and latex particles. Non-buoyant glass particles experience retardation due to gravity and inertial effects. The large local volume fraction of particles promotes the formation of a multi-grain particulate arch at a constriction. Quasi-buoyant latex particles interact with the PDMS walls by direct interception. The attractive van der Waals force and the hydrophobic interaction enhance the particle-surface adhesion. The capture of latex particles by PDMS walls and further aggregates of latex particles at constrictions reduce the constriction size and eventually plug constrictions.

Flow rates have a different influence on the clogging behavior of glass particle and latex particles due to their unique clogging mechanisms. A high flow rate inhibits the formation of clogging of glass particles by diminishing the particle retardation and destabilizing the multi-grain particulate arch. However, a high flow rate promotes the formation of clogging of latex particles since the high flow velocity increases the particle capture efficiency.

The spatially varying velocity field in the radial flow microfluidic chips inherently influences the transport and retention of particles. Glass particles experience more retardation at a larger distance from the central port, which results in a higher probability of clogging. For latex particles, the row clogging ratio increases with the decreased distance from the central port since the large flow velocity promotes particle capture.

Statistical analyses based on advanced image analyses reveal that clogging in porous media is a highly dynamic process and demonstrate the interaction between plugs. The higher occurring probability of dependent clogging leads to localized clogging patterns. Dependent clogging is dominant in the clogging of glass particles, while it has limited influence on the clogging of quasi-neutrally-buoyant latex particles in PDMS microfluidic chips. Pore network simulations show that dependent clogging effectively reduces the permeability and increases tortuosity, compared to independent pore clogging.

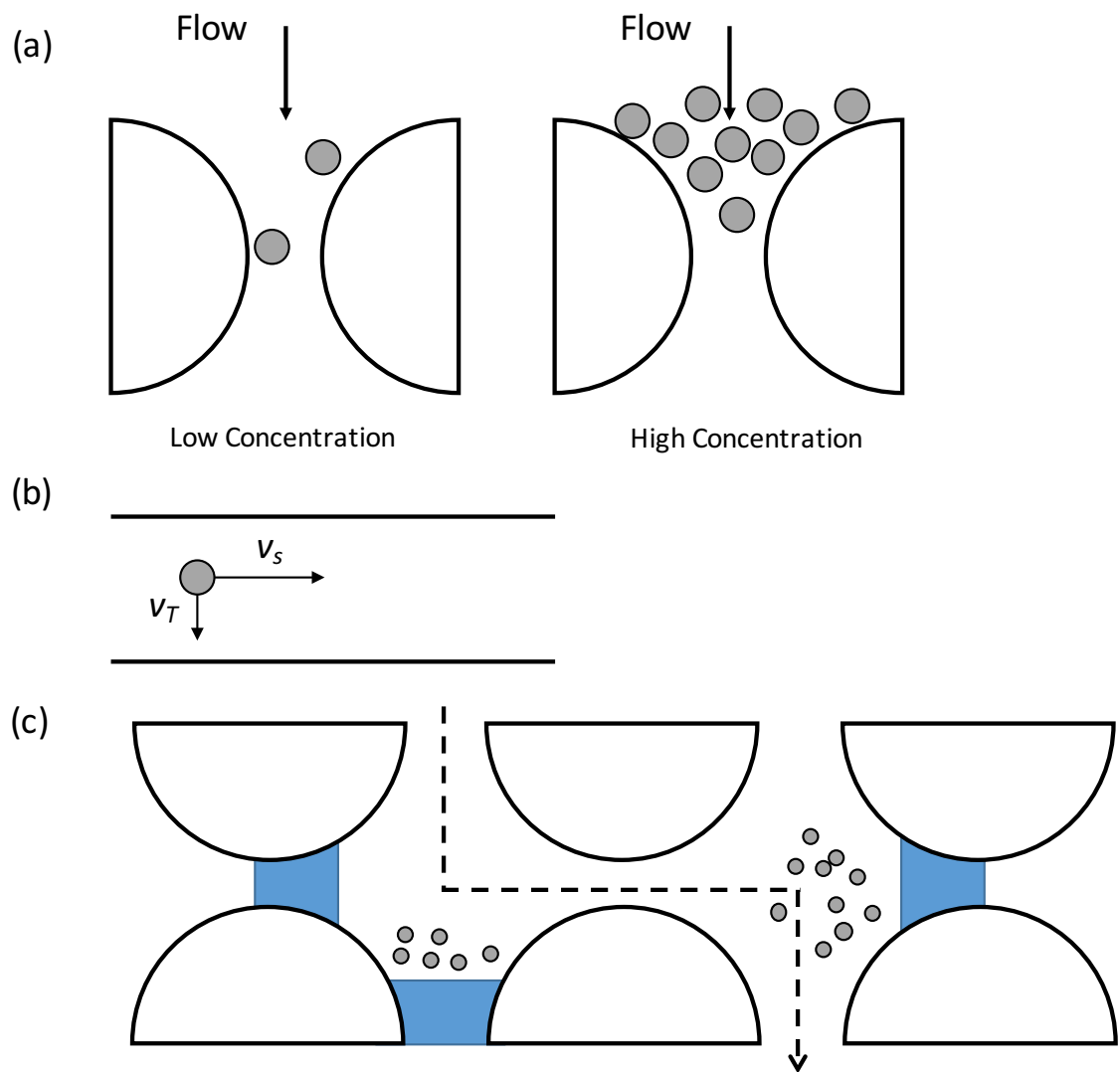


Figure 4.1. Particle Retardation. (a) The effect of local particle concentration on pore throat clogging. (b) Gravity effects. (c) Inertial effects.

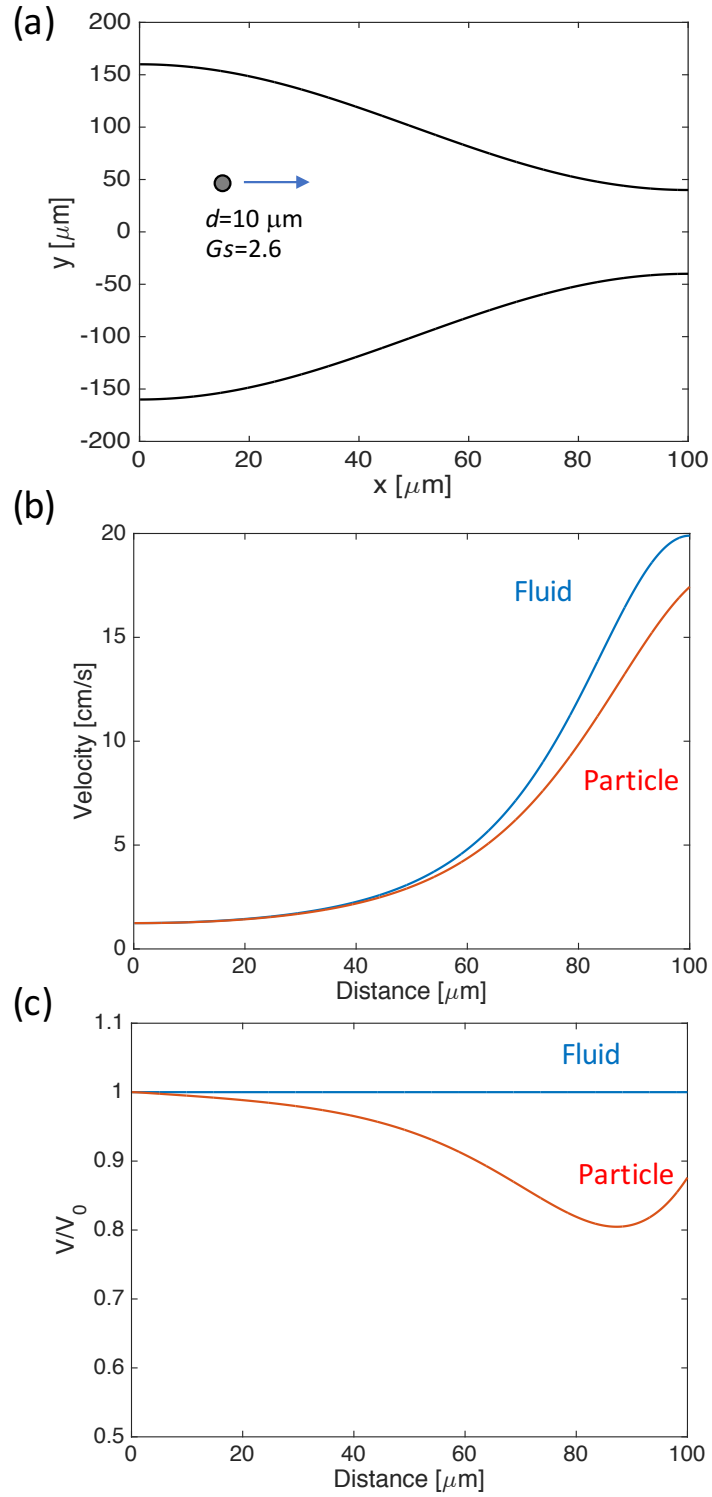


Figure 4.2. Inertial effect. (a) The geometry of the pore constriction. (b) Average fluid velocity and particle velocity along the pore constriction. (c) Particle retention due to the inertial effect

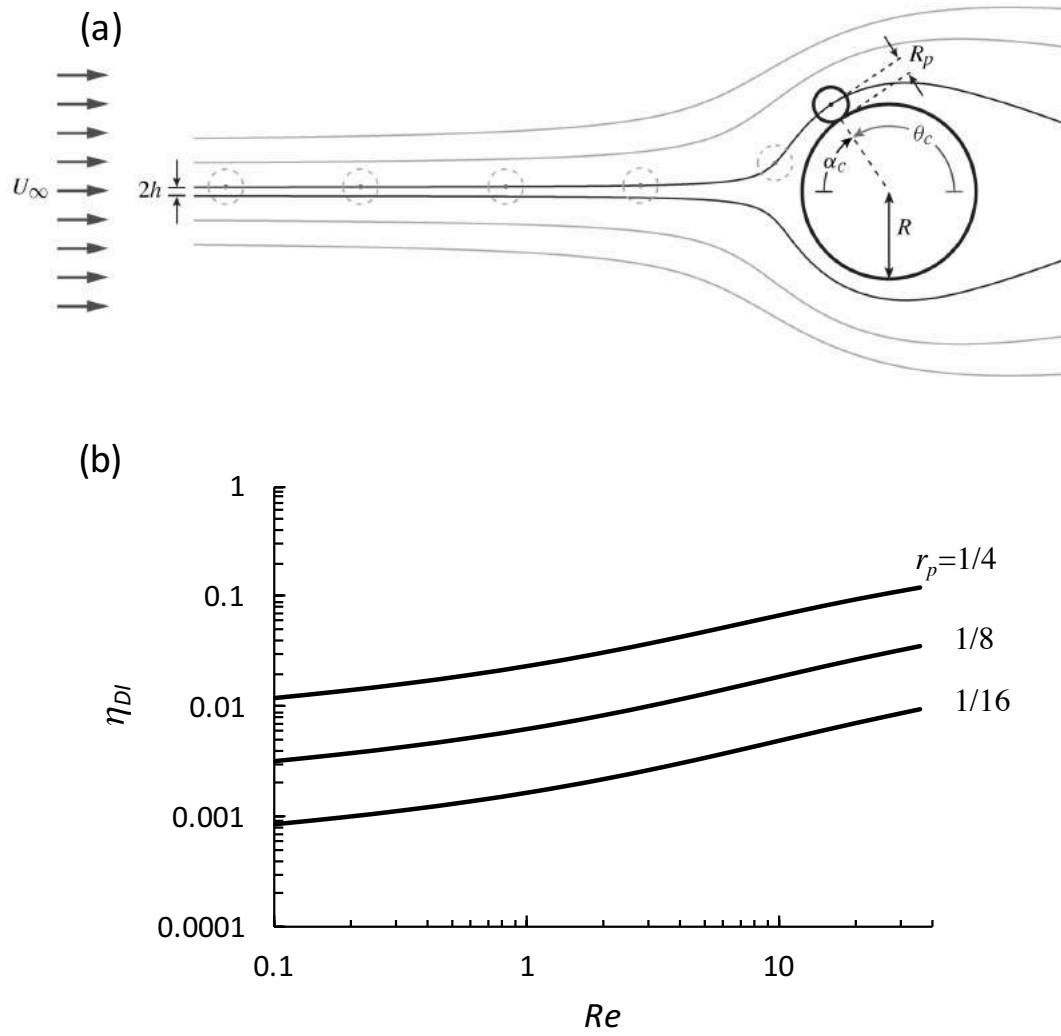


Figure 4.3. Particle capture by direct interception. (a) Sketch of direct interception. The streamlines followed by the particle define the limiting streamline. (b) The particle capture efficiency by direct interception  $\eta_{DI}$  depends on the Reynolds number  $Re$  and the relative radius of the migrating particle  $r_p = R_p/R$ .

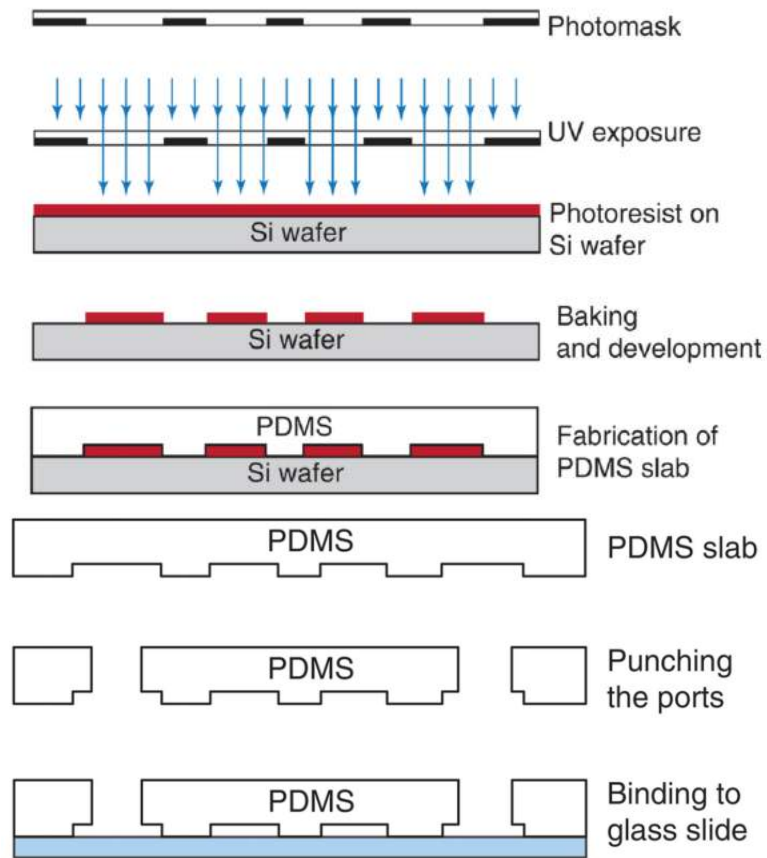


Figure 4.4. Soft lithography protocol. Modified from Mazutis et al. 2013.

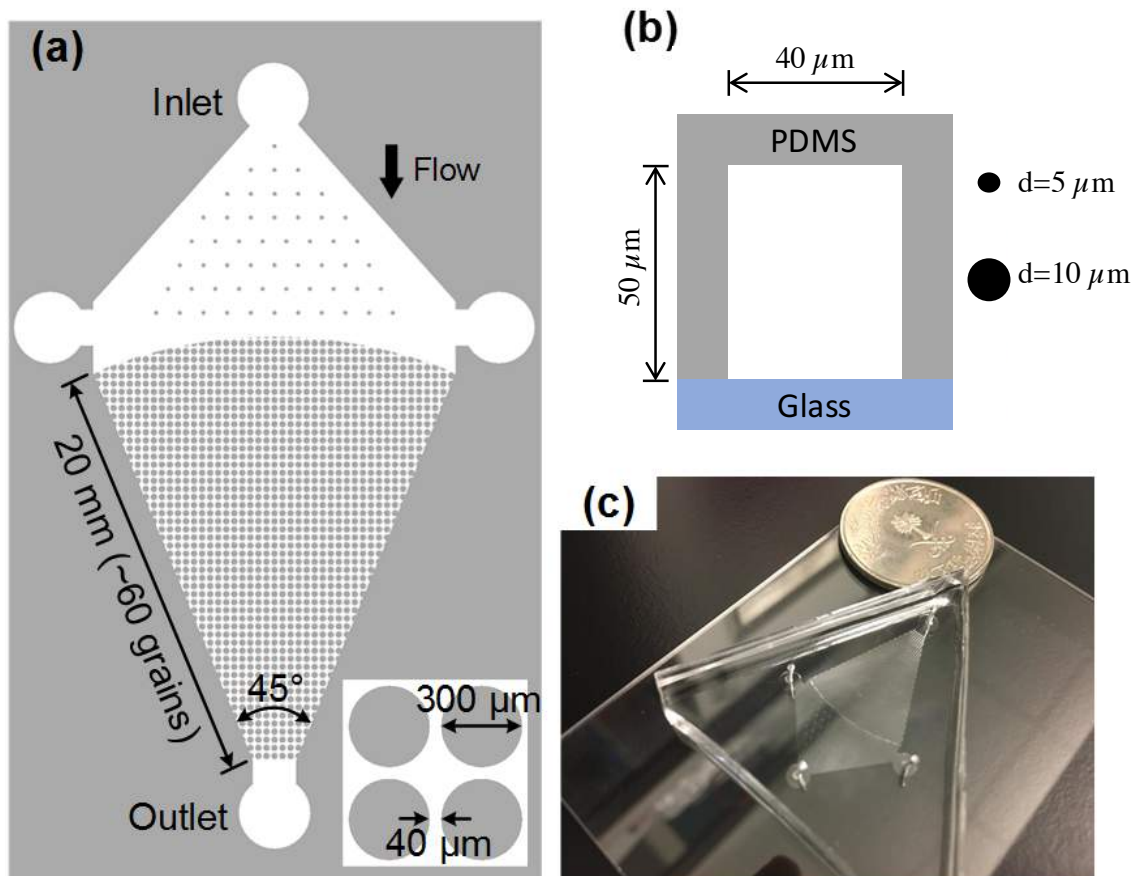


Figure 4.5. Microfluidic chips. (a) Design sketch. (b) Cross-section of a constriction. (c) Close up view of a chip after fabrication.

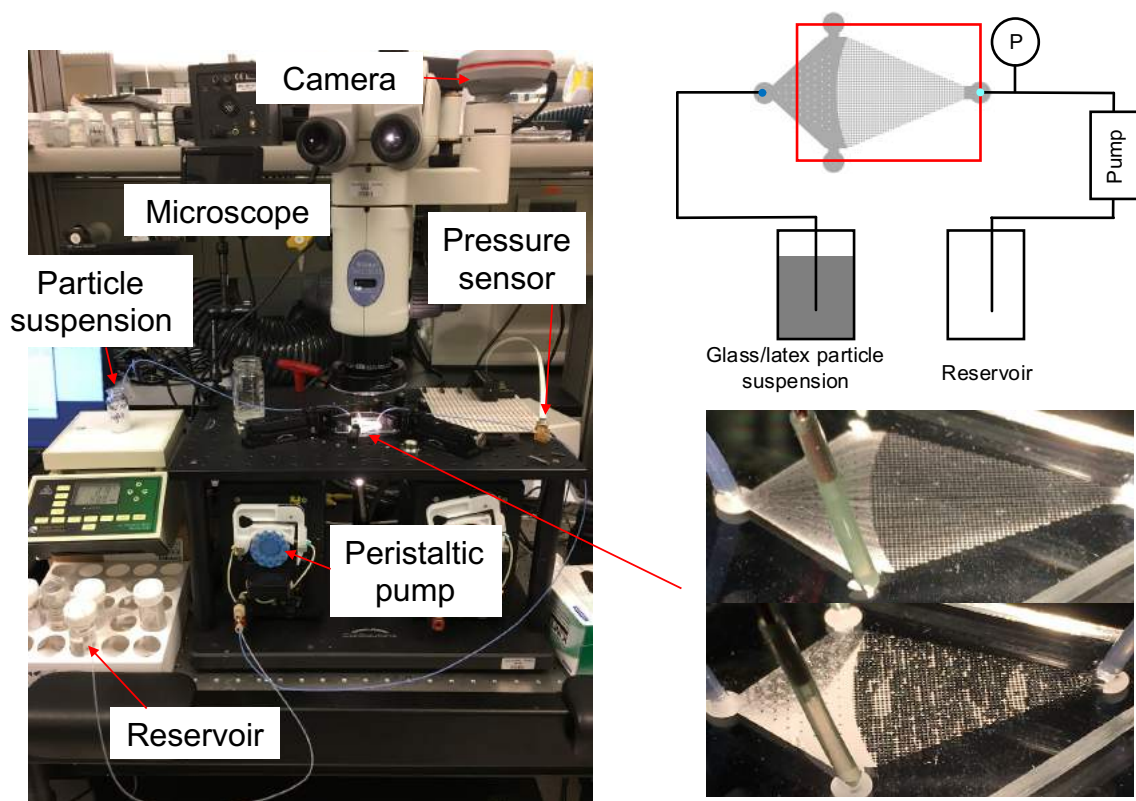


Figure 4.6. Experimental setup. (a) All components. (b) Schematic. (c) Close up view of a chip before and after testing.



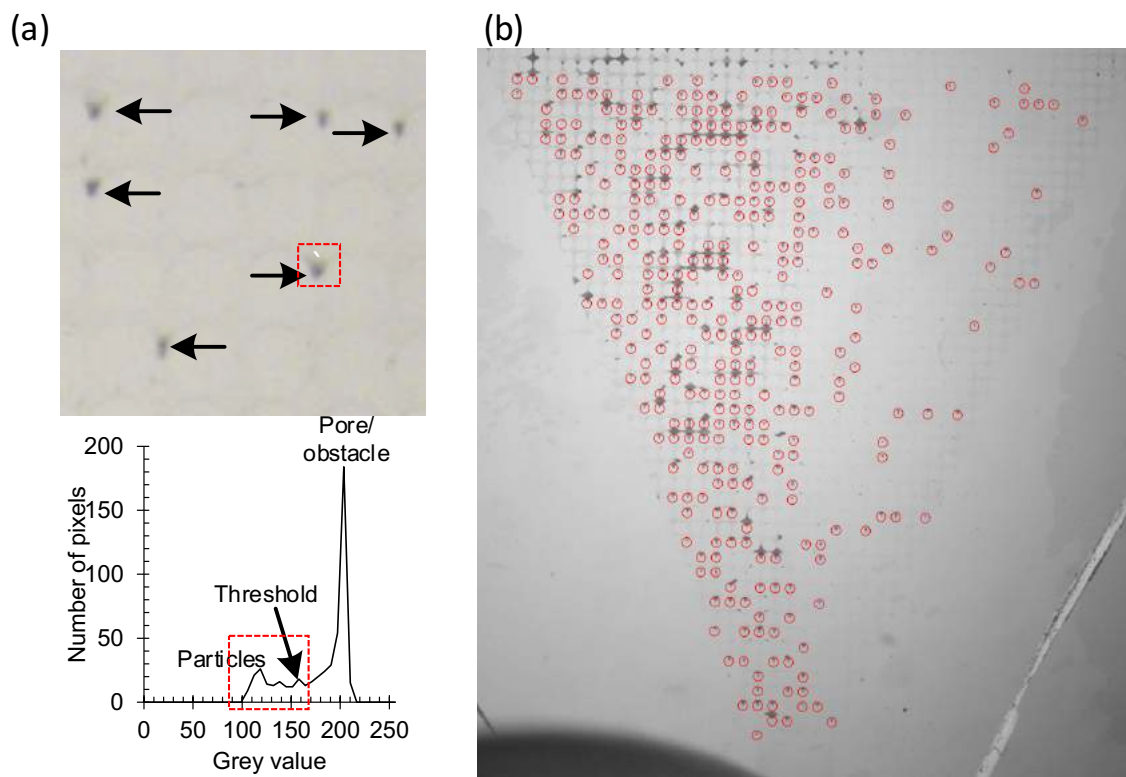


Figure 4.7. Image analyses. (a) Clogged pores and detection algorithm. (b) Distribution of clogged constrictions in chip.

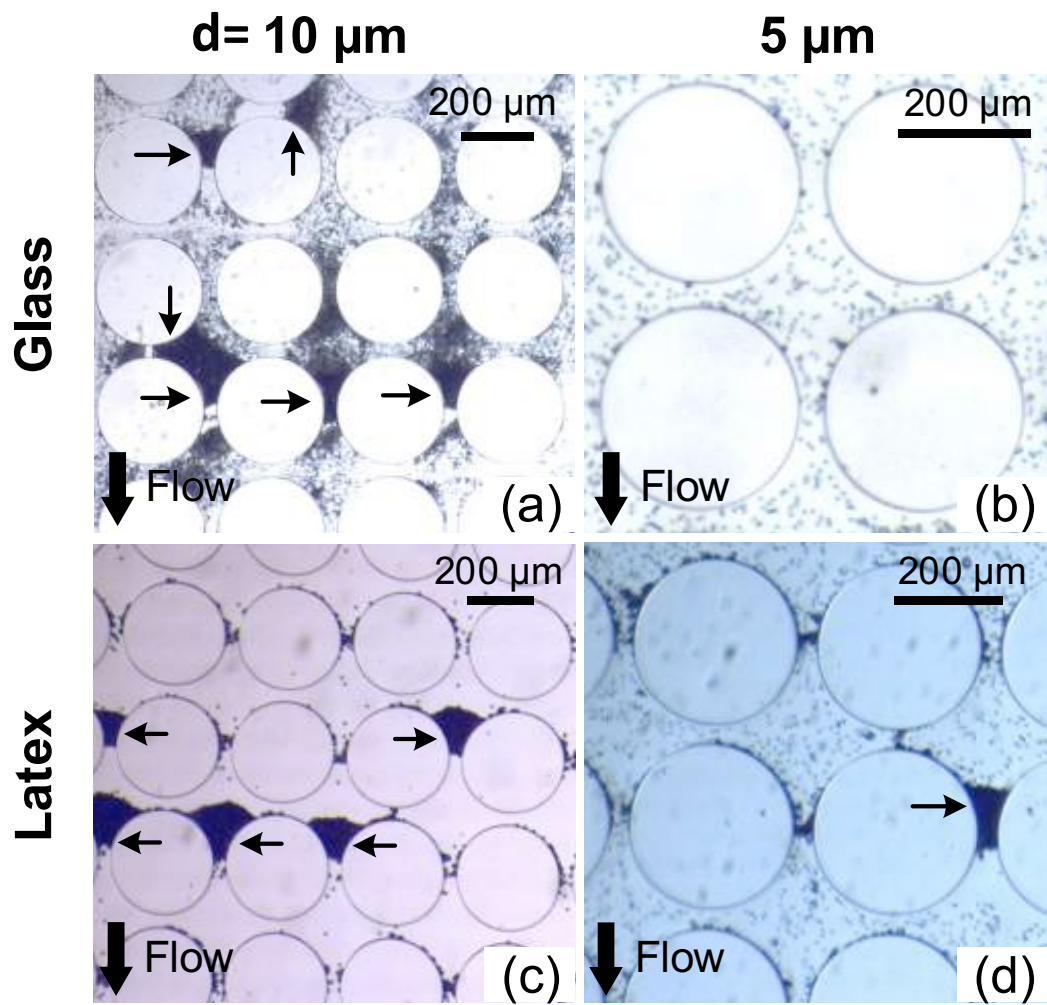


Figure 4.8. Typical pore-scale clogging patterns. (a) 10 μm glass particles. (b) 5 μm glass particles (no clogging occurs). (c) 10 μm latex particles. (d) 5 μm latex particles.

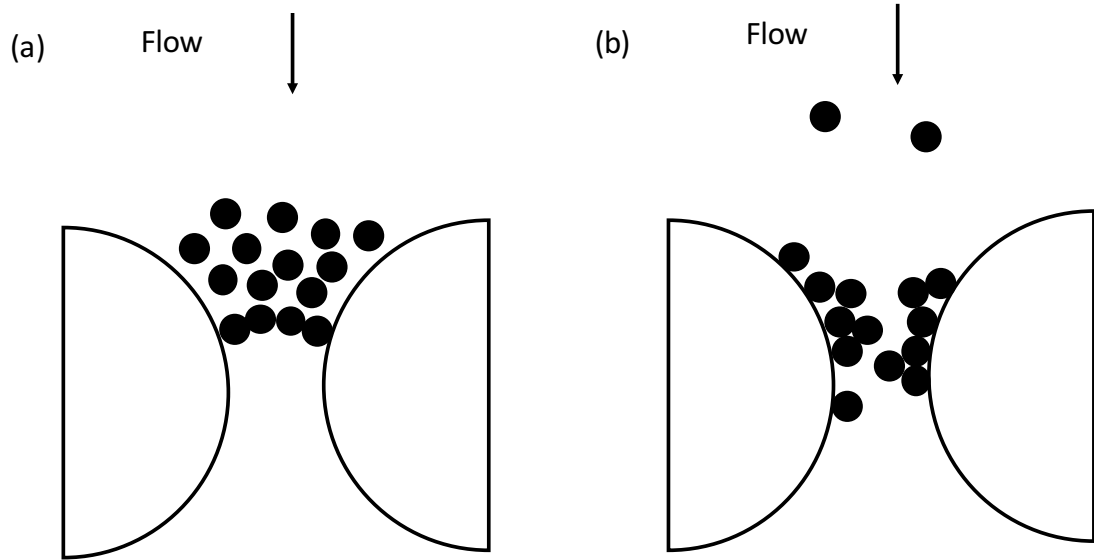


Figure 4.9. Two different mechanisms responsible for the clogging at pore constrictions. (a) Direct bridging: glass particle. (b) Deposition: latex particle.

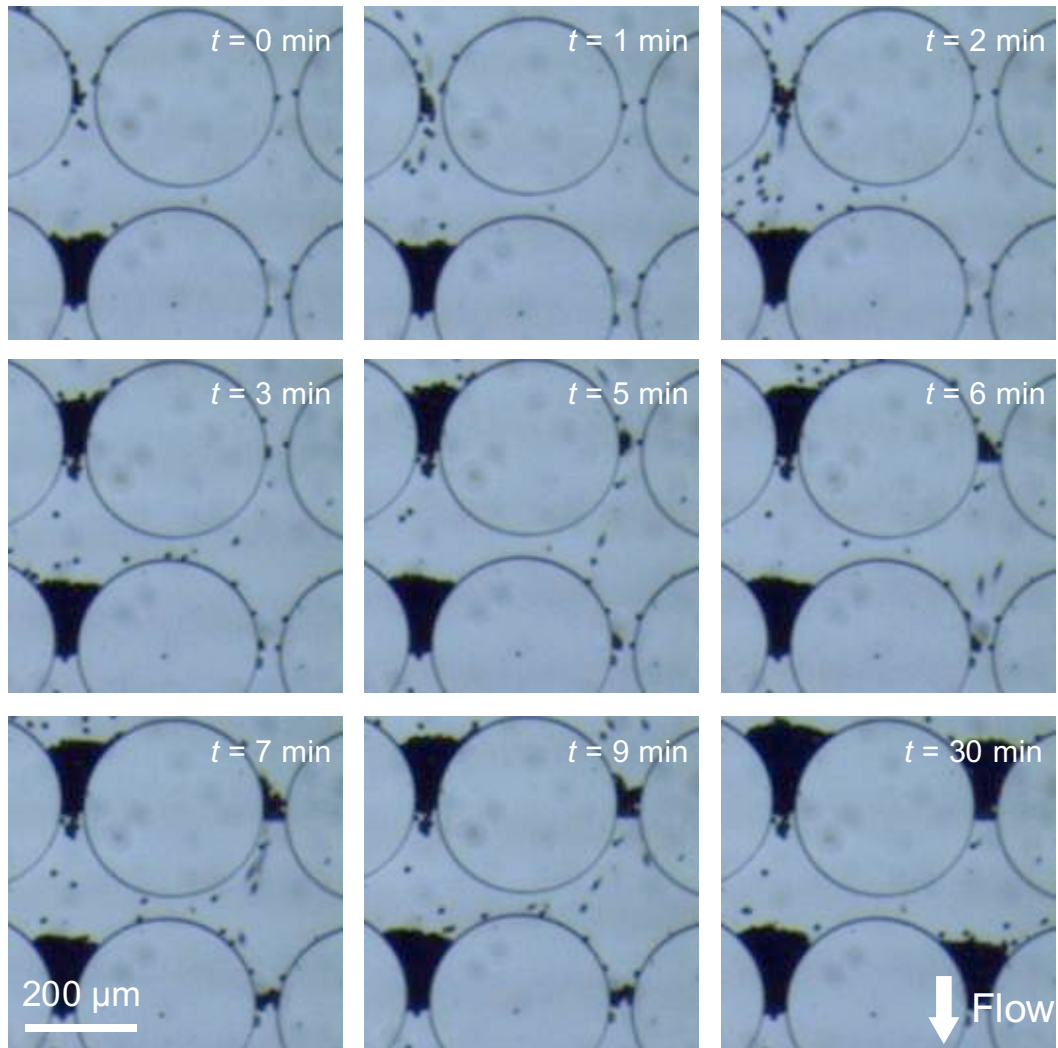


Figure 4.10. Evolution of particle capture and clogging at constrictions.  $10 \text{ } \mu\text{m}$  latex particles.

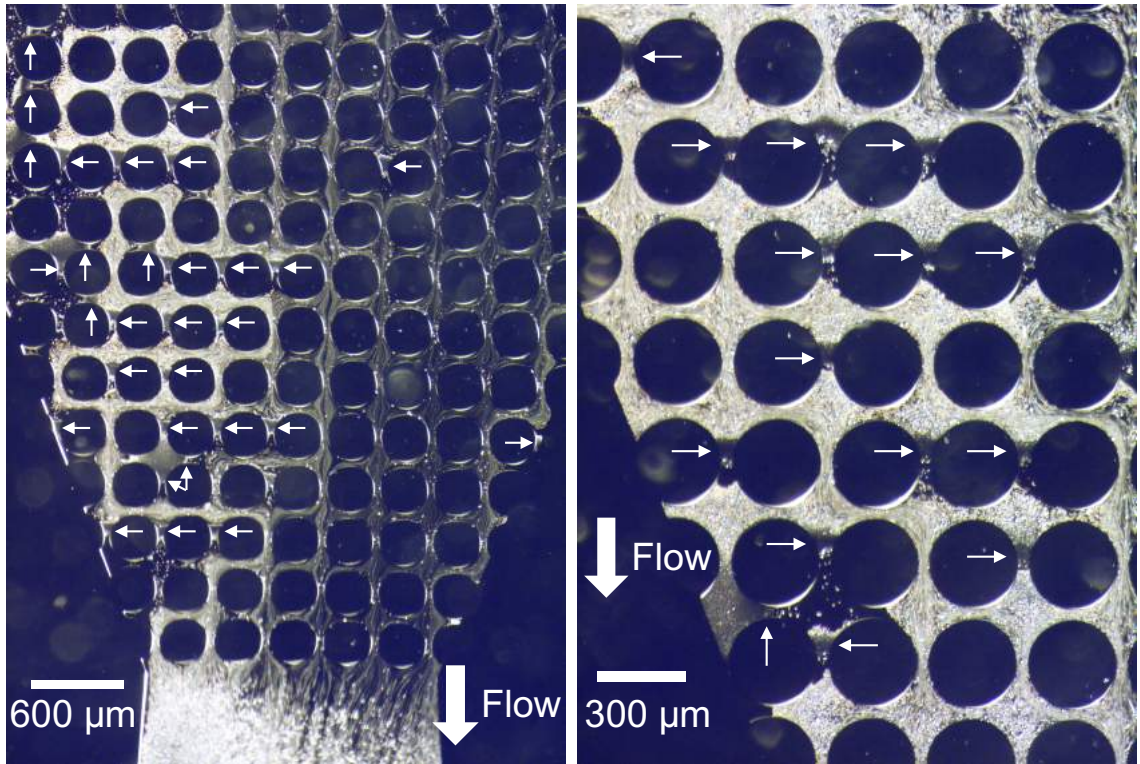


Figure 4.11. Influence of existing clogging on flow tortuosity and particle retardation. Note: arrows mark clogged pore throats.

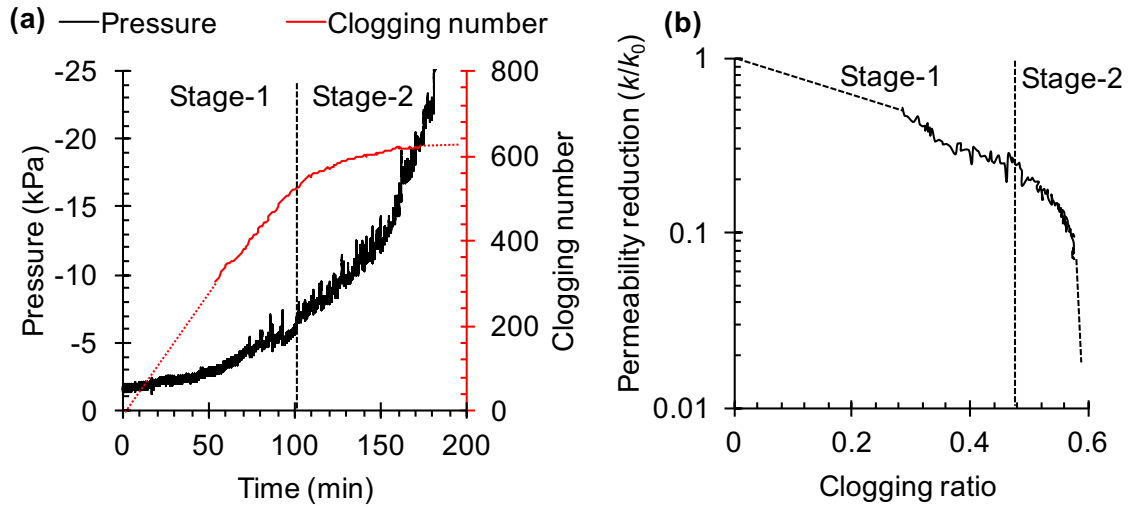


Figure 4.12. Clogging evolution. (a) Pressure and clogging numbers increase with time. (b) Permeability reduces with an increased clogging ratio.

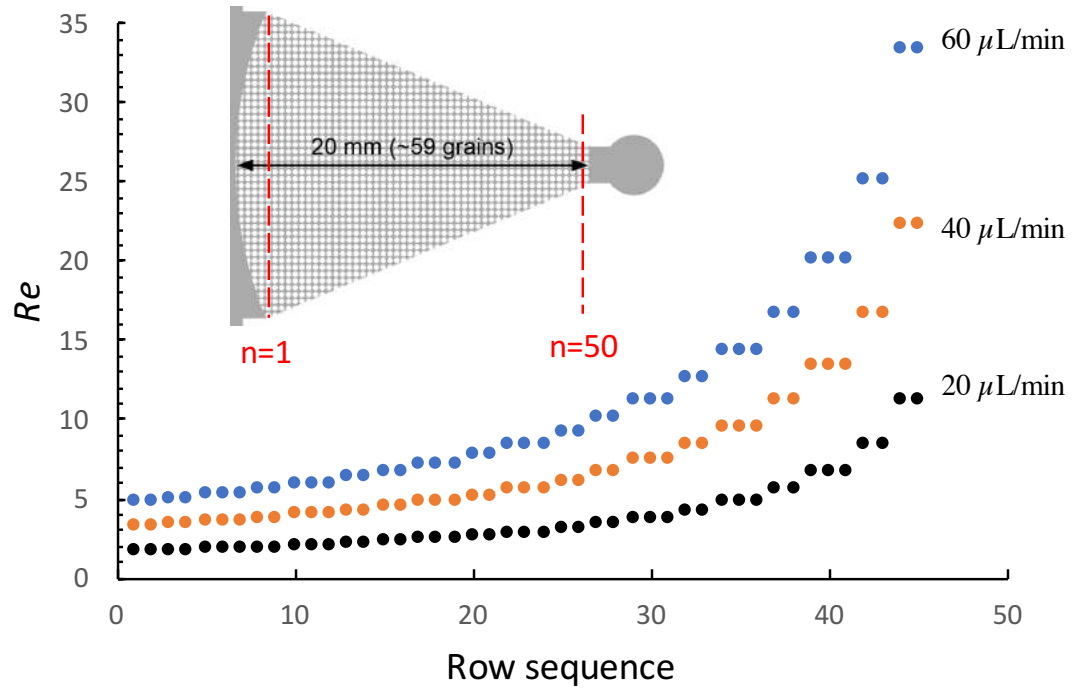


Figure 4.13. The distribution of the Reynolds number in the microfluidics chip. Flow rates: 20  $\mu\text{L}/\text{min}$ , 40  $\mu\text{L}/\text{min}$ , and 60  $\mu\text{L}/\text{min}$

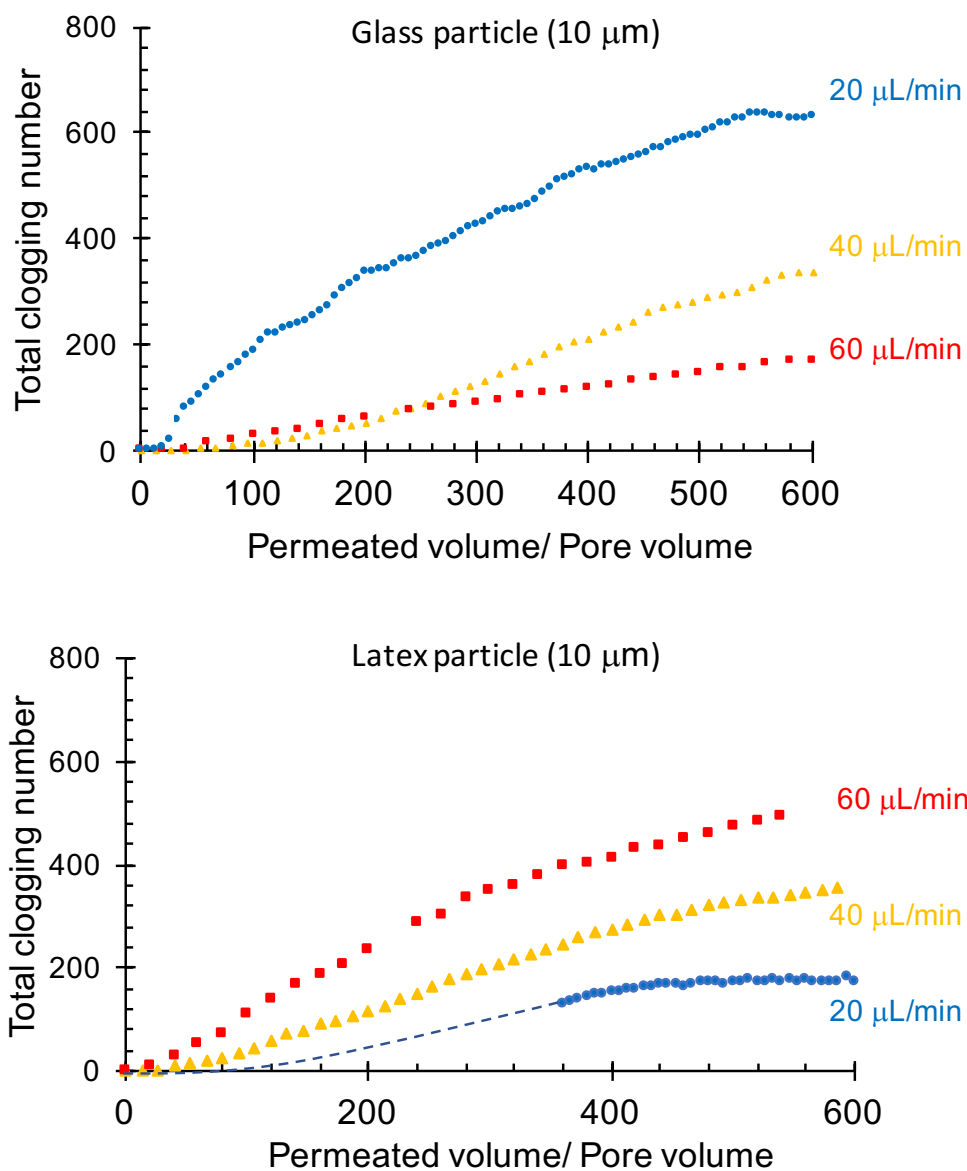


Figure 4.14. The effect of flow rate on the evolution of clogging. (a) 10  $\mu\text{m}$  glass particles. (b) 10  $\mu\text{m}$  latex particles.



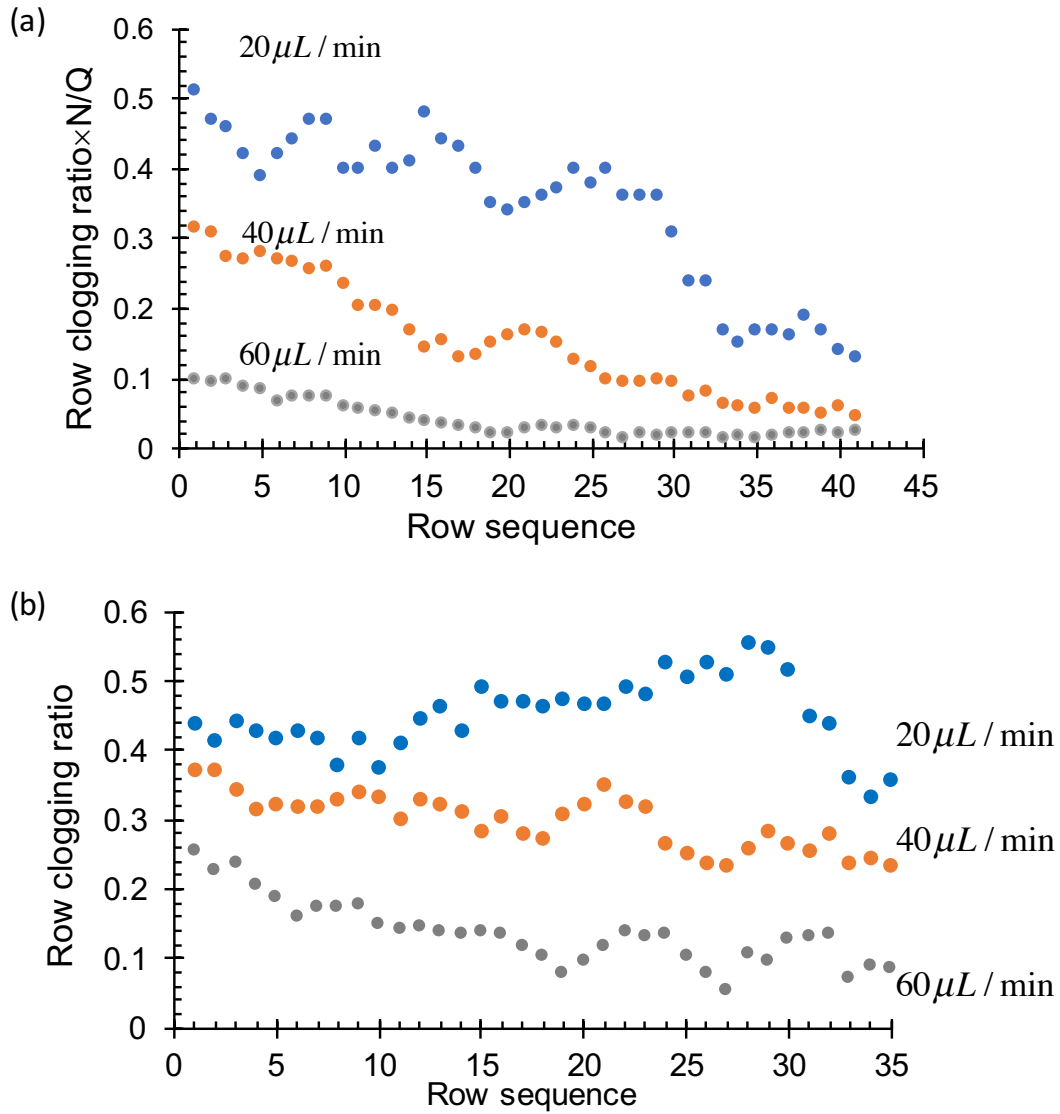


Figure 4.15. The influence of radial flow on the clogging of glass particles. (a) The distribution of row clogging ratios per unit pore volume suspension at 500 pore volumes. (b) The distribution of row clog ratios at 500 pore volumes. Flow rates: 20  $\mu\text{L}/\text{min}$ , 40  $\mu\text{L}/\text{min}$  and 60  $\mu\text{L}/\text{min}$



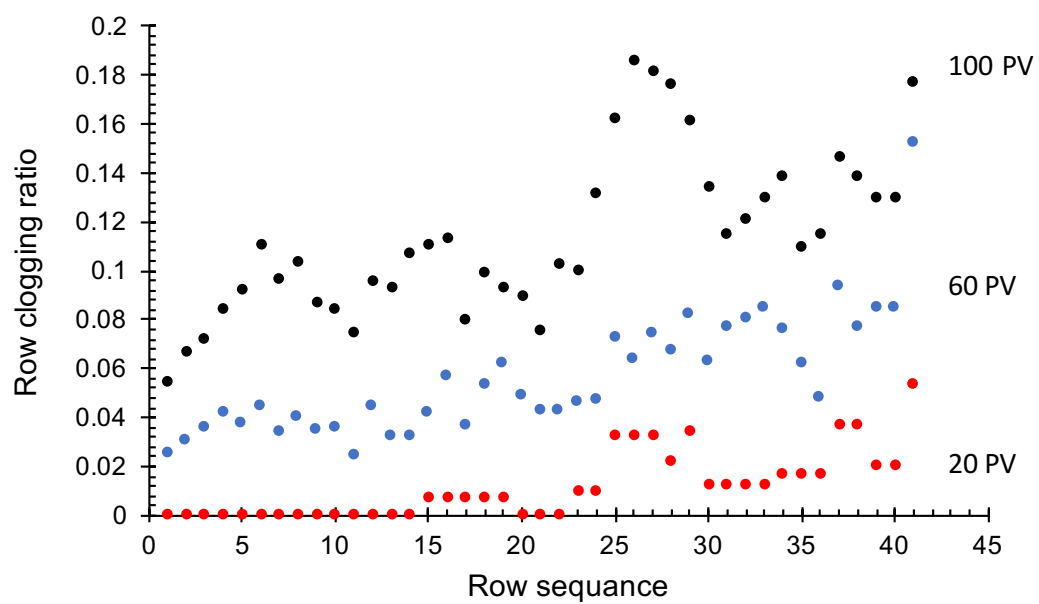


Figure 4.16. The evolution of the distribution of row clogging ratios for latex particles. Flow rates: 60  $\mu\text{L}/\text{min}$ . Note: PV=pore volumes.

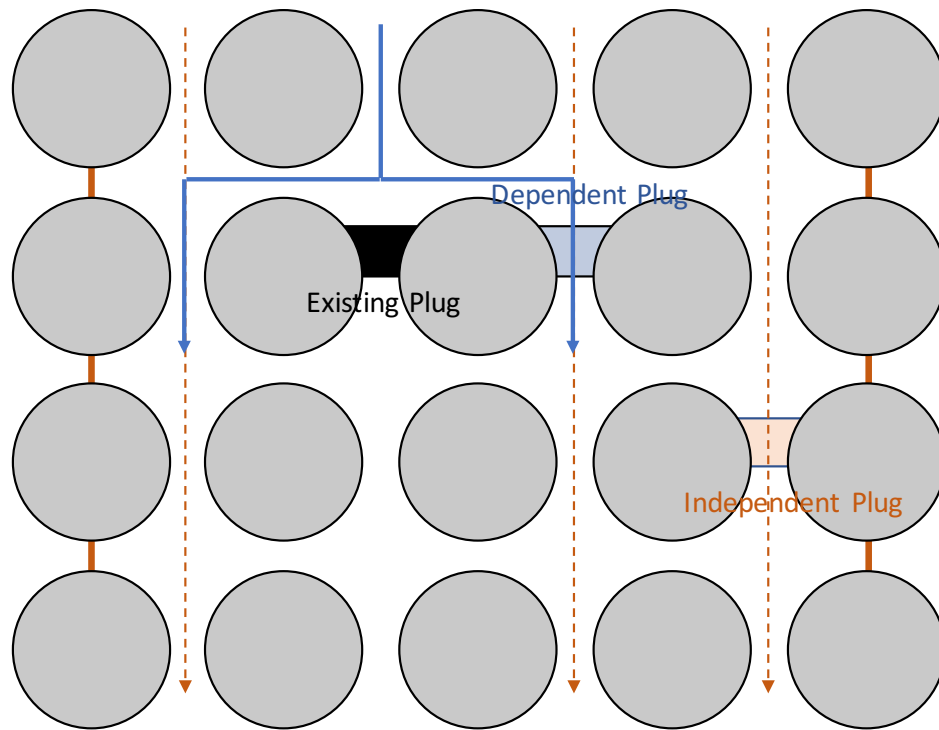


Figure 4.17. Schematic diagram of dependent and independent clogging.

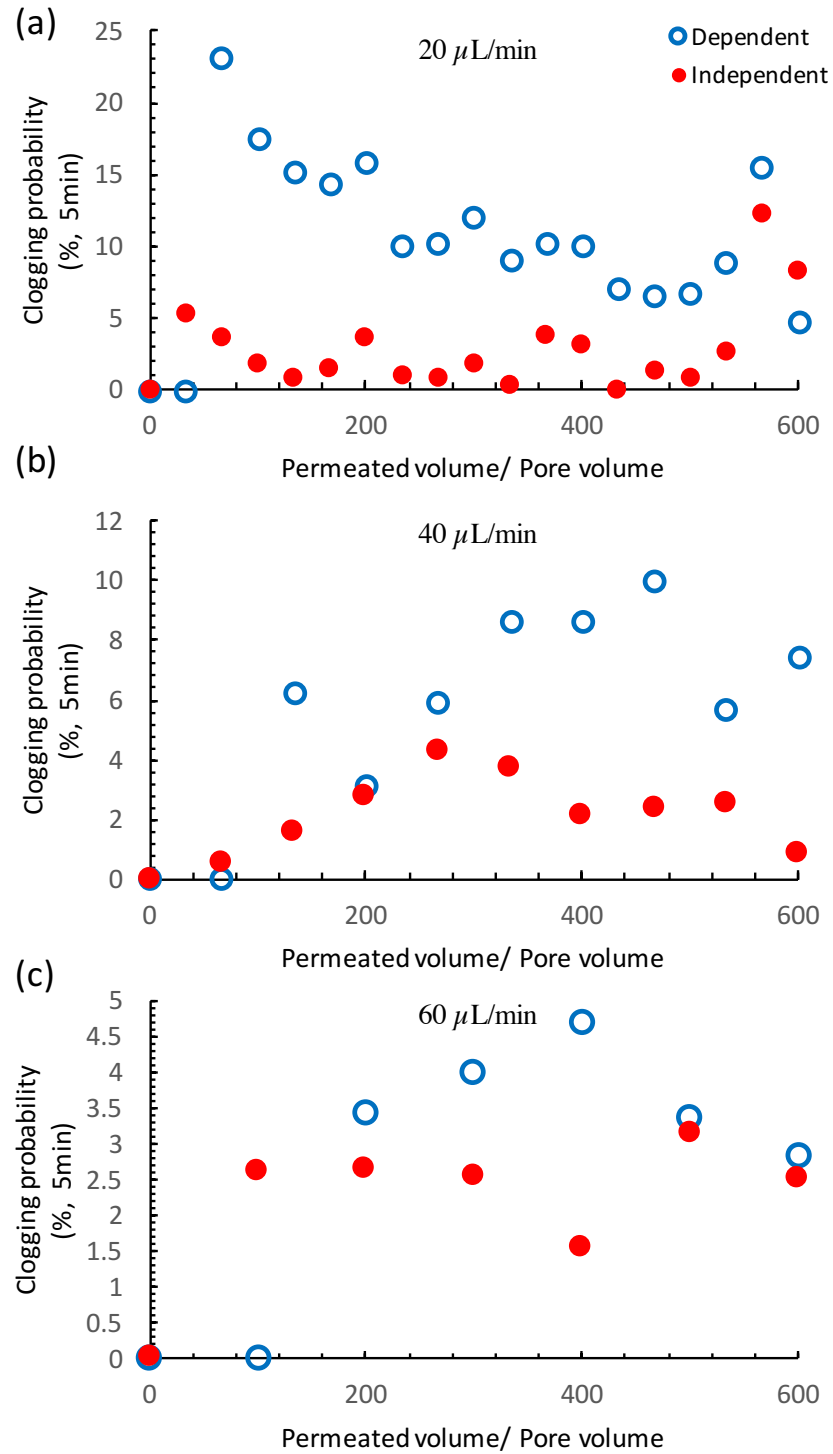


Figure 4.18. Dependent and independent clogging probability for 10  $\mu\text{m}$  glass particles. Flow rates: (a) 20  $\mu\text{L}/\text{min}$ , (b) 40  $\mu\text{L}/\text{min}$ , and (c) 60  $\mu\text{L}/\text{min}$ .

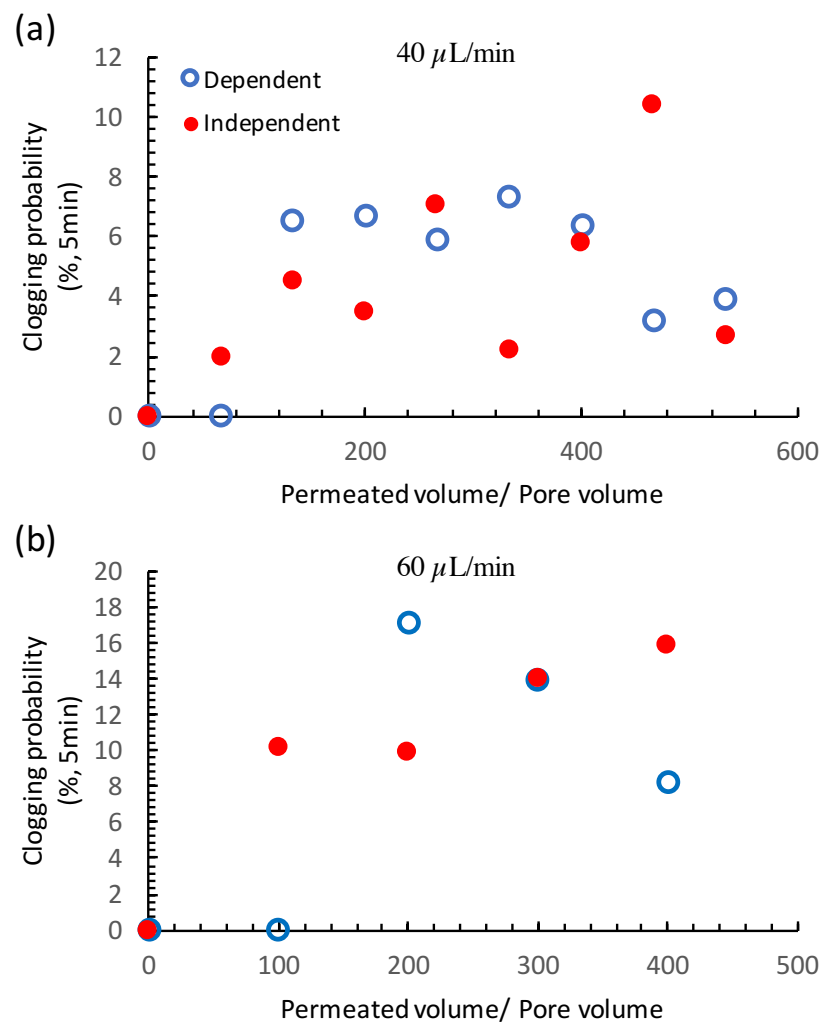


Figure 4.19. Dependent and independent clogging probability for 10  $\mu\text{m}$  latex particles. Flow rates: (a) 40  $\mu\text{L}/\text{min}$  and (b) 60  $\mu\text{L}/\text{min}$ .

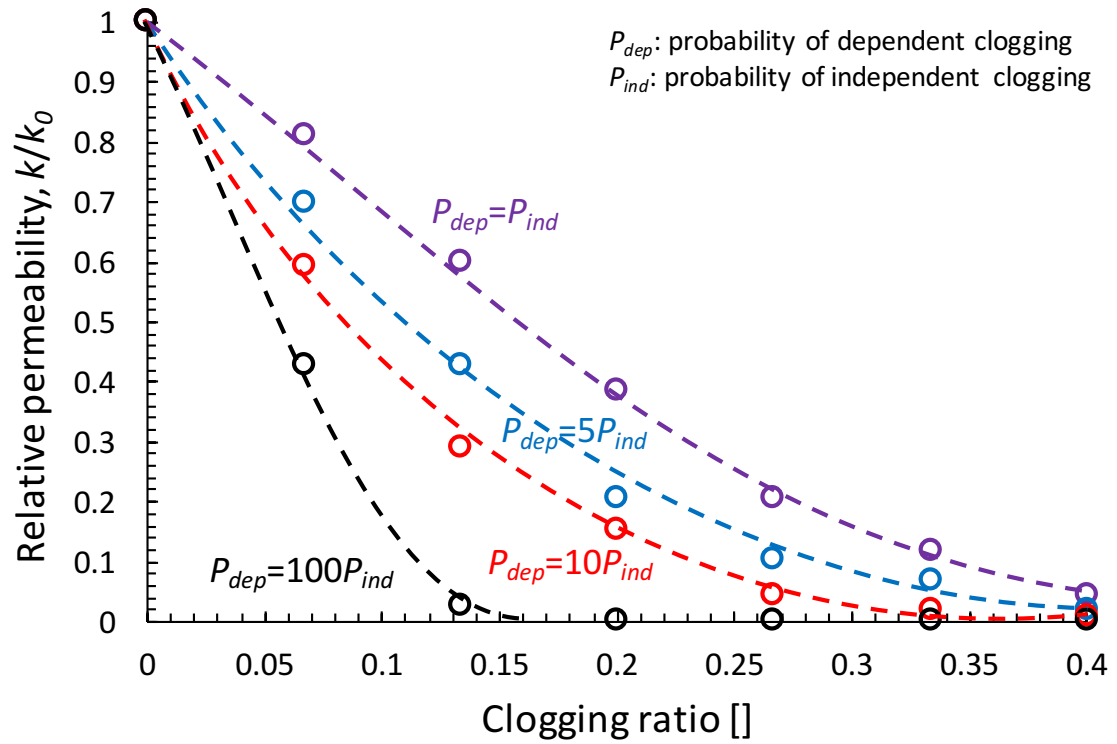


Figure 4.20. Permeability reduction with  $P_{dep}=P_{ind}$ ,  $5P_{ind}$ ,  $10P_{ind}$ , and  $100P_{ind}$ . Note:  $P_{dep}$  is the probability of dependent clogging and  $P_{ind}$  is the probability of independent clogging.

## **CHAPTER 5. PARTICLE FILTRATION: MUDCAKE GROWTH**

### **5.1 Introduction**

The drilling mud removes cuttings from the wellbore, reduces friction between the drill pipe or casing and the wellbore, cools and cleans the bit, coats the formation with a thin, low-permeability filter cake, maintains wellbore stability, and minimizes formation damage. Liquids filtrate into the formation, and solid particles remain behind and form the filter cake against the well wall.

Early research demonstrated that the cumulative flow-through volume is proportional to the square root of time when drilling mud is pressed against a filter paper under conditions of constant pressure and temperature (Larsen 1938). The filter cake evolves over time but remains inherently heterogeneous due to the large effective stress gradient that develops across the cake and the ensuing large gradient in porosity and permeability.

The study of mudcake formation and implications has involved experimental as well as analytical and numerical methods. Experimental studies use various techniques that include: dissection (Meeten 1993, Sherwood and Meeten 1997), X-ray tomography (Elkhatatny et al. 2012) and scanning electron microscopy (Hartmann et al. 1988). Cake formation models typically start with solid and liquid mass conservation equations and incorporate constitutive equations that relate void ratio, effective stress and permeability (Wakeman 1981, Sherwood et al. 1991, Stamatakis and Tien 1991, Chenevert and Dewan 2001, Johansson and Theliander 2007). Constitutive equations adopted in previous

analyses distinguish the “cake phase” from the “slurry phase” and result in “moving boundary” type solutions (Outmans 1963, Collins 1976, Stamatakis and Tien 1991).

This chapter advanced a comprehensive mudcake growth model for water-based mud based on robust constitutive equations, and used this model to evaluate the influences of time, pressure and environmental factors such as temperature and salinity on the filtration behavior of drilling muds. Subsequent analyses explored critical drilling and completion issues that include mud shearing and differential pressure sticking.

## 5.2 Model Development

Consider a mud-filled cylinder and a piston that pushes the mud in the cylinder against a pervious formation (Figure 5.1(a)). While liquids filtrate into the formation, solid particles remain behind against the interface. We can describe this physical process with the Eulerian or the Lagrangian system.

### 5.2.1 Eulerian system

The Eulerian coordinate is an external system. Solid and liquid flux travel across element boundaries in the consolidation process. Let's consider an infinitesimal element (Figure 5.1(b)), the mass conservation equation for solids is:

$$v_s(x) - v_s(x + dx) = \frac{\partial}{\partial t}[(1 - n)dx] \quad (5.1)$$

where  $n$  is the porosity, and  $v_s$  is the Darcy velocity of the solid phase. The continuity equation of solids is:

$$\frac{\partial}{\partial x}(v_s) + \frac{\partial}{\partial t}(1-n) = 0 \quad (5.2)$$

We can obtain the continuity equation of fluids with the same method.

$$\frac{\partial}{\partial x}(v_f) + \frac{\partial n}{\partial t} = 0 \quad (5.3)$$

Combine two continuity equations,

$$\frac{\partial}{\partial x}(v_s + v_f) = 0 \quad (5.4)$$

Assume Darcy's law is valid throughout this model.

$$n(\tilde{v}_f - \tilde{v}_s) = -\frac{k}{\mu_f} \frac{\partial u}{\partial x} \quad (5.5)$$

where  $\tilde{v}_f$  and  $\tilde{v}_s$  are true velocities of the solid and fluid phases, related with Darcy velocities by  $n\tilde{v}_f = v_f$ ,  $(1-n)\tilde{v}_s = v_s$

$$v_f - n(v_f + v_s) = -\frac{k}{\mu_f} \frac{1}{1+e} \frac{\partial u}{\partial x} \quad (5.6)$$

Differentiate both sides

$$\frac{\partial v_f}{\partial x} - (v_f + v_s) \frac{\partial n}{\partial x} = -\frac{\partial}{\partial x} \left[ \frac{k}{\mu_f} \frac{1}{1+e} \frac{\partial u}{\partial x} \right] \quad (5.7)$$

$$\frac{\partial n}{\partial t} + (v_f + v_s) \frac{\partial n}{\partial x} = \frac{\partial}{\partial x} \left[ \frac{k}{\mu_f} \frac{1}{1+e} \frac{\partial u}{\partial x} \right] \quad (5.8)$$



$v_s = 0$  at the formation interface. Since this is the only drainage boundary, the fluid velocity must be equal to the displacement rate of the piston,  $v_f = \frac{dS}{dt}$ .

$$v_f + v_s = \frac{dS}{dt} \quad (5.9)$$

Let's substitute Eq 5.9 into Eq 5.8:

$$\frac{\partial n}{\partial t} + \frac{dS}{dt} \frac{\partial n}{\partial x} = \frac{\partial}{\partial x} \left[ \frac{k}{\mu_f} \frac{1}{1+e} \frac{\partial u}{\partial x} \right] \quad (5.10)$$

### 5.2.2 Lagrangian system

Let's adopt a Lagrangian reference systems fixed in the solid to describe the physical process (see also Sherwood et al. 1991, Sherwood and Meeten 1997). The boundaries of the Lagrangian element move with the same velocity as the solid velocity during compression. Figure 5.1(c) shows an infinitesimal element between  $z$  and  $z+dz$ . The relationship between Eulerian coordinate and Lagrangian coordinate is:

$$z(x) = \int_0^x \frac{1}{1+e} dx \quad (5.11)$$

$$\frac{dz}{dx} = \frac{1}{1+e} \quad (5.12)$$

The fluid mass conservation relates the change in flux through the element to the change in the element void ratio  $e$  [Note: void ratio is the volume of voids normalized by the volume of solids and it is related to porosity  $n$  as  $n=e/(1+e)$ ]:

$$[v_f(z + dz) - v_f(z)]dt = -dz[e(t + dt) - e(t)] \quad (5.13)$$

so that

$$\frac{\partial e}{\partial t} = -\frac{\partial v_f}{\partial z} \quad (5.14)$$

Darcy's law relates the fluid velocity  $v_f$  [m/s] to the permeability of the porous medium  $k$  [m<sup>2</sup>], the viscosity of the liquid phase  $\mu$  [Pa·s] and the pressure gradient  $\partial u/\partial z$  [Pa/m].

$$v_f = -\frac{k}{\mu(1+e)} \frac{\partial u}{\partial z} \quad (5.15)$$

Let's substitute Darcy's law into the mass conservation equation to obtain the governing equation for the mud compressed against the pervious wall:

$$\frac{\partial e}{\partial t} = \frac{\partial}{\partial z} \left[ \frac{k}{\mu} \frac{1}{1+e} \frac{\partial u}{\partial z} \right] \quad (5.16)$$

Initially, the mud has a uniform void ratio  $e_0$ . The piston imposes a pressure  $u_0$ , therefore the filtration pressure is  $u_0 - u_\infty$ , where  $u_\infty$  is the constant pressure in the far field inside the formation. As the liquid invades the formation, the effective stress  $\sigma'$  in the mud increases next to the wall in response to changes in fluid pressure  $u$ ,

$$\frac{\partial \sigma'}{\partial z} = -\frac{\partial u}{\partial z} \quad (5.17)$$

Therefore, Equation 5.16 becomes:

$$\frac{\partial e}{\partial t} = -\frac{\partial}{\partial z} \left[ \frac{k}{\mu} \frac{1}{1+e} \frac{\partial \sigma'}{\partial z} \right] \quad (5.18)$$

The mud permeability decreases as the void ratio decreases during cake formation, and the permeability  $k=f(e)$  remains inside the derivative. We note that the 1D-formulation developed here presumes a cake thickness much smaller than the well radius.

### 5.2.3 Dimensionless analysis

The governing differential equation can be written in terms of non-dimensional variables. Table 1 summarizes the selected set of dimensionless ratios and their physical significance. The differential equation (Eq. 5.18) in terms of non-dimensional variables becomes:

$$\frac{\partial E}{\partial T} = G \frac{\partial}{\partial H} \left[ H(E) \frac{\partial E}{\partial H} \right] \quad (5.19)$$

Where

$$G = \frac{k_0}{e_0 L_o^2}$$

$$H(E) = \frac{K}{1+Ee_0} \frac{\partial U}{\partial E}$$

## 5.3 Clay Behavior- Constitutive Equations

The effective stress varies from  $\sigma'=0$  MPa in the slurry, to values that often exceed  $\sigma'>1$  MPa in the mudcake against the formation. Consequently, the void ratios fall from  $e>40$  to

$e < 0.5$ , and the permeability decreases over 5 orders of magnitude. Surprisingly, these dramatic changes take place within a few millimeters.

Furthermore, in situ conditions are characterized by high temperature and the risk of high salinity contamination. Therefore, we need adequate constitutive models for mud compaction and permeability as a function of effective stress, temperature, and salinity. Table 5.1 summarizes constitutive equations adopted in previous drilling mud studies. We seek robust, physics-inspired models with a limited number of physically meaningful parameters.

### 5.3.1 *Clay structure*

Electrical inter-particle forces determine particle aggregation in mineral suspensions. These forces depend on the mineral and fluid chemistry. The drilling industry prefers mono-ionic sodium montmorillonite, where  $\text{Na}^+$  cations populate the counter-ion cloud around particles. The fluid pH determines clay edge and surface charges, while the fluid ionic concentration controls the double layer thickness and the balance between attraction and repulsion forces. Consequently, the pore fluid pH and ionic concentration will determine the tendency to disperse or to aggregate into edge-to-face, edge-to-edge, or face-to-face aggregations (Van Olphen 1977, Santamarina et al. 2002). Other environmental factors such as temperature affect particle association and filtration properties.

The highest void ratio that a packing of platy particles can attain depends on the particle slenderness  $\alpha$ , defined as the length  $L_p$  divided by the thickness  $t_p$ . For example, the void ratio for a card-castle structure can be as high as  $e_{\max} = (\alpha - 1)/2$  (Sharma and Zongming 1991, Santamarina et al. 2001). The slenderness of montmorillonite particles

may reach  $\alpha=100$ , which corresponds to a void ratio  $e=50$ . This agrees with experimental studies using shear waves (Klein and Santamarina 2005) and rheological properties (Abend and Lagaly 2000, Santagata et al. 2008).

### 5.3.2 Compressibility

We adopted a wide stress-range compressibility model to avoid the artificially defined cake-slurry interface in the moving boundary problem (Peck and Terzaghi 1948, Chong and Santamarina 2016):

$$e = e_c - C_c \log \left( \frac{1 \text{ kPa}}{\sigma' + \sigma'_L} + \frac{1 \text{ kPa}}{\sigma'_H} \right)^{-1} \quad (5.20)$$

where asymptotic void ratios  $e \rightarrow e_L$  and  $e \rightarrow e_H$  define the threshold effective stresses  $\sigma'_L$  and  $\sigma'_H$ ,

$$\sigma'_H = 10^{(e_c - e_H)/C_c} \text{ kPa} \text{ when } \sigma' \rightarrow \infty \quad (5.21)$$

$$\sigma'_L = \frac{\sigma'_H}{10^{(e_L - e_H)/C_c} - 1} \text{ when } \sigma' \rightarrow 0 \quad (5.22)$$

In mud analyses,  $e_L$  is the initial void ratio  $e_0$  of the slurry as mixed,  $e_L = e_0 \leq e_{max}$ . Figure 5.2(a) shows experimental data and model prediction for void ratio versus effective stress  $e-\sigma'$ . In the absence of data at very low effective stress, we note that the void ratio at the liquid limit  $e_{LL}$  is a good estimate of the void ratio at  $\sigma' = 1 \text{ kPa}$ ,  $e_{1 \text{ kPa}} \approx e_{LL} = G_s \bullet LL / 100$  (Chong and Santamarina 2016).

### 5.3.3 Fluid flow: permeability versus void ratio

Permeability decreases as the pore size decreases when the slurry compacts to form the cake. This study adopts a power equation to relate permeability  $k$  to the void ratio  $e$  (Kozeny 1927, Carman 1937, Taylor 1948, Chapuis 2003, Ren and Santamarina 2017):

$$k = k_0 \left( \frac{e}{e_0} \right)^\beta \quad (5.23)$$

where  $k_0$  is the permeability at the reference void ratio  $e_0$  and the  $\beta$ -exponent captures the sensitivity of permeability to changes in the void ratio. Figure 5.2(b) shows that this constitutive equation adequately matches experimental data for bentonite. While data are missing at very low effective stress, we highlight that the void ratio at high effective stress dominates the fluid flux across the filter cake.

The proposed constitutive models for compressibility and permeability capture the gradual mud response with effective stress, avoid the non-natural assumptions in moving boundary solutions, and correctly anticipate observed experimental trends (see comparison in supplemental material).

#### 5.3.4 *Temperature: clay rheology and fluid viscosity*

Temperature alters the rheological characteristics and the compaction behavior of clay pastes through a combination of competing effects: increased platelet Brownian motion and hindered bond formation, increased Debye-Huckel length and inter-particle repulsion, faster aggregation towards minimum potential energy configurations, and decreased fluid viscosity.

Experimental evidence shows that the yield stress of bentonite suspensions is weakly dependent on temperature below 60°C and rapidly rises at higher temperature due to the effect of dispersion and increased effective mineral surface (Annis 1967, Alderman et al. 1988). Conversely, a well-dispersed bentonite suspension displays a decrease in the high-shear viscosity as temperature increases (Annis 1967, Alderman et al. 1988).

Figure 5.3 shows the shear plane around dispersed and face-to-face aggregated platelets. Consider  $n_0$  platelets of individual thickness  $t_p$  across a representative length scale  $L_0$ . When platelets group into  $n$  aggregates, the free space  $L_{free}$  for fluid shearing depends on the degree of dispersion  $\beta=n/n_0$  and the thickness to the shear plane  $t_{shear}$ :

$$L_{free} = L_0 - n_0 t_p - 2n t_{shear} = L_0 - n_0 (t_p + 2\beta t_{shear}) \quad (5.24)$$

Clearly, the fluid free space decreases and the shear resistance  $\tau=\mu v/L_{free}$  increases with increased dispersion  $\beta$ .

### 5.3.5 Fluid chemistry: pH and ionic concentration

Repulsion is shielded, van der Waals attraction prevails and platelets aggregate face-to-face at high ionic concentration, typically above seawater concentration  $\sim 0.5\text{mol/L}$  (see fabric maps in Santamarina et al. 2001; Palomino et al. 2005). The aggregation of platelets at high ionic concentrations leads to more compacted fabrics, a pronounced decrease in the liquid limit (Figure 5.4(a)) and lower compressibility  $C_C$  (Figure 5.4(b)).

Calcium ions replace sodium ions in counter ion clouds, shrink double layers and prompt aggregation. Therefore, mud contamination with calcium ions from gypsum,

anhydrite, lime or cement decreases the mud viscosity, increases fluid loss and results in more compact and less compressible cakes (Figure 5.5).

## **5.4 Cake Formation- Model Prediction**

The governing differential equation for cake formation (Eq. 5.18), constitutive equations (Eq. 5.20, 5.23), and mud behavioral trends addressed above (Figures 5.2 to 5.5) come together in this section, as we explore the mud response during drilling.

### *5.4.1 Filtration pressure and filtration time*

Let's consider a mud filled borehole. Figure 5.6 presents the void ratio profiles under a constant filtration pressure of 2MPa after 50s, 200s, 800s and 3200s (constitutive parameters listed in Table 2). The cake thickness increases with time. The non-linear  $e$ - $x$  trends reflect the coupling between the non-linear compressibility and permeability models.

Figure 5.7 provides void ratio contours along a wellbore after 2.8hr (constant filtration time at all depths). The minimum void ratio attained when the cake rests against the formation ( $x=0$ ) depends on the filtration pressure. Contour lines for large void ratios  $e>10$  away from the wall are not sensitive to the filtration pressure due to the high compaction next to the formation and the associated low permeability.



#### 5.4.2 Depth

The filtration time varies with depth during the drilling process. Let's consider a drilling stage from 400m to 600m with a rate of penetration  $ROP=20\text{m/hr}$  (Figure 5.8(a)). The filtration pressure is 0.8MPa at 400m and 1.2MPa at 600m with a mud weight= $1200\text{kg/m}^3$ . Drilling alone takes 10 hours so that the filtration time is 10 hours at depth 400m and 0 hour at depth 600m immediately-post drilling (still-time=0hr). Let's assume a void ratio  $e=10$  as a mud cake thickness criterion. With zero still-time, the corresponding mud cake thickness is 5.8mm at depth 400m and 0mm at depth 600m. After 24hr of still-time, the filtration time is 34hr at 400m, 24hr at 600m, and the corresponding cake thickness has increased to 10.8mm and 9.1mm respectively (Figure 5.8(b)). The mud cake thickness becomes more uniform as the still time increases.

#### 5.4.3 Viscosity of the continuous phase

The viscosity of water decreases with temperature, but it can be augmented by more than two orders of magnitude with the addition of viscosifiers. Let's assume that the change in the viscosity of water does not alter the absolute permeability and compressibility of the bentonite skeleton.

Results in Figure 5.9 (a) and (b) demonstrate that an increase in the liquid viscosity effectively reduces the fluid loss and leads to a thinner and tighter filter cake. In particular, simulation results show that both fluid loss and cake thickness double when the water viscosity decreases from 1cP ( $\sim 20^\circ\text{C}$ ) to 0.3cP ( $\sim 90^\circ\text{C}$ ), in good agreement with previous experimental results (Arthur and Peden 1988). Clearly, filtration properties must be determined at in-situ temperature conditions.

#### 5.4.4 Permeability

The influence of the permeability on filtration is explored in Figure 5.10 for three different values of the reference permeability  $k_0$  that could result from ionic contamination ( $k_0=1\times 10^{-5}$  mD,  $5\times 10^{-5}$  mD and  $1\times 10^{-4}$  mD. Note: all other constitutive parameters in Table 2 remain the same). Results indicate that more permeable muds form thicker filter cakes and cause more severe fluid loss during filtration. This analysis supports previous experimental results and field observations related to severe fluid losses in the presence of  $\text{Ca}^{2+}$  or high ionic concentration contamination.

### 5.5 Implications

#### 5.5.1 Cementation: mud replacement and cake removal

Well integrity relies on successful cementing. Inadequate filter cake removal leaves behind a layer of residual cake which may become a potential pathway for gas flow along the annulus (Bonett and Pafitis 1996). The mudcake is sheared off until the shear stress imposed by the invading cement exceeds the shear strength of the mudcake. The imposed shear stress depends on the displacement velocity in the annulus between the casing and the well wall, and the viscosity of the cement.

On the other hand, the shear strength of the bentonite depends on effective stress in the cake and thixotropic hardening in the slurry. The yield stress of bentonite suspensions is a function of the time  $t$  and the void ratio  $e$  of bentonite:

$$\tau_y = A \left( \frac{t}{hr} \right)^B \text{Pa} \quad (5.25)$$

where  $A$  is the yield stress  $\tau_y$  when  $t=1$  hr, and  $B$  is the sensitivity of  $\tau_y$  to time. Experimental results in Figure 5.11 show that both  $A$  and  $B$  parameters are a function of the void ratio  $e$ :

$$A = 0.42 \exp \left( \frac{156}{2.6 + e} \right)$$

$$B = 0.37 - \frac{6.2}{2.6 + e}$$

The effective stress dependent shear strength  $\tau_y$  in the cake is estimated from the effective stress  $\sigma'$  following a standard Cam Clay formulation (Schofield and Wroth 1968):

$$\tau_y = 0.2\sigma' \quad (5.26)$$

We combined these two models to anticipate the shear strength profile of the slurry-mudcake system. Figure 5.12 shows the yield stress and shear strength profiles of a filter cake formed under the filtration pressure=2MPa after 0.1hr and 2.8hr. Results show the combined effect of effective stress and thixotropy: thixotropy dominates the yield stress of muds with high void ratios  $e>20$ .

Let's assume a  $OD=200$ mm casing inside a  $ID=280$ mm well so that the annulus is 40mm thick. The black lines in Figure 5.13 are the shear stress profiles imposed by the cement slurry driven by an effective pressure gradient of 3kPa/m and 12kPa/m along the well. The intersection point between the yield stress and the shear stress provides a conservative estimate of the residual cake thickness; in this case 11mm for a pressure gradient of 3kPa/m and 8mm for a pressure gradient of 12kPa/m. The high pressure

gradient required to remove the compacted mudcake is not attainable under normal flow conditions. Therefore, the shear stress imposed by the cement slurry is not sufficient for effective mudcake removal.

### 5.5.2 Differential pressure sticking

“Stuck pipe” events have been one of the drilling industry’s major challenges due to lost time and associated costs (Outmans 1958). In fact, stuck pipes account for about 25% of the non-productive time. A third of the stuck pipes are due to differential pressure sticking (Muqeem et al. 2012).

Mudcake formation has a strong influence on differential sticking incidents. Let’s use the cake growth model developed above to determine the force exerted on the tube surface due to unbalanced fluid pressure against the tube. In a polar coordinate system centered with the well ( $r, \theta$ ), the contour of a centered circle is  $r=R$  and the contour of an eccentric circle with an offset  $c$  satisfies  $r^2+c^2-2r\cdot c\cdot\cos \theta=R^2$  (Figure 5.14(a)-inset). The total force  $T$  generated by the fluid pressure is the integral of the fluid pressure  $u$  against the casing perimeter:

$$T = \int_0^{2\pi} u(r, \beta) R \cos(\beta) d\beta \quad (5.27)$$

Consider an  $ID=300\text{mm}$  borehole filled with mud under a  $1\text{MPa}$  filtration pressure. The  $OD=200\text{mm}$  pipe is offset  $c=49\text{mm}$  towards a side. Let’s assume that the presence of the pipe does not influence the void ratio and pore pressures profiles. Figure 5.14(a) shows the pore pressure against the well as a function of filtration time. There is a significant fluid

pressure drop at  $\beta=180^\circ$ , where the pipe is closest to the well wall. The total force  $T$  acting on the pipe increases sub-linearly with time as the mudcake grows  $T=1.05 \cdot (t/\text{hr})^{3/4}$  kN/m (Figure 5.14(b)). This trend resembles earlier experimental studies (Annis and Monaghan 1962, Reid et al. 1996, Sherwood 1998). Indeed, minimal time is recommended to reduce stuck pipe complications (Dupriest et al. 2011).

## 5.6 Conclusions

This study advanced a comprehensive mudcake growth model for water-based mud implemented with robust, physically-informed constitutive equations. In particular, we adopted wide stress-range constitutive models to avoid numerical discontinuities, and selected compatible model parameters for constitutive equations.

The mud cake thickness is more sensitive to time than to filtration pressure. Therefore, time controls the non-uniform distribution of mudcake thickness during drilling. Environmental factors such as temperature, pH, ionic concentration and cation contamination have a significant influence on cake formation. Long filtration time, high permeability, and low viscosity exacerbate fluid loss and increase the cake thickness.

Mud replacement is critical to the quality of the cementing job and the integrity of wellbores. The analysis of residual cake thickness takes into account the effective stress dependent mudcake formation and the time-dependent mud thixotropy. Thixotropy dominates the mud yield stress at high void ratios, e.g.  $e>20$ .

Stuck pipe by differential pressure sticking is responsible for costly non-productive time. The offsetting force increases sub-linearly as a power function of the still-time.

Table 5.1. Summary of constitutive equations in compressible cake models. Compressibility and Permeability

<b>Compressibility</b>	Power law	$\frac{(1 - n)}{(1 - n_0)} = \left(1 + \frac{\sigma'}{\sigma_0}\right)^\alpha$	Tiller and Leu 1980, Stamatakis and Tien 1991, Sørensen et al. 1996, Theliander and Fathi-Najafi 1996, Tien and Bai 2003, Johansson and Theliander 2007
		$\frac{n}{n_0} = \left(\frac{\sigma'}{\sigma_0}\right)^{-\alpha}$	Outmans 1963, Holdich 1993, Chenevert and Dewan 2001, Johansson and Theliander 2007
		$\frac{1 - n_{avg}}{1 - n_{avg0}} = \left(\frac{\sigma}{\sigma_0}\right)^{-\alpha}$	Tiller and Cooper 1962
		$e = e_0 + \left(\frac{\sigma_1}{\sigma' + \sigma_2}\right)^\alpha$	Sherwood and Meeten 1997
		$e = e_0 + \left(\frac{\sigma_1}{\sigma'}\right)^\alpha$	Carrier and Beckman 1984
	Inverse function	$n = n_0 + \frac{\sigma_1}{\sigma' + \sigma_2}$	Johansson and Theliander 2007
	Logarithm	$e = \alpha \log\left(\frac{-\sigma'}{\sigma_0}\right) + \beta$	Smiles 1970

	Modified semi-logarithmic model	$e = e_c - C_c \log \left( \frac{1kPa}{\sigma' + \sigma'_L} + \frac{1kPa}{\sigma'_H} \right)$	Chong and Santamarina 2016
<b>Permeability</b>	Power law	$k = k_0 \left( \frac{\sigma'}{\sigma_0} \right)^{-\beta}$	Tiller and Cooper 1962, Outmans 1963, Holdich 1993, Chenevert and Dewan 2001
		$k = k_0 \left( 1 + \frac{\sigma'}{\sigma_0} \right)^{-\beta}$	Tiller and Leu 1980, Stamatakis and Tien 1991, Sørensen et al. 1996, Theliander and Fathi-Najafi 1996, Tien and Bai 2003, Johansson and Theliander 2007
		$k = k_0 \left( \frac{e}{e_0} \right)^{\beta}$	Ren and Santamarina 2017
	Polynomial	$k = k_0 e^3 (1 + e)^{-2}$	Smiles 1970



Table 5.2. Model parameters

<b>Permeability</b> $k = k_0 \left( \frac{e}{e_0} \right)^b$	$k_0$	$5.6 \times 10^{-5} \text{ mD}$
	$e_0$	1
	$b$	3
<b>Compressibility</b> $e = e_c - C_c \log \left( \frac{1 \text{ kPa}}{\sigma'_L + \sigma'_L} + \frac{1 \text{ kPa}}{\sigma'_H} \right)$ $\sigma'_H = 10^{(e_c - e_H)/C_c} \text{ kPa}$ $\sigma'_L = \frac{\sigma'_H}{10^{(e_L - e_H)/C_c} - 1}$	$e_c$	23.5
	$e_L$	36
	$e_H$	0.6
	$C_c$	9.5

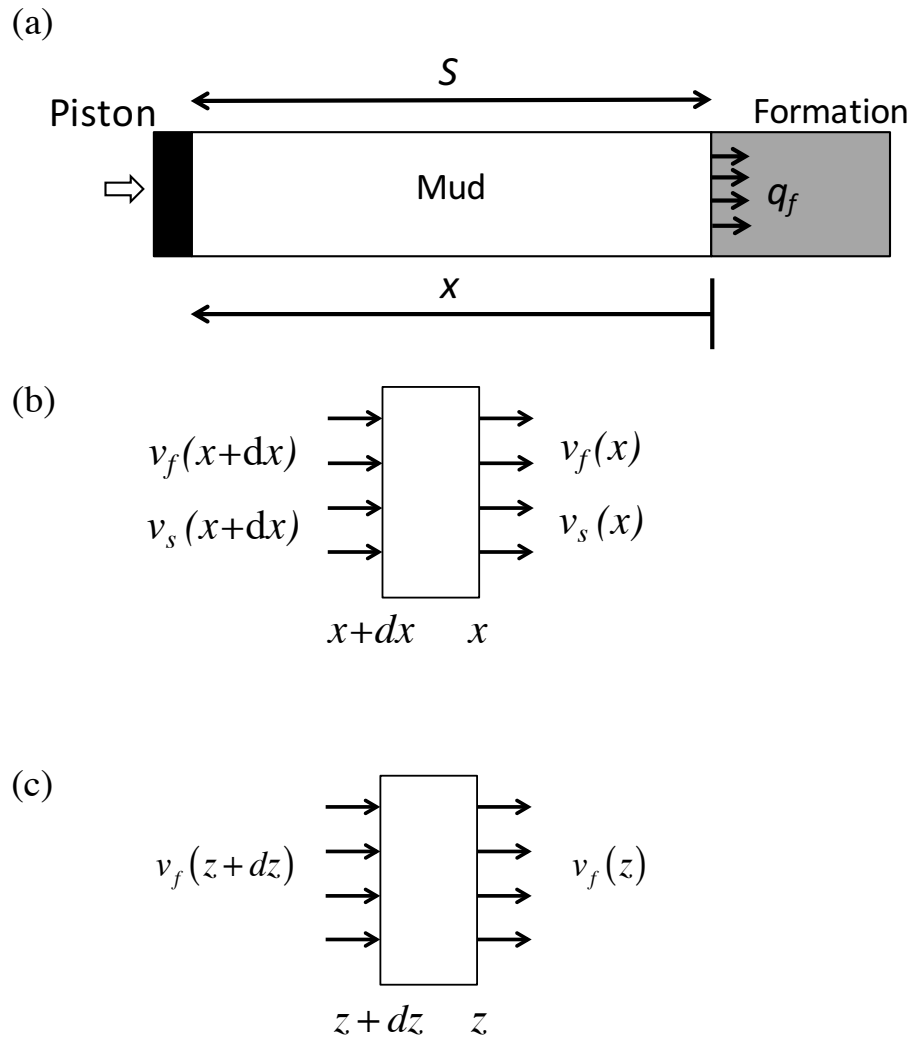


Figure 5.1. Piston model. (a) Schematic representation of the piston model. (b) An infinitesimal element in the Eulerian system. (c) An infinitesimal element in the Lagrangian system.

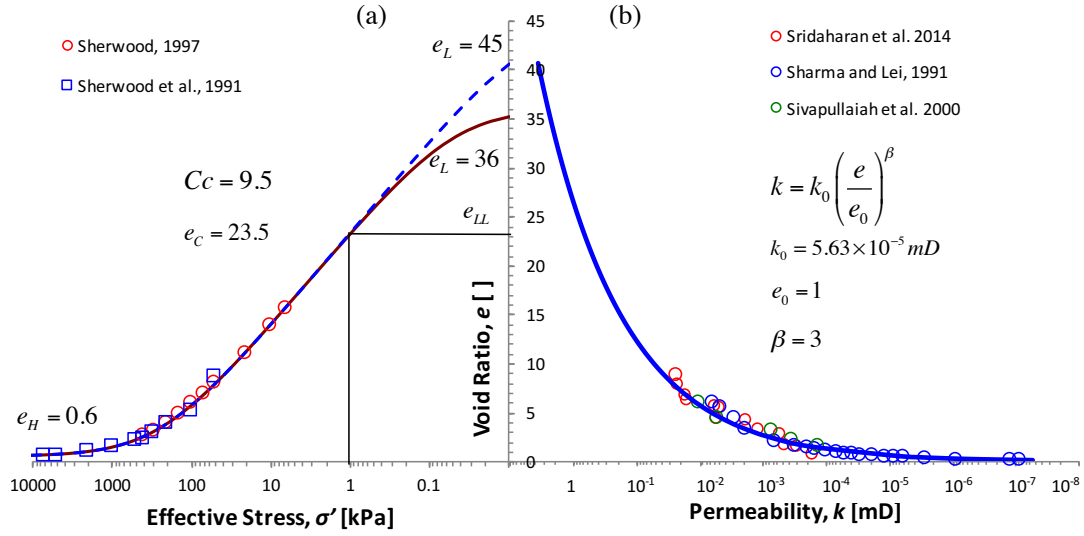


Figure 5.2. Constitutive equations of sodium bentonite. (a) Effective stress vs. void ratio. (b) Permeability vs. void ratio. (Data from: Sharma and Zongming 1991, Sherwood et al. 1991, Sherwood and Meeten 1997, Sivapullaiah, Sridharan et al. 2000)

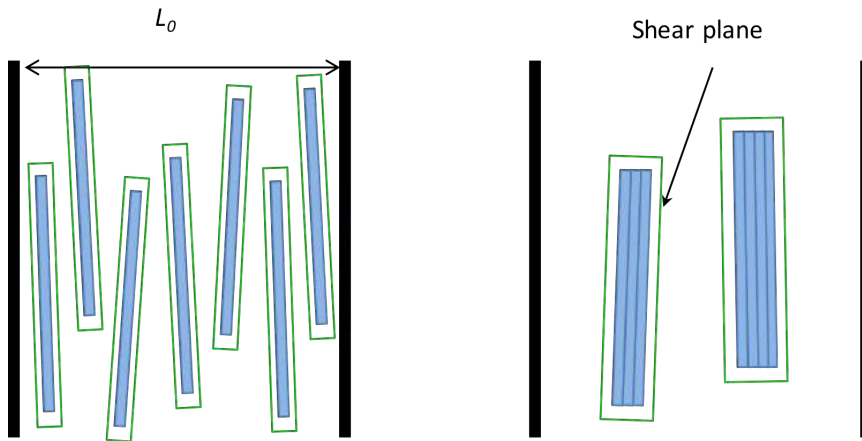


Figure 5.3. Impact of environmental factors on the bentonite fabric: dispersed and aggregated clay platelets.

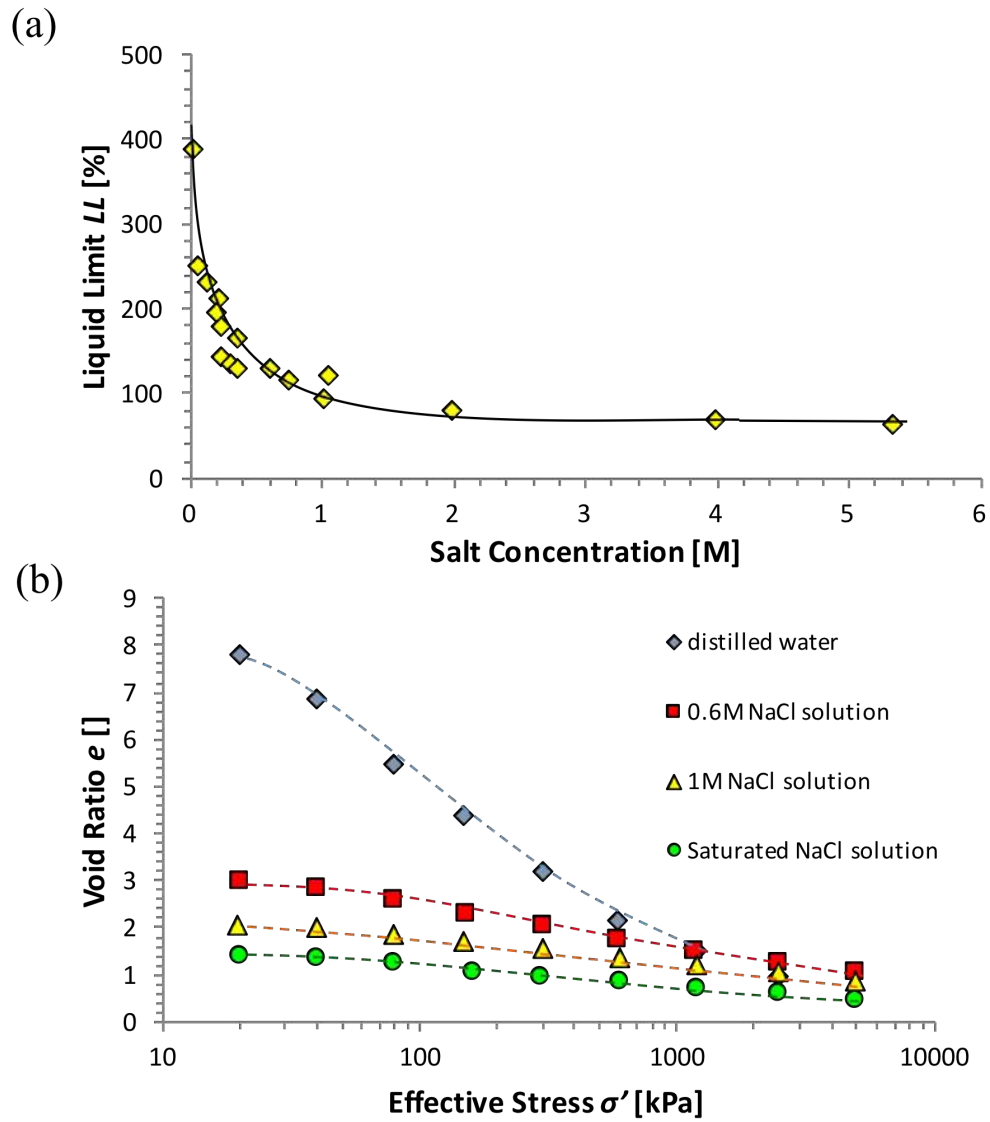


Figure 5.4. Environmental factor: ionic concentration. (a) The influence of the salt concentration on the liquid limit of sodium bentonite. Data from: Schmitz et al., 2003. (b) Odometer curves for bentonite reconstituted with and immersed in NaCl solutions at various concentrations. (Data from: Di Maio et al., 2004)

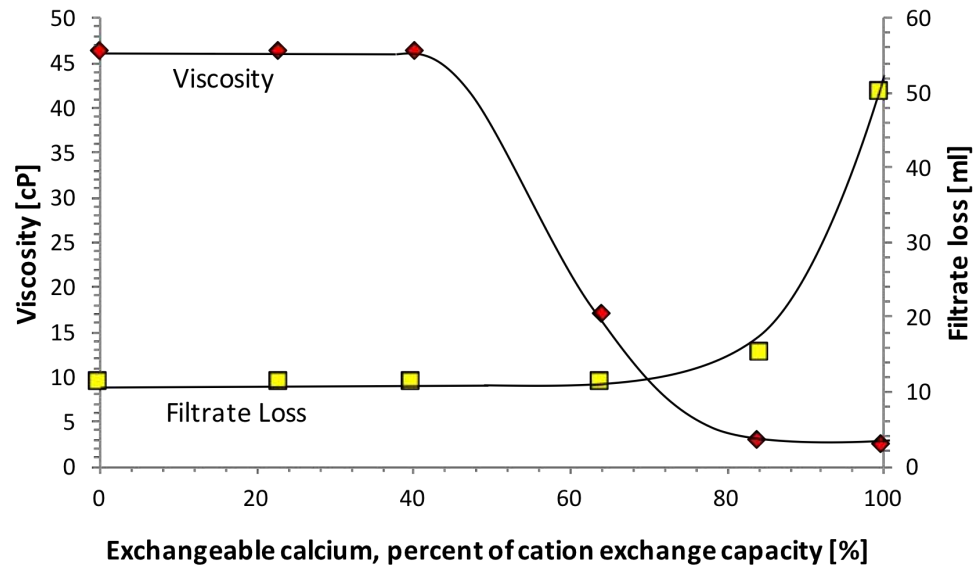


Figure 5.5. Viscosity and filtration loss properties at 4% bentonite as a function of the amount of exchangeable calcium. Filtration loss in API tests. (Data from: Williams et al. 1953).

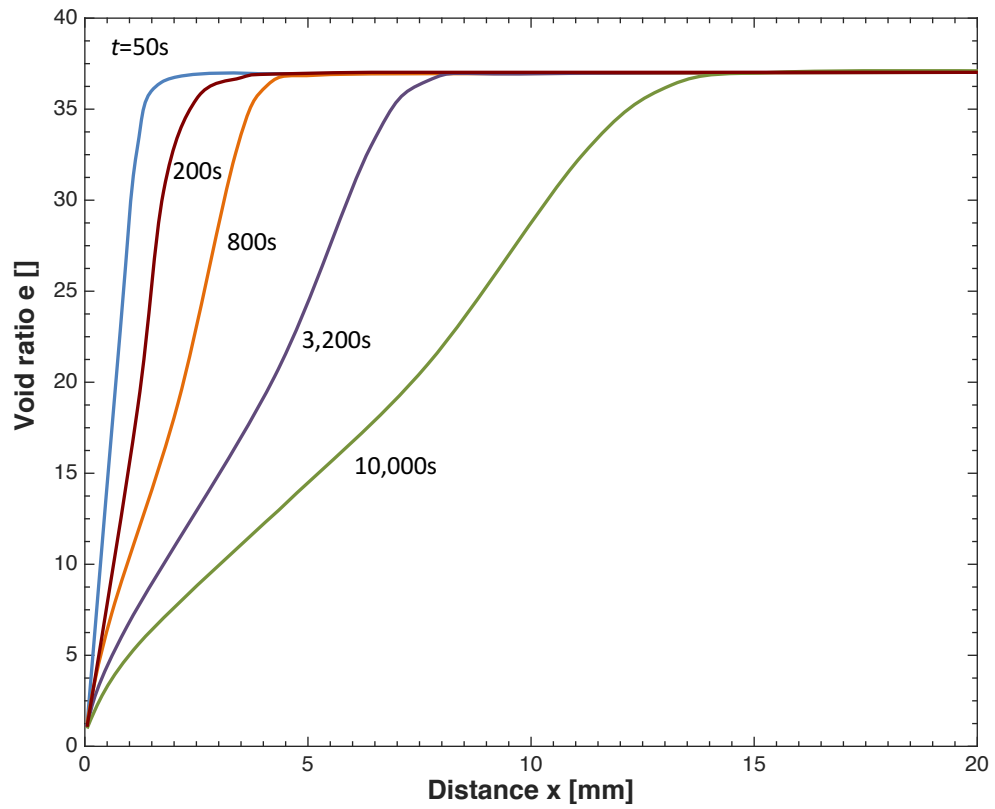


Figure 5.6. Cake formation: the influence of filtration time. Void ratio profiles at 50s, 200s, 800s and 3,200s for a 2MPa filtration pressure. Constitutive parameters are in Table 2.

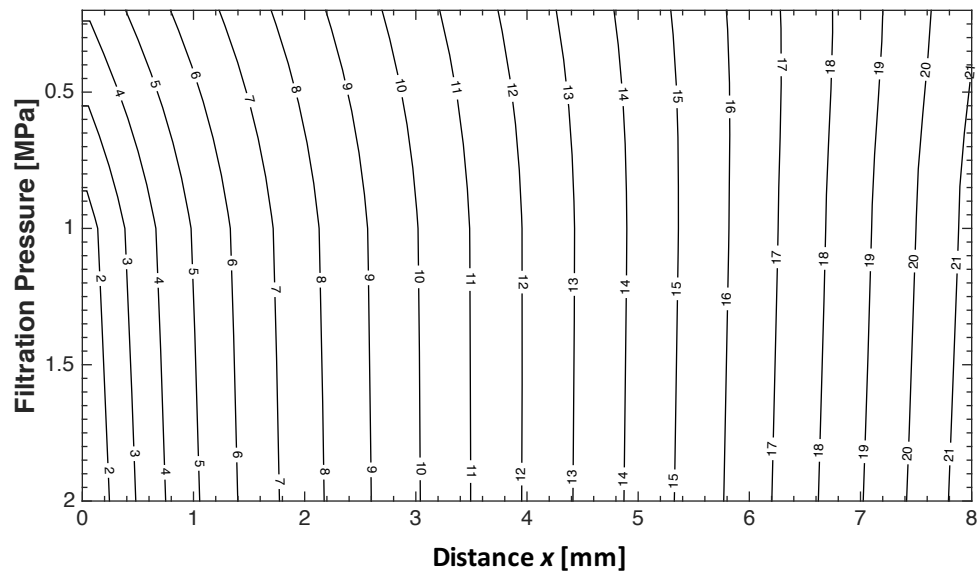
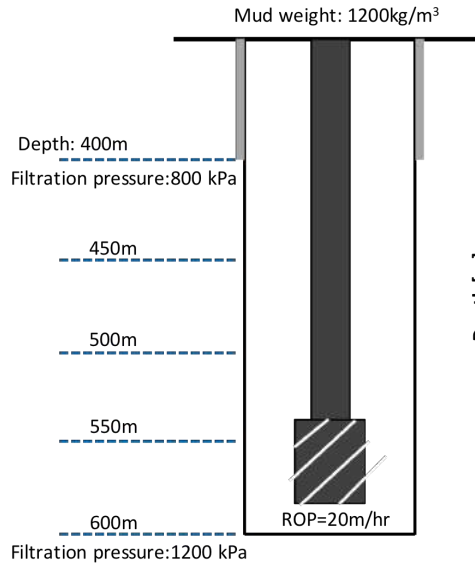
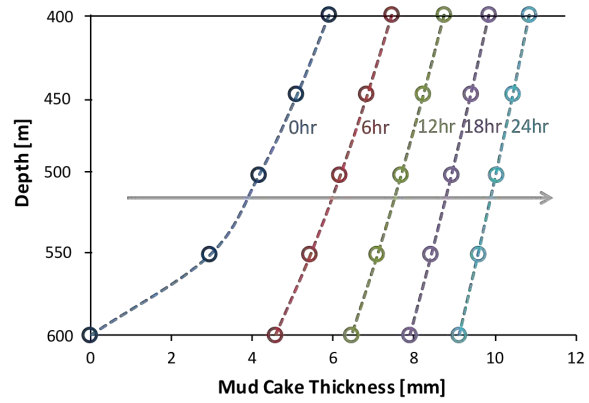


Figure 5.7. Cake formation: the effect of filtration pressure. Void ratio contours versus wellbore depth presented in terms of filtration pressure. Filtration time=2.8hr at all depths.



(a)



(b)

Figure 5.8. Cake formation: the effect of time. (a) Case: from 400m to 600m depth and rate of penetration ROP=20m/hr. (b) Increasing mudcake thickness ( $e=10$ ) with increasing still-time from 0hr to 24hr.



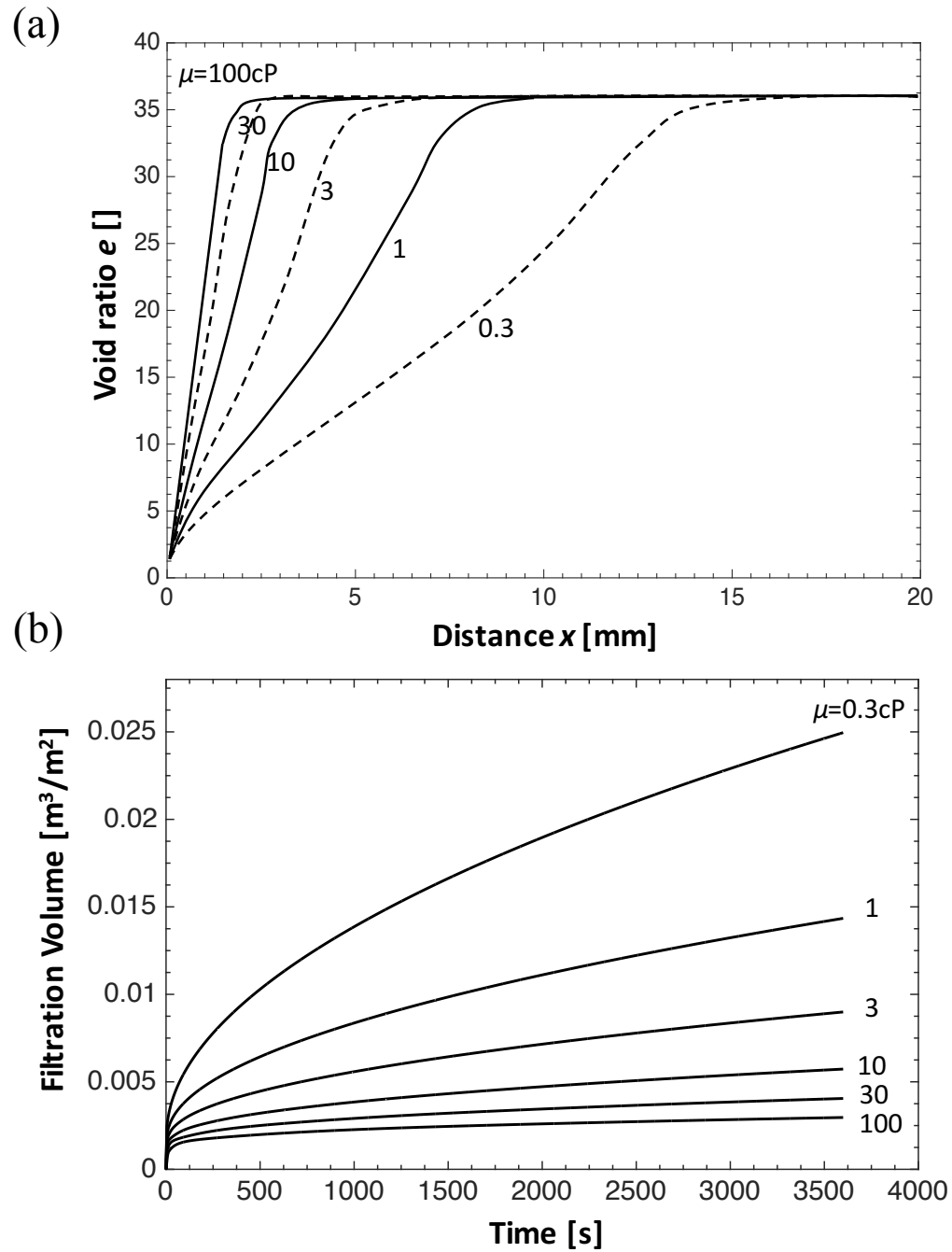
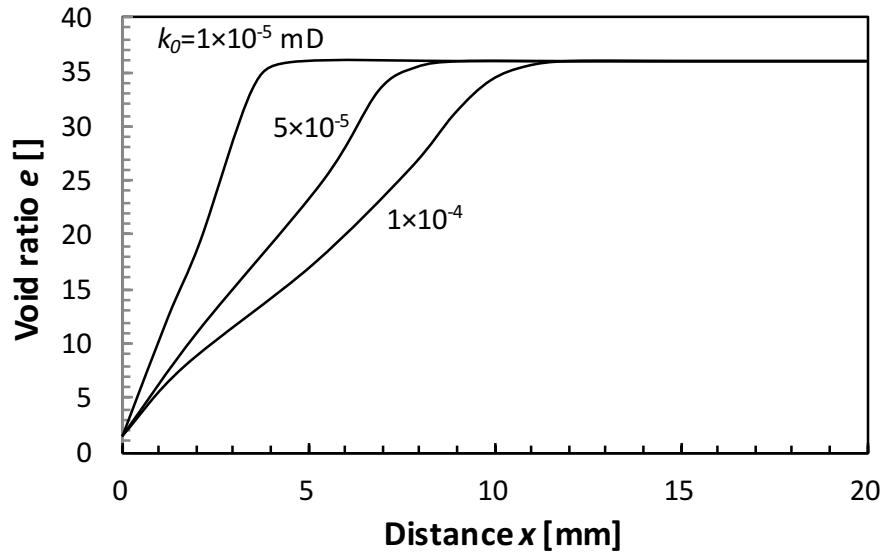


Figure 5.9. The influence of the liquid viscosity on the filtration behavior. (a) Void ratio profile. (b) Cumulative filtration volume. Fluid viscosities between 0.3cp and 100cp, filtration pressure=1MPa and filtration time=1hr.

(a)



(b)

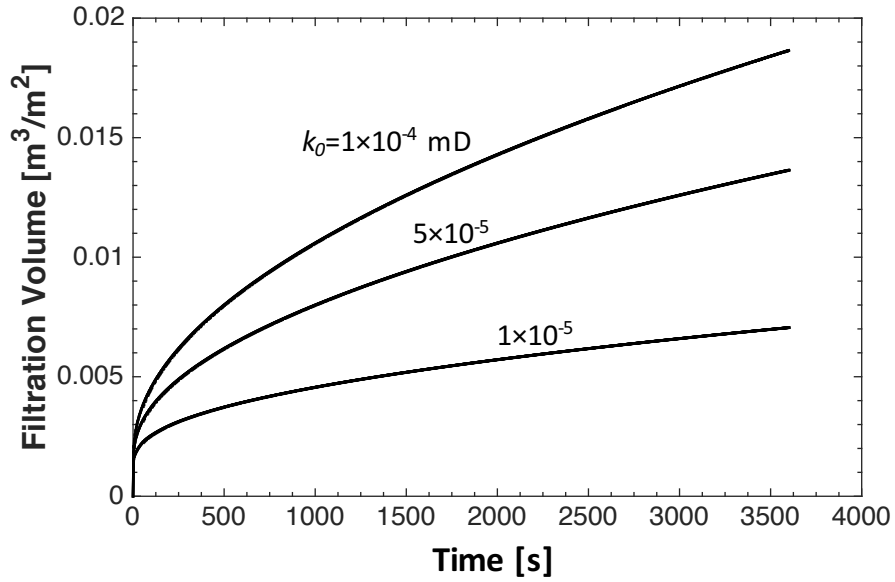


Figure 5.10. The influence of permeability on the filtration response. (a) Void ratio distribution. (b) Cumulative filtration volume. Reference permeability  $k_0 = 1 \times 10^{-5}$  mD,  $5 \times 10^{-5}$  mD and  $1 \times 10^{-4}$  mD, filtration pressure=1MPa and filtration time=1hr.

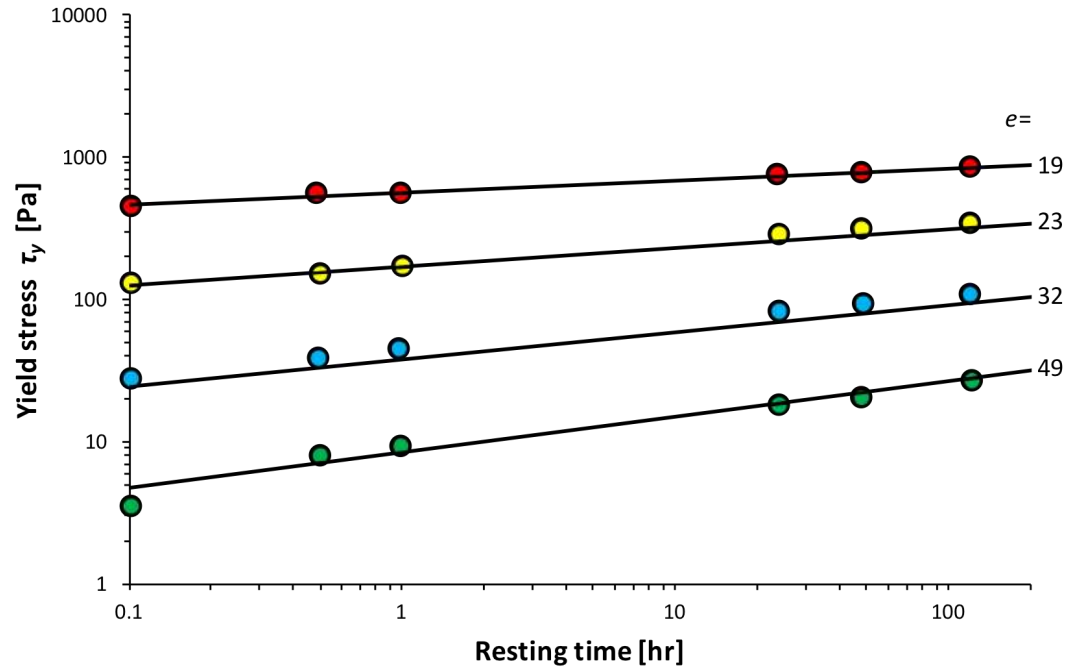


Figure 5.11. Thixotropic behavior of bentonite suspension with void ratio  $e=19, 23, 32$  and  $49$ . Solid lines are the model prediction (Equation 12) and symbols are measured values. (Data from: El Mohtar and Yoon 2013)

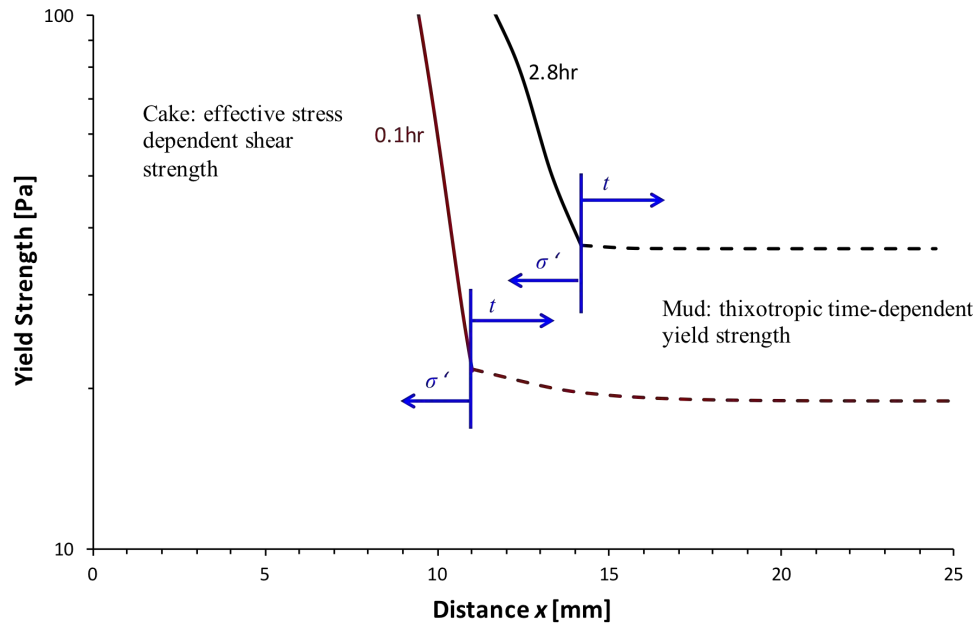


Figure 5.12 Yield Strength. Effective stress dependency in the cake, and thixotropic time-dependency in the mud.

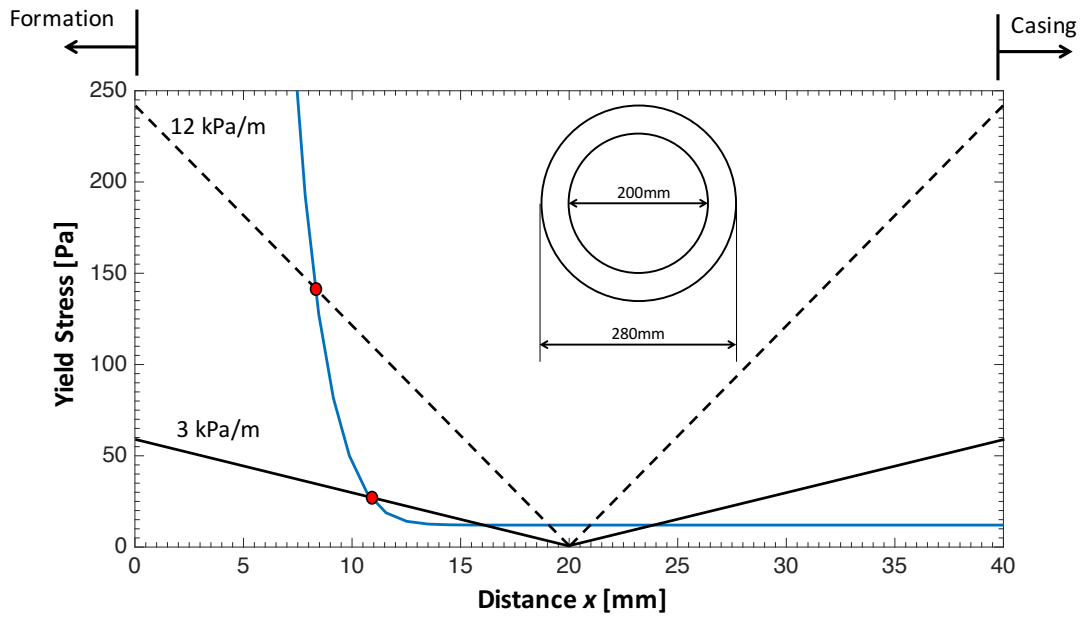


Figure 5.13. Residual cake thickness after cement invasion. Black lines: shear stress imposed by the invading cement. Blue line: cake-mud shear strength (refer to Figure 5.12).

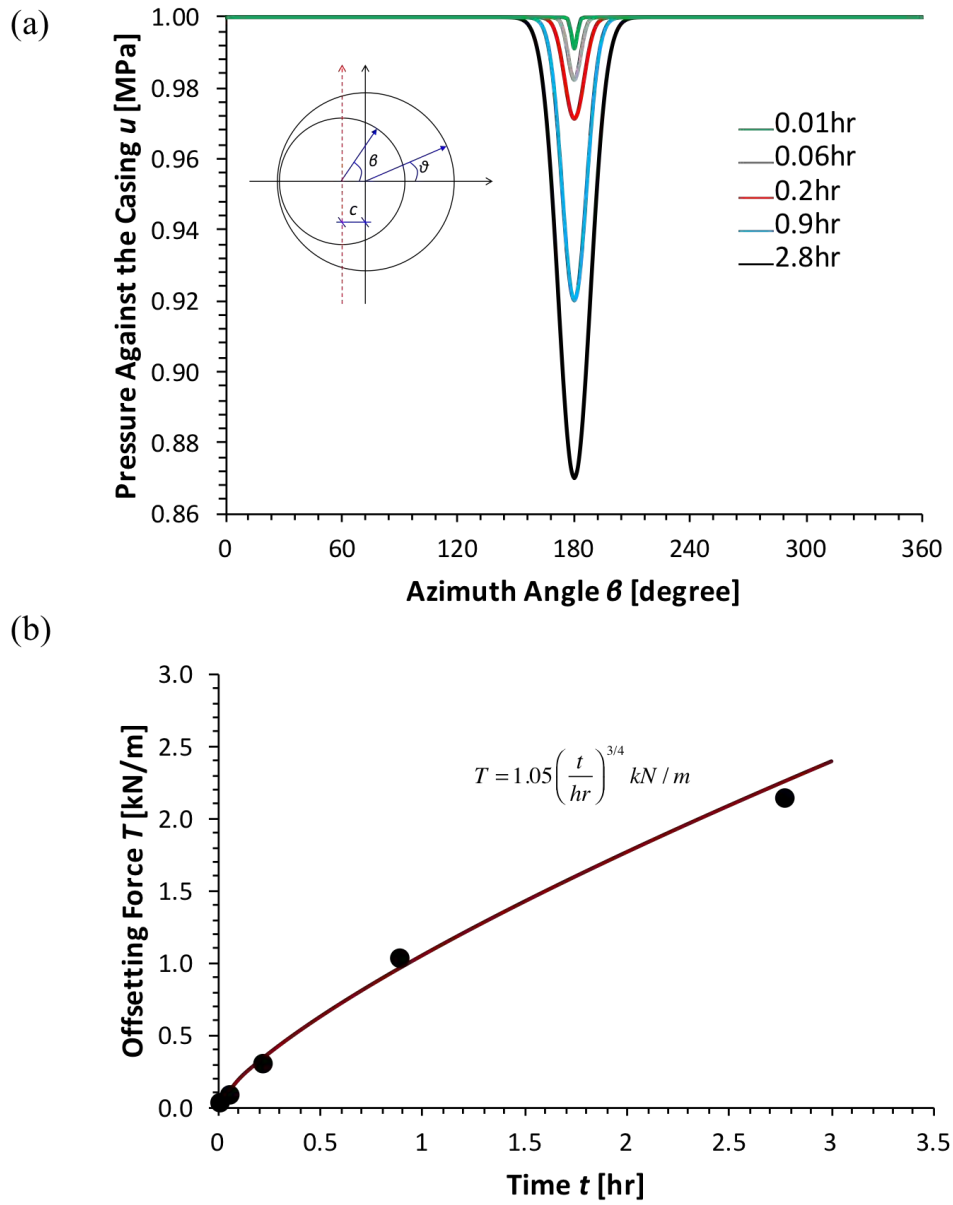


Figure 5.14. “Stuck pipe” by differential pressure sticking. (a) Fluid pressure against the casing for a 1MPa filtration pressure. (b) The effect of the still-time  $t$  on the total force against the pipe  $T$ .

## CHAPTER 6. MAGNETIC WATER BASED DRILLING MUD

### 6.1 Introduction

Drilling mud removes cuttings from the wellbore, reduces friction between the drill pipe or casing and the wellbore, cools and cleans the bit, coats the formation with a thin, low-permeability filter cake, maintains wellbore stability, and minimizes formation damage (Caenn *et al.*, 2011).

The addition of a tracer material in drilling fluids allows the measurement of the fluid movement around the borehole which is critical for the identification of several important events, such as lost circulation, mudcake formation, and cement displacement. Radioactive tracers have been used for decades to determine flow rate and flow profiles, evaluate completion problems and treatment effectiveness (Flagg *et al.*, 1955; Bateman, 2016). Recently, magnetic particles serve as a high magnetic susceptibility tracer (Aderibigbe *et al.*, 2016) and contrast agent in NMR for formation characterizations (Kenouche *et al.*, 2014; An *et al.*, 2017).

Previous studies on bentonite-based magnetic materials have been driven by waste water treatment needs (Oliveira *et al.*, 2003; Mockovčiaková, Orolínová and Škvarla, 2010; Wu *et al.*, 2012; Lian *et al.*, 2014). Preparations of magnetic bentonite can use either chemical synthetic methods (Oliveira *et al.*, 2003) or by mixing iron oxide nanoparticles with the bentonite slurry (Vipulanandan, Mohammed and Samuel, 2017). However, currently available magnetic bentonite materials are expensive for the massive applications involved in the oil/gas industry.

This chapter aims to develop an economical and stable magnetic drilling mud for wellbore monitoring. A systematic study of the suspension stability, rheological properties, and magnetic hysteresis guides the engineering of an optimal magnetically sensitive drilling fluid. Chapter 7 documents a wellbore monitoring method based on the magnetic drilling mud.

## **6.2 Materials and Methods**

### *6.2.1 Materials*

We selected readily available magnetite ( $\text{Fe}_3\text{O}_4$ ) particles with an average diameter of  $\sim 50\mu\text{m}$  (Sigma-Aldrich). The bentonite is obtained as a powder form (Delmon Co. Ltd, KSA). The long-term stability is critical to the application of this magnetic drilling mud. Therefore, we add surfactants to assist the suspension of  $\text{Fe}_3\text{O}_4$  particles in bentonite mud. Surfactants tested in this study include anionic surfactant SDS, cationic surfactant CTAB, and nonionic surfactant Tween 20 (Sigma-Aldrich, with a purity  $>99\%$ ). Figure 6.1 shows molecule structures of three surfactants.

The X-ray diffraction XRD analysis (Rigaku Minibenchtop-600) of the bentonite powder is based on samples that pass through the 200-mesh size. Samples are analyzed with parallel beam optics, Cu  $K\alpha$  radiation at 40kV and 15mA. Results show that the bentonite consists of sodium montmorillonite  $(\text{Na,Ca})_{0.33}(\text{Al, Mg})_2(\text{Si}_4\text{O}_{10})(\text{OH})_{2n}\text{H}_2\text{O}$  (2 $\theta$  peaks at 7.511, 28.121, 35.101, 48.021, 52.311 and 76.201).



The ICP-OES spectrometer determines the cations available in the bentonite. Figure 6.2 shows that sodium cation is dominant among all cations while a small amount of other cations is present in the bentonite.

#### *6.2.2 Suspension preparation*

The raw bentonite slurry is prepared with the bentonite powder and deionized water by agitating the mixture for 30 minutes in a constant speed blender (Model 20, OFITE). Then the raw bentonite mud undergoes high temperature aging for 20 hours at 85°C (4 roller oven, OFI Testing Equipment) to ensure dispersion and hydration of bentonite platelets. Fe<sub>3</sub>O<sub>4</sub> particles and surfactants are added into the aged bentonite slurry and mixed for 30 minutes in a stand mixer (HMD200, Hamilton Beach).

#### *6.2.3 Rheology measurement*

A HPHT rotational viscometer (M5600, Grace Instrument) assesses rheological properties. Experiments are performed with shear rates which range from 10s<sup>-1</sup> to 500 s<sup>-1</sup> under different temperatures.

#### *6.2.4 Magnetic hysteresis measurement*

The Physical Property Measurement System (PPMS, Quantum Design) determines the magnetic hysteresis curves. We use customized Teflon capsules to load the suspensions. Tests include the raw Fe<sub>3</sub>O<sub>4</sub> particles and drilling fluids with 0.1%, 1% and 10% by mass of Fe<sub>3</sub>O<sub>4</sub>.

## 6.3 Results and Analyses

### 6.3.1 Dispersion stability

The Fe<sub>3</sub>O<sub>4</sub> micro particle is inherently unstable in the bentonite slurry due to the high density ( $\rho=5.17\text{g/cm}^3$ ). Figure 6.3 shows the effects of particle sizes and fluid viscosity on the terminal velocity  $v_T$  of Fe<sub>3</sub>O<sub>4</sub> particles:

$$v_T = \frac{d^2(\rho_s - \rho_f)g}{18\mu} \quad (6.1)$$

where  $\rho_s$  and  $\rho_f$  are the density of the solid particle and fluid respectively,  $d$  is the diameter of the particle, and  $\mu$  the viscosity of the fluid. Micro particles have a much higher terminal velocity compared to sub-micro particles even at high viscosity. High terminal velocity leads to rapid separation of particles from the liquid phase.

Figure 6.4 shows the stability of suspensions stabilized by the three surfactants selected for this study (Figure 6.1). A suspension without surfactant is used as the control group for comparison. All samples are prepared with 5% Fe<sub>3</sub>O<sub>4</sub> particles, 2% bentonite, and 8mM surfactant. Nonionic surfactant Tween-20 does not show any significant contribution to the stability of suspensions. Both cationic surfactant CTAB and anionic surfactant SDS improve the stability of the suspension. After two hours settling time, the suspension stabilized by CTAB starts to show separation between the solid particle phase and the bentonite mud phase. SDS stabilized suspension has the best stability among all test samples.

The influence of the concentration of SDS on the suspension stability has also been investigated (Figure 6.5). At low concentrations ( $C_{\text{SDS}} < 4\text{mM}$ ), we immediately observe the settlement of  $\text{Fe}_3\text{O}_4$  particles. A stable suspension forms with  $C_{\text{SDS}} = 4 \sim 8\text{mM}$ . A high concentration of SDS ( $C_{\text{SDS}} > 16\text{mM}$ ) leads to co-sedimentation of bentonite and iron oxide particles, where we observe a completely clear upper layer. The same settlement tests were conducted under different temperature conditions ( $20^\circ\text{C}$  to  $85^\circ\text{C}$ ) and with identical results. Suspensions are stable in all temperature ranges with  $C_{\text{SDS}} = 4 \sim 8\text{mM}$ . This optimum concentration range is close to the critical micelle concentration (CMC) of SDS ( $8.2\text{mM}$  at  $25^\circ\text{C}$ ). Obviously, a higher bentonite mass concentration ( $> 2\%$ ) can further improve the stability of the suspension due to the large viscosity.

### 6.3.2 Rheological properties

Rheology is a critical property of drilling fluids. The viscosity of bentonite suspensions is sensitive to the existence of additives and contaminants. We systematically investigated the influence of  $\text{Fe}_3\text{O}_4$  particles and SDS on the rheological behaviors of the bentonite mud under different temperatures.

Figure 6.6 illustrates the rheological behaviors of the bentonite- $\text{Fe}_3\text{O}_4$ -SDS system. Figure 6.6 (a) and (b) show results of suspensions based on 2% and 3% bentonite. Generally, samples based on 3% bentonite mud have a higher viscosity compared with samples based on 2% bentonite mud due to the increase in bentonite concentration. All fluids show a shear-thinning behavior which is consistent with the rheological behavior of the raw bentonite suspension.

The addition of  $\text{Fe}_3\text{O}_4$  particles and SDS has a similar influence on the viscosity of 2% and 3% bentonites. We observe a significant decrease in the viscosity of the suspension compared with raw bentonite with the addition of 1%  $\text{Fe}_3\text{O}_4$  particles. However, with the coexistence of SDS and  $\text{Fe}_3\text{O}_4$  particles, the viscosity of suspensions increases with the increased concentration of  $\text{Fe}_3\text{O}_4$  particles. The sample with 5%  $\text{Fe}_3\text{O}_4$  and 8mM SDS is almost double the viscosity of raw bentonites. The synergistic effect between bentonite- $\text{Fe}_3\text{O}_4$ -SDS is responsible for the increase in viscosity.

Temperature alters the rheological characteristics of clay pastes through a combination of competing effects: increased platelet Brownian motion and hindered bond formation, increased Debye-Huckel length and inter-particle repulsions, faster aggregation towards a minimum potential energy configuration, and decreased fluid viscosity (Liu and Santamarina, 2017). For example, the viscosity of water decreases from 1cP to 0.3cP when the temperature increases from 20°C to 90°C. The viscosity of test fluids (3% bentonite+5%  $\text{Fe}_3\text{O}_4$  particles+8mM SDS) decreases monotonically with the increased temperature (Figure 6.7).

### 6.3.3 *Magnetic properties*

Figure 6.8(a) shows the magnetic hysteresis loops of the magnetic mud with  $\text{Fe}_3\text{O}_4$  concentration 0.1%, 1%, and 10% under the temperature  $T=300\text{k}$ . All three samples display typical ferromagnetism. The saturation magnetizations (at 10 kOe) are 0.125 emu/g, 0.843 emu/g, and 6.656 emu/g for 0.1%, 1%, and 10%  $\text{Fe}_3\text{O}_4$  respectively. Residual magnetizations (at 0 Oe) are 0.0065 emu/g, 0.0149 emu/g, and 0.0669 emu/g. The

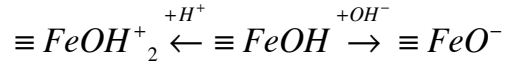
saturation magnetization for pure micro-size Fe<sub>3</sub>O<sub>4</sub> powder is 95.923 emu/g and the residual magnetization is 8.434 emu/g.

We freeze samples to compare the magnetic properties of liquid and solid mixtures. Figure 6.9 presents magnetic hysteresis curves of 10% Fe<sub>3</sub>O<sub>4</sub> mass fraction samples at temperature T=250k and T=300k.

## 6.4 Discussion

### 6.4.1 Bentonite-surfactant-Fe<sub>3</sub>O<sub>4</sub> interactions

Surface charge When an iron oxide surface comes in contact with water, a hydroxylated surface can form. The surface charge of the iron oxide surface is dependent on protonation/deprotonation of the hydroxyl groups when the pH of the solution changes (Parks and Bruyn, 1962; Stucki, Goodman and Schwertmann, 2012):



The point of zero charge (PZC) of Fe<sub>3</sub>O<sub>4</sub> is around pH 7.9 (Schwertmann and Cornell, 2007). Therefore, the Fe<sub>3</sub>O<sub>4</sub> particles are negatively charged in all suspensions prepared in this study.

Montmorillonite is a 2:1 clay mineral. Isomorphic substitutions (replacements of Si(IV) by Al(III), Al(III) by Fe( II ) and Mg( II )) developed within the structure result in negative charges within montmorillonite layers. This structural charge is independent of pH and generates a negative electric potential at the face of platelets (Bleam, 1990; Chang and Sposito, 1996). In addition to the structural charge, reactive groups at the edges can

experience a protonation/deprotonation process. Thus, the edge can become positively or negatively charged depending on the pH of the solution. The isoelectric point of the edge is less than pH=5 (Pecini and Avena, 2013). Therefore, both the face and edge of montmorillonite platelets are negatively charged in our experimental conditions.

Bentonite-Tween20-Fe<sub>3</sub>O<sub>4</sub> system As a nonionic surfactant, Tween20 cannot interact with either bentonite platelets or Fe<sub>3</sub>O<sub>4</sub> particles with electrostatic forces. Therefore, Tween20 does not show any noticeable influence on the dispersion stability of suspensions.

Bentonite-CTAB-Fe<sub>3</sub>O<sub>4</sub> system The hydrophilic head of the cationic surfactant CTAB can bind onto the negatively charged bentonite platelets and Fe<sub>3</sub>O<sub>4</sub> particles via electrostatic interactions (Juang, et al., 2004; Wang *et al.*, 2015). The hydroxyl groups on the Fe<sub>3</sub>O<sub>4</sub> surface can also form hydrogen bonds with CTAB molecules which may enhance the interaction between Fe<sub>3</sub>O<sub>4</sub> and CTAB (Saïen and Gorji, 2017). Thus, it seems likely the tail-tail interaction between CTAB coated bentonite platelets and Fe<sub>3</sub>O<sub>4</sub> contributes to the stabilization of the suspension. It is also possible that CTAB molecules serve as bridges between bentonite and Fe<sub>3</sub>O<sub>4</sub> particles and promote the formation of a stable 3-D structures.

Bentonite-SDS-Fe<sub>3</sub>O<sub>4</sub> system Surfactants like SDS with hydroxyl, carboxyl, sulfate, sulfonate, phosphate, phosphonate groups can easily bond to the hydroxyl groups of Fe<sub>3</sub>O<sub>4</sub> particles and subsequently modify their surface (Chen *et al.*, 2016). There are several possible interaction mechanisms between negatively charged bentonite platelets and anionic surfactant SDS. Ion exchange can take place between OH<sup>-</sup> ions on bentonite surfaces and the anionic part of the surfactant CH<sub>3</sub>(CH<sub>2</sub>)<sub>11</sub>OSO<sub>3</sub><sup>-</sup>. Hydrogen bonds can form between bentonite platelets and surfactant molecules. In addition, it is possible that the Ca<sup>2+</sup>

cation can establish electrostatic bridges between the anionic part of surfactants and the surface of bentonite particles (Abu-Jdayil, Ghannam and Nasser, 2016). Further studies are required to explain the high stability of bentonite-SDS-Fe<sub>3</sub>O<sub>4</sub> suspensions.

#### 6.4.2 *Magnetic properties*

The magnetic permeability and the shape of the magnetization curve for a composite is dependent upon the particle size and particle concentration. The magnetic permeability increases linearly with the amount of ferromagnetic inclusions if particles do not interact (low particle concentration and particles are homogeneously distributed). At high volume fractions, particle-particle interactions further increase the magnetic permeability of the mixture and lead to the non-linear relationship between the magnetic permeability and the amount of ferromagnetic inclusions (Adler *et al.*, 1990; Klein and Santamarina, 2000). This magnetic mud shows a similar trend to the dry mixture. The saturation magnetization and the residual magnetization are proportional to the mass fraction of Fe<sub>3</sub>O<sub>4</sub> particles (Figure 8b).

Magnetic particles in low viscosity suspensions have less residual magnetization and more noisy hysteresis curves compared with dry samples (Llandro *et al.*, 2009). However, the new magnetic mud has the same shaped hysteresis curves as solid-state ferromagnetic materials. Room temperature samples have almost the same saturation magnetization and residual magnetization as frozen samples (Figure 6.9). A possible explanation is that large particle size and high viscosity of the bentonite slurry limit physical movements of magnetic particles in the suspension, e.g. particle rotation and Brownian motion.

## 6.5 Conclusions

The purpose of this study was to develop an economical and stable ferromagnetic drilling fluid for wellbore monitoring purposes. We added micro-size  $\text{Fe}_3\text{O}_4$  particles to magnetize the bentonite suspension and included surfactants to stabilize the mixture.

The anionic surfactant SDS is most effective at improving the suspension stability compared to the other surfactants (Tween 20 and CTAB). The optimal SDS concentration is between 4~8mM which is close to its critical micelle concentration.

The magnetic drilling mud shows typical ferromagnetic behavior. The saturation and residual magnetization are proportional to the mass fraction of  $\text{Fe}_3\text{O}_4$  particles.

The new magnetic drilling fluid has potential applications in wellbore monitoring, lost circulation treatment, and waste water treatment.




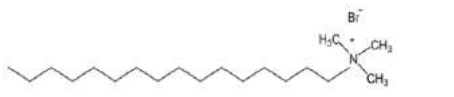
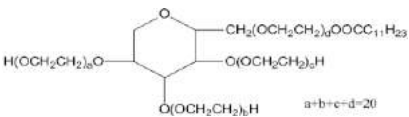
Surfactant	Structure
Sodium Dodecyl Sulfate (SDS)	
Cetyl Trimethyl Ammonium Bromide (CTAB)	
Tween 20	

Figure 6.1. Molecular structures of SDS, CTAB and Tween 20

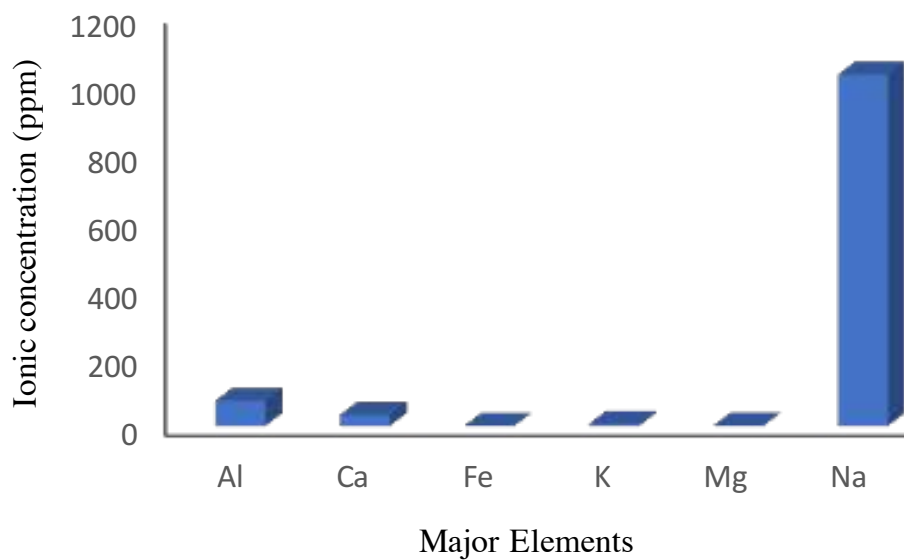


Figure 6.2. Ionic concentration (ppm). Major element in the bentonite sample.

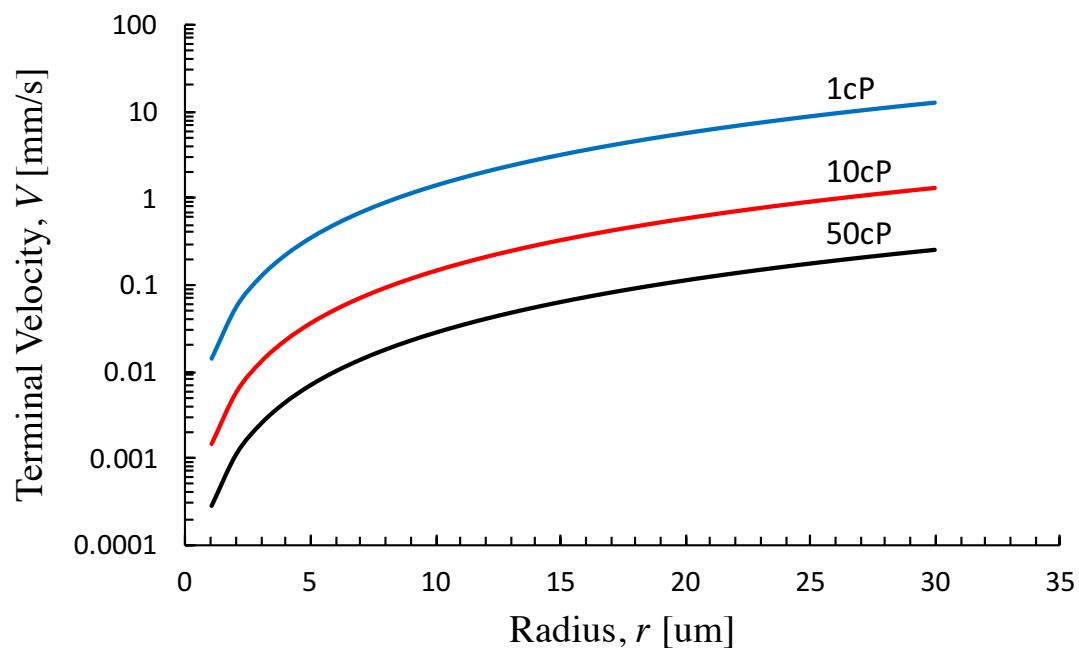


Figure 6.3. Terminal velocity as a function of particle radius and fluid viscosity. Note: the analytical solution is valid for individual spherical particles.

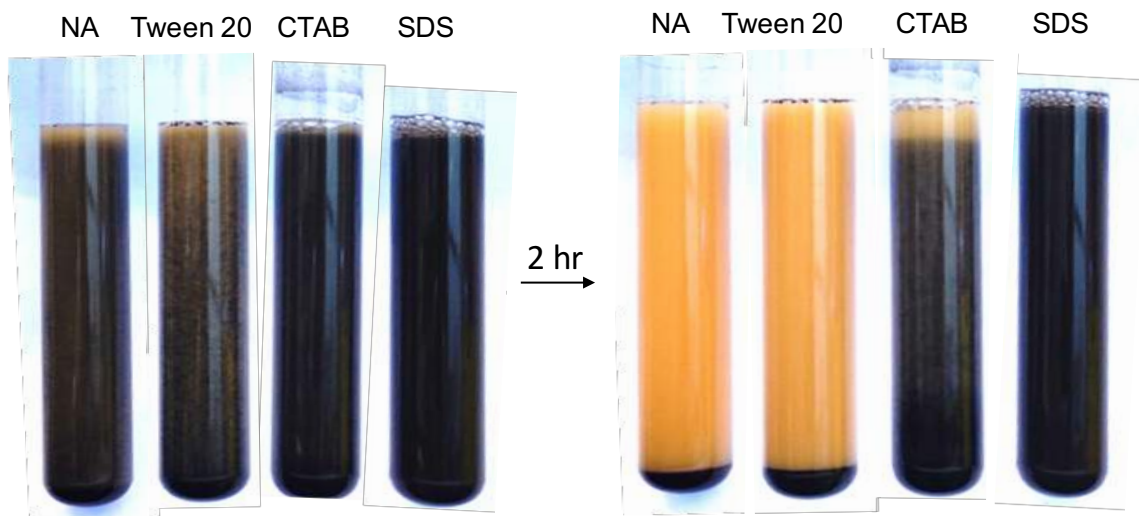


Figure 6.4. The influence of surfactant types on the stability of bentonite- $\text{Fe}_3\text{O}_4$  suspensions.  
 Note: 5%  $\text{Fe}_3\text{O}_4$ , 2% bentonite and 8mM surfactant.

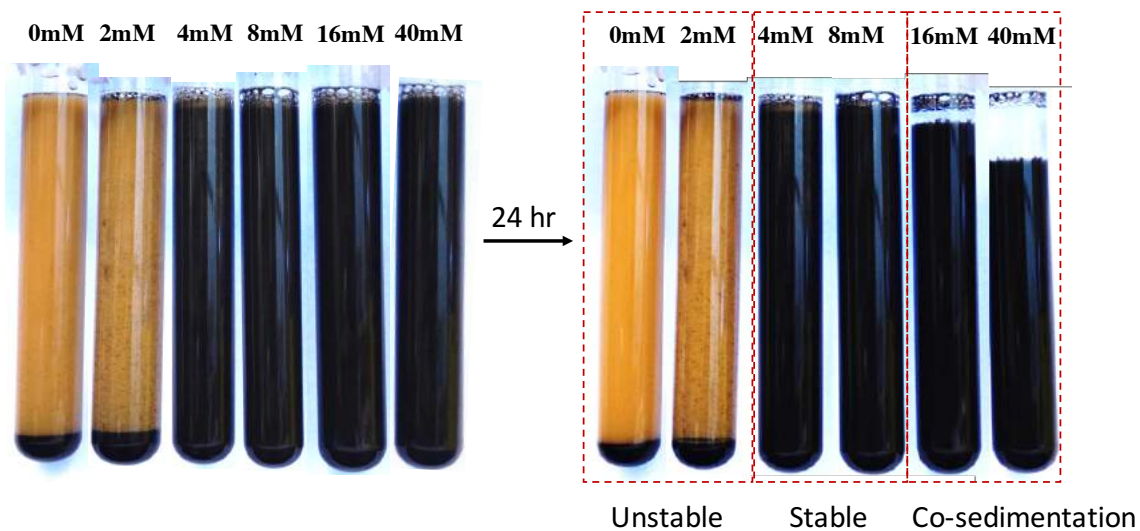


Figure 6.5. The influence of the SDS concentration on the stability of bentonite- $\text{Fe}_3\text{O}_4$  suspensions.

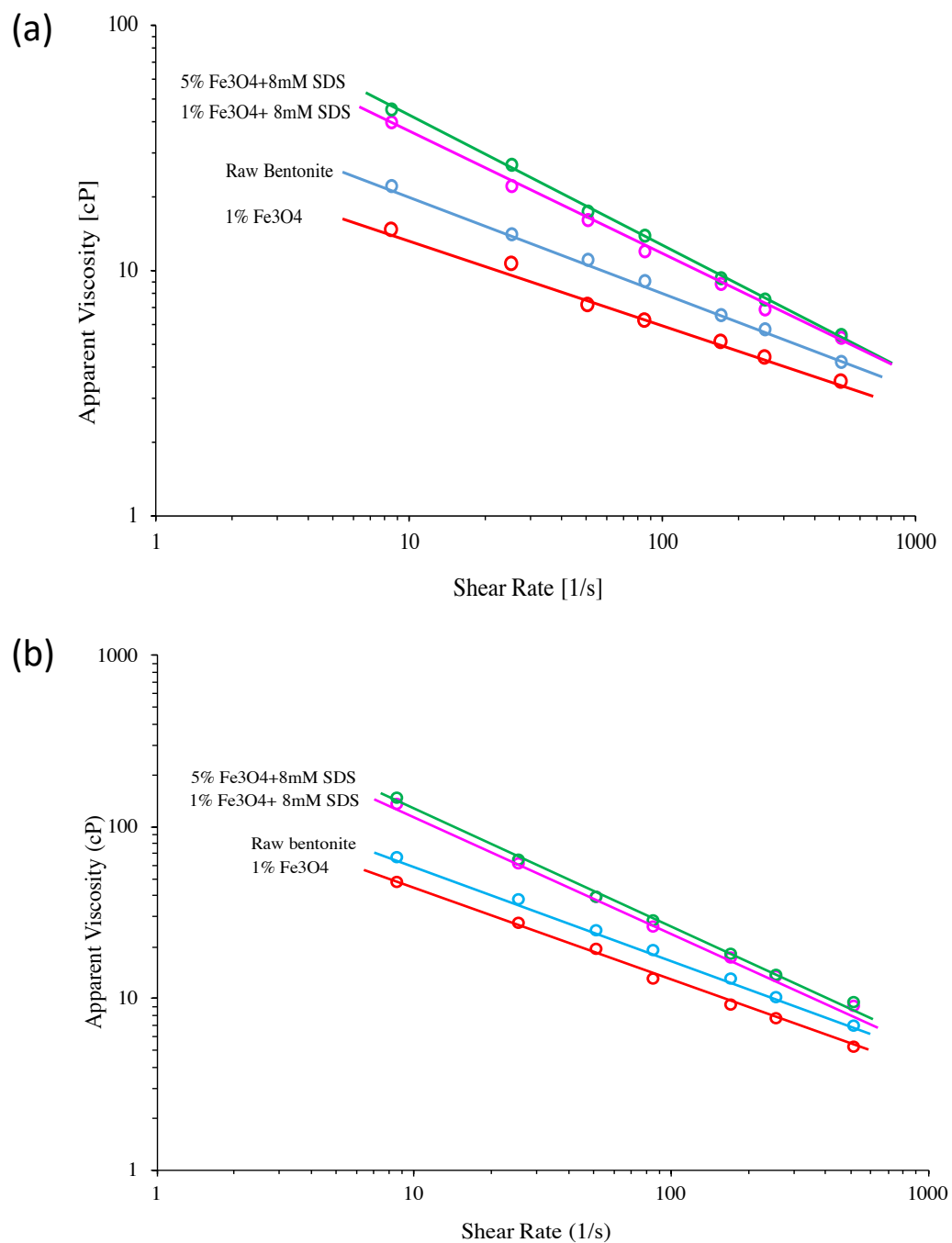


Figure 6.6. The influence of the SDS concentration on the stability of benotnite-Fe<sub>3</sub>O<sub>4</sub> suspensions. (a) Based on 2% bentonite mud. (b) Based on 3% bentonite mud.

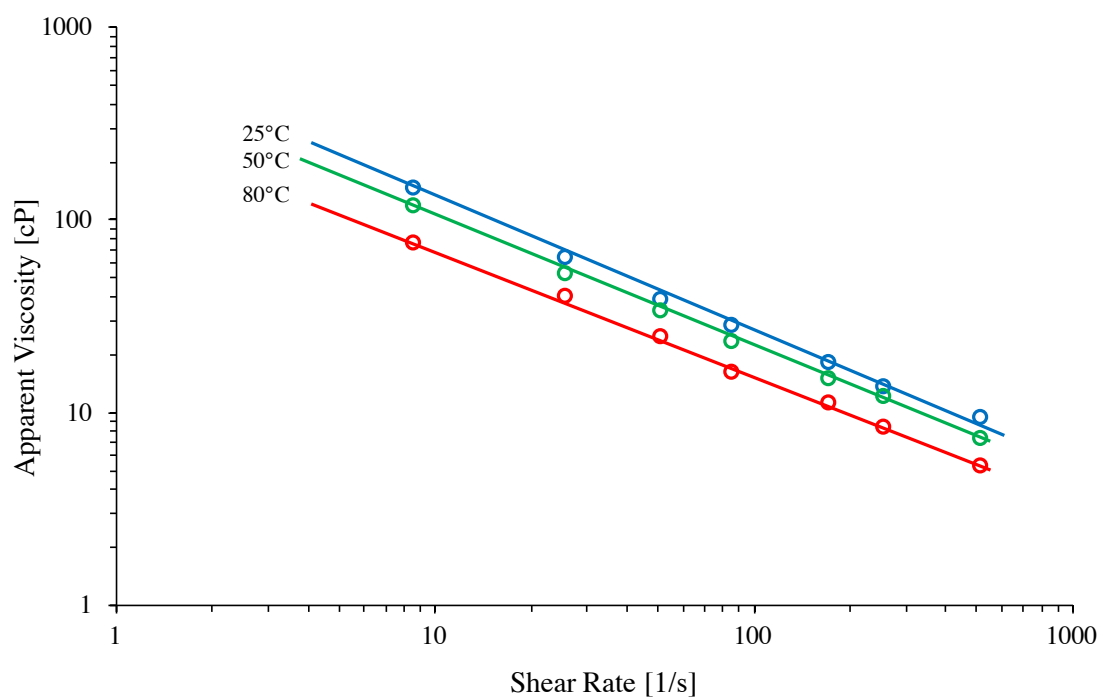


Figure 6.7. The influence of temperature on the viscosity of bentonite suspensions (3% bentonite+5%  $\text{Fe}_3\text{O}_4$  particles+ 8mM SDS).

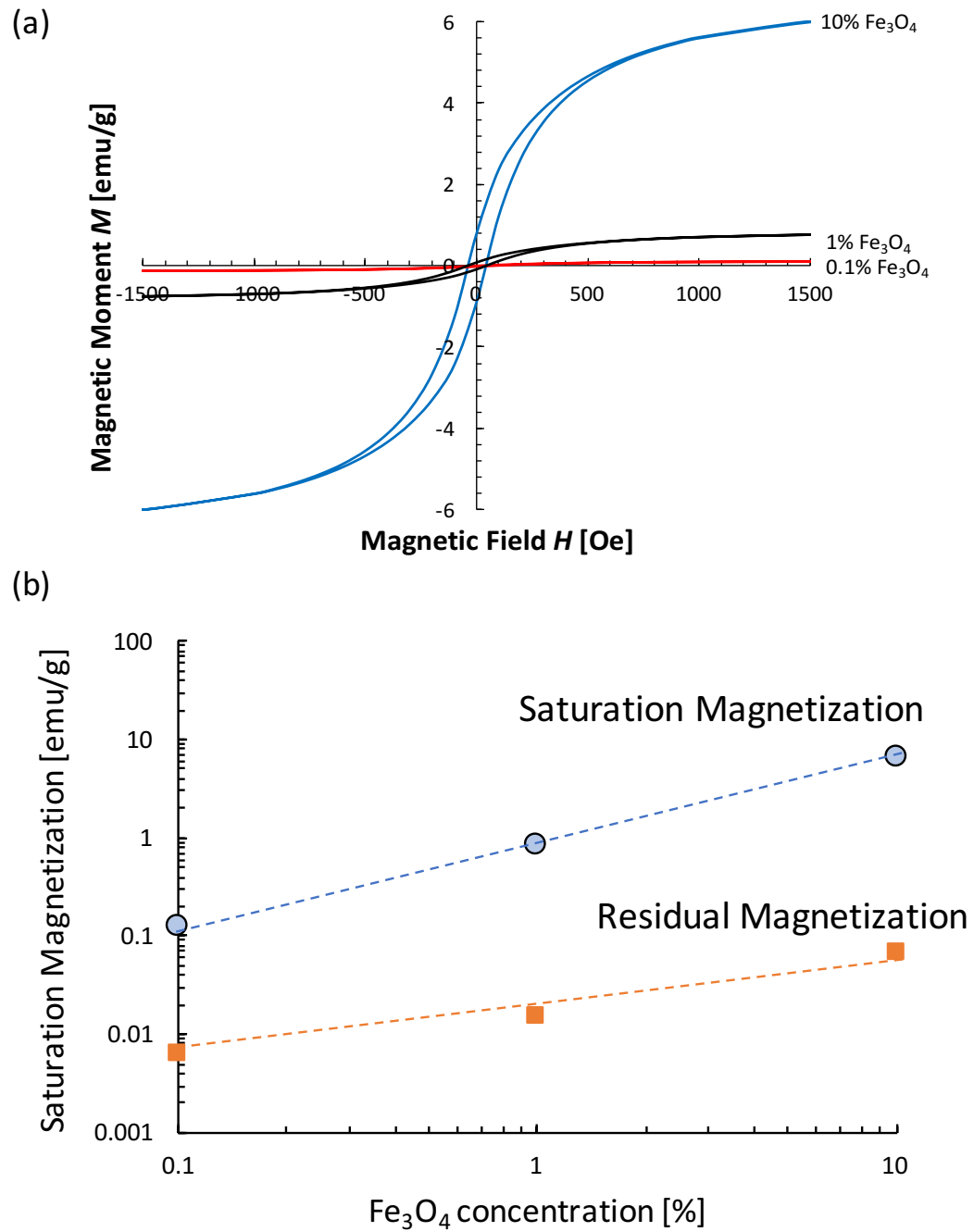


Figure 6.8. Magnetic properties of magnetic mud as a function of  $\text{Fe}_3\text{O}_4$  concentration. (a) Hysteresis curves. (b) Saturation magnetization and residual magnetization.

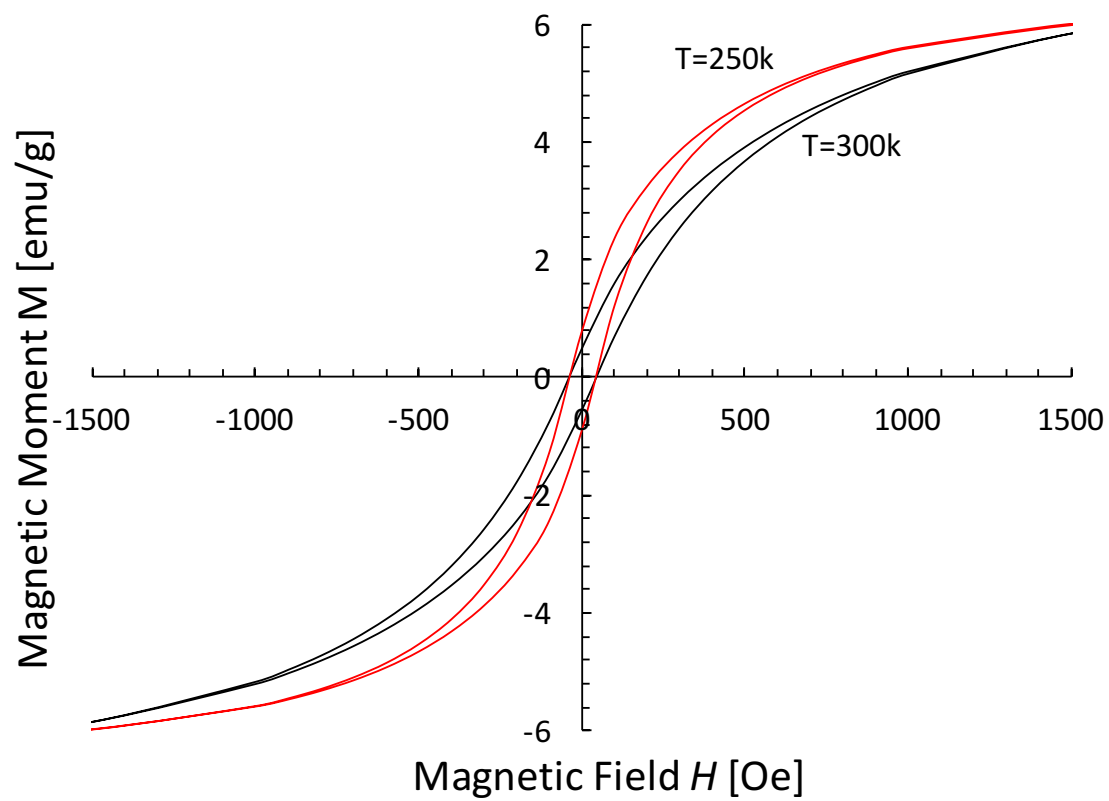


Figure 6.9. Magnetic hysteresis curves of 10%  $\text{Fe}_3\text{O}_4$  samples at  $T=250k$  and  $T=300k$ .

## CHAPTER 7. MAGNETIC TOOL FOR WELLBORE MONITORING

### 7.1 Introduction

Casings are cemented into the well to prevent formation erosion, seal lost-circulation zones, support casing, protect casing strings from corrosion, and for hydraulic zonal isolation (Guillot and Nelson, 2006). A poor cement job results in low top of cement, mud channels (especially in eccentric casing conditions), bad mud removal and washed-out boreholes (Figure 7.1).

Such conditions can lead to potential gas leaks and environmental contamination. For example, the Deepwater Horizon oil spill industrial disaster. Therefore, evaluation of the cement job is a critical operation that identifies whether the objectives of cementing have been achieved. However, quality control remains challenging for the oil/ gas industry. Cement job evaluation currently uses a variety of logging techniques based on active and passive acoustics, temperature, radioactivity and resistivity.

Magnetic measurements are among the oldest geophysical exploration techniques. Magnetic-based methods have been used to search for minerals, map basement structures, and assess natural hazards (Nabighian *et al.*, 2005). Magnetic measurements can be conducted through airborne magnetic surveys (Donovan, Forgey and Roberts, 1979; Luyendyk, 1997), marine magnetic surveys (Boyce *et al.*, 2004), satellite magnetic measurements (Maus and Kuvshinov, 2004; Maus *et al.*, 2008), and borehole magnetic surveys (Broding *et al.*, 1952; Silva and Hohmann, 1981).



High-resolution magnetic sensors can combine with magnetic drilling fluids (Chapter 6) to allow the direct measurement of the spatial distribution of ferromagnetic materials in the annular space between the casing and the formation. This chapter starts with a review of common commercially available magnetic sensors and down-hole tools. Then, we investigate the feasibility of applying high-resolution magnetic sensors as a new logging tool for well integrity evaluation. The research approach combines both numerical simulations and experimental studies.

## **7.2 Well Completion Evaluation Tools: Overview**

The assessment of cement jobs is an area which has challenged researchers and industry (Khalifeh et al., 2017). Leading technologies are reviewed next.

Acoustics logging Acoustics and ultrasonic logging are the standard tools which determine the top of cement and measure cement quality. This involves cement bond logs, variable density logs, ultrasonic pulse-echo, and flexural measurement techniques. Acoustic logs indirectly measure cement quality. The results are inferred from the degree of acoustic coupling of the cement to the casing and to the formation (Rouillac, 1994).

Noise logging This passive tool listens to the noise generated by fluid flow through a leakage pathway behind the cement casing. The intensity and frequency of noise depend on the flow rate and the geometry of the leakage pathway respectively (McKinley et al., 1973). The use of fiber optics to measure tiny strain events caused by localized acoustic energy interactions with fiber cables provides a new way to continuously monitor the entire

length of a wellbore (Bateman, 2016). However, difficulties in the interpretation of the signal and poor spatial resolution are two key limitations to the application of noise logging.

Temperature logging Temperature logs detect variations in the temperature behind the casing caused by cement hydration or fluid migration. This technique detects the top of cement before the end of cement hydration. However, it is not able to provide other information about the seal quality. Radial differential temperature logging has been used in the field to detect flow behind the casing (Cooke, 1979).

Resistivity logging Resistivity logging conducts a low-frequency A.C current from one electrode to another along the casing. A small portion of the current leaks from the casing to the cement and formation. The apparent resistivity of the adjacent material can be calculated from the leakage current (Vail *et al.*, 1993).

Radioactive tracer logging The technique involves using a gamma-ray-emitting radioactive isotope to tag the material placed downhole, and logging measurements with a gamma-ray tool to infer the location of the tagged material (Gadekea *et al.*, 1991). It determines flow rates, diagnoses completion problems, and evaluates hydraulic fracture geometry (Scott *et al.*, 2010; Bateman, 2016).

### **7.3 Magnetic Sensing Tools: Overview**

Magnetic sensors have been used in various applications over the past few decades in the automotive, aerospace, biomedicine, computers, security, and robotics field (Lenz and

Edelstein, 2006). The following review explores commercially available magnetic sensors and potential downhole applications.

### 7.3.1 *Magnetic Sensors*

Table 7.1 lists the sensing range of different magnetic sensors. Fluxgate magnetometers FGMs have been used to measure magnetic fields since the 1930s. A fluxgate sensor consists of a magnetic core rapped in a pick-up coil. Changes in core permeability cause the core field to change, and induce voltage in the pick-up coil (Primdahl, 1979). The measurement range, noise level, and linearity of FGM make this type of technique an appropriate sensor to measure the Earth's magnetic field (0.25-0.65 Gauss).

The Superconducting Quantum Interference Device SQUID is a very sensitive magnetometer used to measure extremely subtle magnetic fields, based on superconducting loops containing Josephson junctions (Jaklevic *et al.*, 1964). The threshold for SQUID is  $10^{-14}$  T (the magnetic fields of the heart and brain are  $10^{-10}$  T and  $10^{-13}$  T respectively). SQUID is believed to be the best tool for biomagnetic measurements, e.g. heart and brain (Wikswow, 2004).

Magnetoresistance MR refers to the change in the electrical resistance of a material in response to an applied magnetic flux density. The MR magnetometer has a high sensitivity, high temperature tolerance, and low power consumption. MR sensors have been used in commercial applications and can operate at temperatures of up to 225°C, pressures up to 20,000 psi and mechanical shocks up to 1500g (Gooneratne et al., 2017).

### 7.3.2 Downhole Applications

Magnetic sensors are used in directional drilling to navigate wells. In this case, triaxial fluxgate magnetometers work with triaxial accelerometers to measure both inclination and azimuth. Magnetic susceptibility sensors are used for fracture detection, in which magnetic propping agents fill the induced fractures (Aderibigbe *et al.*, 2016).

The complex downhole environment is characterized by high temperatures ( $>125^{\circ}\text{C}$ ), high pressures ( $>100\text{MPa}$ ), shocks and vibrations ( $>20\text{g}$ ), and chemical corrosion. Magnetic sensors have to be designed, fabricated and packaged to survive these conditions.

## 7.4 The KAUST Magnetic Logging Tool

### 7.4.1 Sensor selection and calibration

This study tested two different magnetic sensors: the fluxgate magnetometer (FGM-3h, 20 \$/each, Speak&CO) and magnetic tunnel junction sensor (STJ-220, 800 \$/each, Micro Magnetics Inc.). We conduct calibrations to expose the sensitivity and the directivity of both sensors. Figure 7.2(a) shows the responses of both sensors along the main axis at different distances from a small bar magnet. Both sensors have an acceptable resolution: the STJ-220 has a resolution of approximately 0.002 Gauss, the FGM-3h has a resolution of around 0.01 Gauss. The STJ-220 has better directivity compared with FGM-3h results from its very small cross section  $d=2\text{mm}$  (Figure 7.2(c)).

Based on the above sensor calibration results, we use a high-resolution STJ-220 sensor for single sensor detection experiments and equip a multi-sensor probe with FGM-3h sensors.

#### *7.4.2 Multi-sensor probe*

Directional measurements of the magnetic field distribution along a cased borehole use a probe equipped with seven fluxgate sensors (Figure 7.3). One sensor is installed vertically to measure the vertical component of the magnetic field. There are six sensors circumferentially equally spaced to obtain the horizontal components of magnetic fields produced from the annulus space and the formation. The diameter of the probe is 115mm, and the height is 100mm. Six centralizers (3 in the bottom and 3 in the top) ensure that the probe can run concentrically along the main axis of the casing.

Two 1:1 ratio cased borehole models are made to simulate the downhole geometries. The external cylinder has OD=8" and ID=7.5"; the internal cylinder has OD=5.5" and ID=5". The internal cylinder is placed in the center to simulate the concentric casing condition and has a uniform annulus space thickness 2". In the eccentric casing model, the internal cylinder has an offset of 15mm from the central line of the external cylinder (Figure 7.3). Cased borehole models are filled with clean silica sand to represent non-magnetic materials and the sand-iron powder mixture represents magnetic materials. The multi-sensor torpedo runs at a speed of 5cm/s in the borehole models.

#### *7.4.3 Deployment and data processing*

The proposed magnetic logging method comprises four operations:

1. Treat the well with magnetic fluids. The carrier fluids can be either drilling fluid or cement.
2. Magnetize in-situ magnetic fluids with a high-power permanent/ electrical magnet which can project large magnetic fields into surrounding geological formations.
3. Run the magnetic sensing tool through the magnetized region and collect in-situ measurement results.
4. Apply an inverse algorithm to invert measurement data to the magnetic material distribution in space.

### **7.5 Casing Selection: Shield Effect**

Gauss' law describes the distribution of the magnetic field:

$$\nabla \cdot B = 0 \quad (7.1)$$

The physical meaning of this law is that the net magnetic flux out of any closed surface is zero. Magnetic field lines must terminate on the opposite pole and cannot be stopped. However, magnetic field lines can be redirected. Magnetic field lines prefer to travel through high magnetic permeability materials. High magnetic permeability casings provide an easier path for the lines of flux to travel through and act as a screen which shields the magnetic field both inside and outside. Therefore, it is extremely difficult to conduct any magnetic measurements behind a high magnetic permeability casing.

Most of the ferroalloys (e.g. carbon steel) have a very high magnetic permeability. Table 7.2 lists the relative permeability of some common materials. Surprisingly,

Austenitic stainless steel has a relative permeability of 1.004 which is close to the relative permeability of air. Stainless steel is obtained by alloying chromium and nickel with iron, which retains the face-centered lattice even at low temperatures. It has completely different magnetic properties because of its unique crystal structure. Most kinds of stainless steel are not magnetic to any appreciable degree (Feynman et al., 1979).

We simulate the influence of casing materials on the magnetic field with COMSOL Multiphysics. Figure 7.4(a) presents a solenoid installed inside a casing. Figure 7.4(b) shows the distribution of the magnetic flux under the influence of an iron casing and a stainless steel casing. The relative permeability  $K_m = \mu_m / \mu_0$  used in the simulation is 5000 for iron and 1.004 for stainless steel.

Simulation results show that all field lines from the solenoid travel through the iron casing due to its high permeability, while the stainless steel casing has a negligible influence on the propagation of the magnetic field.

Lab experiments validate the simulation results (Figure 7.4(c)). A magnetic sensor records the changes in the magnetic field while inserting the casing (materials: plastic, steel, and stainless steel) between the sensor and a permanent magnet. The stainless steel pipe and plastic pipe both have negligible influences on the field strength, and the steel pipe shields the magnetic field generated by the permanent magnet.

## 7.6 Applications

### 7.6.1 Fracture Detection

Fractured formations are difficult to identify since they do not provide a recognizable response to any available electrical, nuclear or acoustic logging devices. The present work provides a method for detecting fractures which are capable of fluid communication with the borehole.

#### Magnetization of a fracture

Consider a fracture filled with a ferromagnetic material. When a permanent magnet/ electromagnet travel through the fracture, the fracture can be either magnetized radially or axially. Figure 7.5 shows the change of magnetization statuses of the fracture when a solenoid travels upward through the plane of the fracture. When the solenoid is below the fracture, it magnetizes the fracture radially outward from the center. Then the fracture becomes being magnetized axially when the solenoid is in the plane of the fracture. When the solenoid is above the fracture, the fracture is magnetized radially inward toward the center. Only when the magnet is at the plane of the fracture, the fracture is magnetized axially. When we conduct measurements following the magnetization, the fracture will always be magnetized radially.

#### Axial field strength of a radially magnetized ferromagnetic fracture



Figure 7.6 shows the geometric definition of a fracture filled with magnetic material. The inner radius is  $r_{in}$  and the outer radius is  $r_{out}$ , and its thickness is  $h$ . The axis  $z$  is the axis of symmetry. The upper surface is charged with a surface magnetic pole density  $+\sigma^*$  and the lower surface is charged with a surface magnetic pole density  $-\sigma^*$ . The axial component can be expressed as follows (Peng, McMurtry and Coey, 2004):

$$B_z(z) = \frac{B_r}{2} \left( \frac{1}{a_1} - \frac{1}{a_2} - \frac{1}{b_1} + \frac{1}{b_2} + \ln \left[ \frac{(1+b_1)(1+a_2)}{(1+b_2)(1+a_1)} \right] \right) \quad (7.2)$$

where

$$a_1 = \sqrt{1 + \left( \frac{z+h}{R_2} \right)^2}, \quad a_2 = \sqrt{1 + \left( \frac{z-h}{R_2} \right)^2}, \quad b_1 = \sqrt{1 + \left( \frac{z+h}{R_1} \right)^2}, \quad b_2 = \sqrt{1 + \left( \frac{z-h}{R_1} \right)^2}$$

### Experimental study

Three fracture models ( $R_1=6\text{mm}$ ,  $R_2=2, 6$ , and  $8\text{ cm}$ ) are prepared by painting the surface with the magnetic mud. A permanent magnet travels along the central axis to magnetize the fracture. Measurements of the residual magnetic field strength use a magnetic tunnel junction sensor along the central axis. The magnet and sensor are driven by a precision linear stage.

Figure 7.7 shows the measured magnetic field strength along the central axis of radially magnetized fracture models. The magnetic field strength increases when the sensor approaches the plane of the fracture and reaches the maximum at a close distance from the

plane of the fracture. The vertical component of the field strength at the plane of the fracture is zero. The directions of the vertical component are opposite at two sides of the plane of the fracture since the central symmetric feature of the magnetic field. This sharp transition highlights a noticeable signal which can recognize the existence of a fracture. Experimental results show a good agreement with the semi-analytical solutions introduced in the previous section.

In general, larger fractures generate magnetic fields with larger magnitudes. However, the size of the fracture only has a significant influence on the field strength when the size of the fracture is relatively small. Due to the rapid decay of the magnetic field with distance, the influence of the fracture size becomes negligible when its size is relatively large.

#### *7.6.2 Cement Job Evaluation*

##### Data Inversion: Parametric representation and successive forward simulation

We attempt to invert measurement data from the multi-sensor tool to infer the distribution of magnetic materials in space. The inversion of multi-sensor measurements is an inherent 3-D inverse problem. However, it can be simplified into multiple 2-D inversion problem because of the large number of sensors along the perimeter (Figure 7.8(a)). In the measurements, the domain is  $100\text{cm} \times 10\text{cm}$ . There are  $M=100$  measurements (1 measurement per cm) and  $N=1000$  unknowns (voxel dimension  $1\text{cm} \times 1\text{cm}$ ). The number of unknowns is much greater than the number of measurements. While a larger voxel size

reduces the number of unknowns, it also causes a decrease in resolution. Therefore, we adopt parametric representation to reduce the number of unknowns and use successive forward simulations to solve parameters. The space distribution of magnetic inclusions along the annulus can be represented by a rectangle  $r \times h$  at position  $z$  (Figure 7.8(b)-inset).

The procedures for successive forward simulation is as follows (Santamarina and Fratta, 2005):

1. Generate an estimate of the solution  $x^{<est>}$ .
2. Use forward simulation to compute  $y^{<pred>} = f(x^{<est>})$
3. Determine the residual between  $y^{<pred>}$  and  $y^{<meas>}$ .
4. Generate another estimate and repeat.
5. Continue until a physically meaningful estimate is found that adequately justifies the data.

#### Forward simulation

The magnetic field of a magnetic dipole is (Figure 7.9(a)):

$$B_z(r) = \frac{\mu_0}{4\pi} m_l \left( \frac{3\cos^2 \theta - 1}{r^3} \right) \quad (7.3)$$

$$B_x(r) = \frac{\mu_0}{4\pi} m_l \left( \frac{3\cos \theta \sin \theta}{r^3} \right) \quad (7.4)$$

where  $m_l$  is the magnetic strength of the dipole. Based on this equation, we are able to calculate the response map. Figure 7.9(b) shows the response of a directional magnetic sensor to a magnetic dipole at position  $(x, y)$ . Similar to electric fields, the superposition

principle applies to magnetic fields and causes the total field strength equals to vector sum of multiple individual fields due to the magnets:

$$\mathbf{B}_{total} = \mathbf{B}_1 + \mathbf{B}_2 + \mathbf{B}_3 + \dots + \mathbf{B}_n \quad (7.5)$$

Therefore, a big irregular magnetic inclusion can be treated as the superposition of multiple small magnetic dipoles.

### Residuals

We apply forward simulation for three parameters  $h$ ,  $z$ , and  $r$  and then calculate the residuals between simulations and measurements with the  $L_2$  error norm.

$$S = \sum_{i=1}^n (y_i - f(x_i))^2 \quad (7.6)$$

Figure 7.8(b) presents the determination of a magnetic inclusion with  $z=18$ ,  $r=22$ , and  $h=3$ . The residuals show that thickness  $h$  and position  $z$  can be accurately determined since a clear peak value can be expected. However, the length  $r$  decays smoothly with the distance from the wellbore which makes it is difficult to accurately estimate the value of  $r$  accurately.

### Experimental study

The eccentric casing model is filled with clean sand and the sand-iron mixture (10% iron particle) to simulate the mud channel in the narrow side (Figure 7.10(a)). Figure 7.10(b) shows the raw measurement results obtained from 12 directions in a cylindrical coordinate system. We are able to roughly see the spatial distribution of magnetic materials from the raw data. The inverse algorithm is applied after filtering signals below a certain amplitude

to improve the signal-to-noise ratio. Figure 7.10(c) illustrates the inversion of raw measurement data to solve the spatial distribution of the magnetic materials.

Figure 7.11 shows the measurement results of a thin layer sand-iron mixture in the concentric cased borehole model. This experiment reveals the spatial resolution of the new logging tool. It is able to accurately capture magnetic fields generated by layer magnetic material with only 3mm thickness.

## **7.7 Conclusions**

Innovative well completion logging techniques are needed for the assessment of cement job quality. This chapter explored a well logging method that consists of high-resolution magnetic sensors, non-magnetic casings, and engineered magnetic mud.

The shield effect of different metallic materials is investigated numerically and experimentally. Results indicate that stainless steel casings have a negligible influence on the magnetic field behind the casing while the iron casing completely shields the magnetic field.

The magnetization status is critical to the magnetic field distribution of a fracture. The central-symmetric feature of the field strength distribution along the main axis provides a noticeable signal to accurately determine the location of a fracture. However, the evaluation of the fracture size remains a challenge.

The multi-sensor probe provides a high-resolution 3-D measurement of the magnetic field strength of cased boreholes. An efficient inverse algorithm successfully solves the spatial distribution of magnetic materials in the annulus.

Table 7.1. Sensitivity of different magnetic sensors. The orange and blue bands indicate the strength of the bio's magnetic field and the Earth's magnetic field.

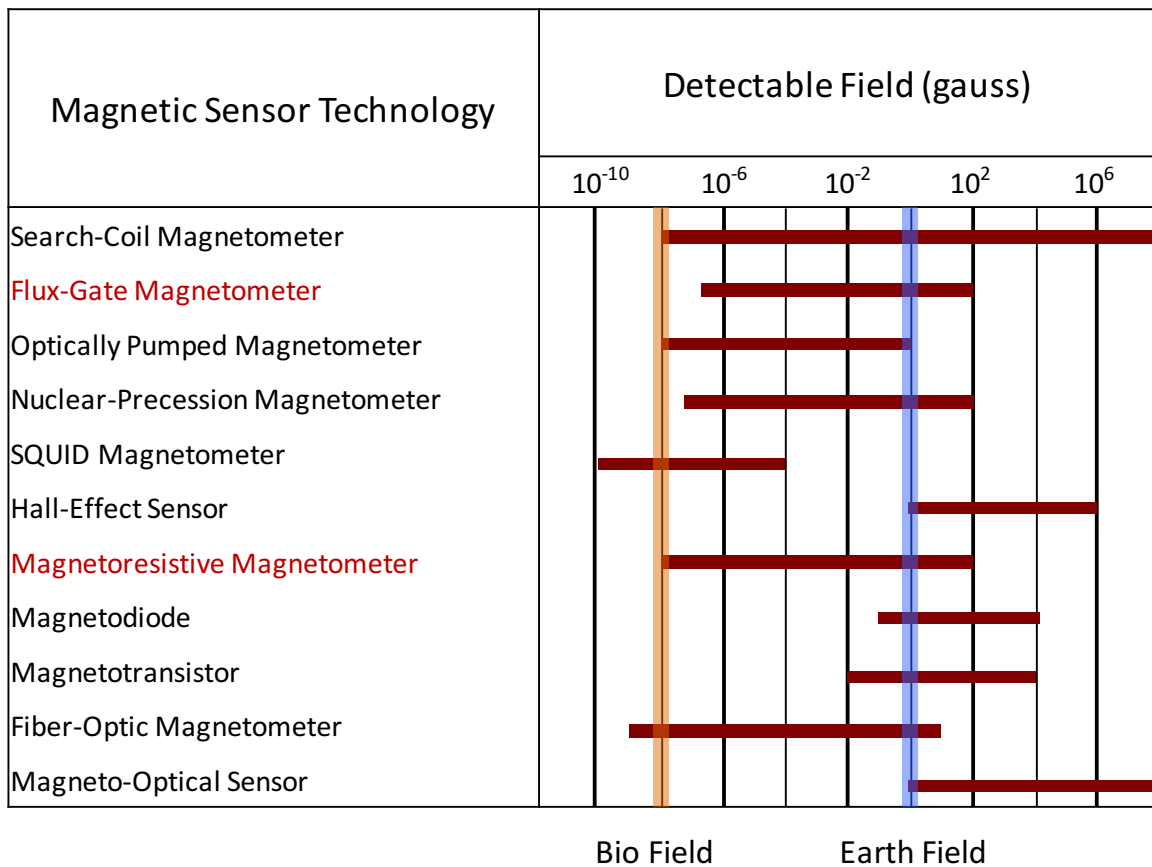


Table 7.2. Relative permeability of common materials

<b>Medium</b>	<b>Relative permeability</b>
Iron (99.95% pure)	1,000,000
Iron (99.8% pure)	5,000
Ferritic SS	1,400
Martensitic SS	850
<b>Austenitic SS</b>	<b>1.004</b>
Air	1.00000037
Superconductors	0



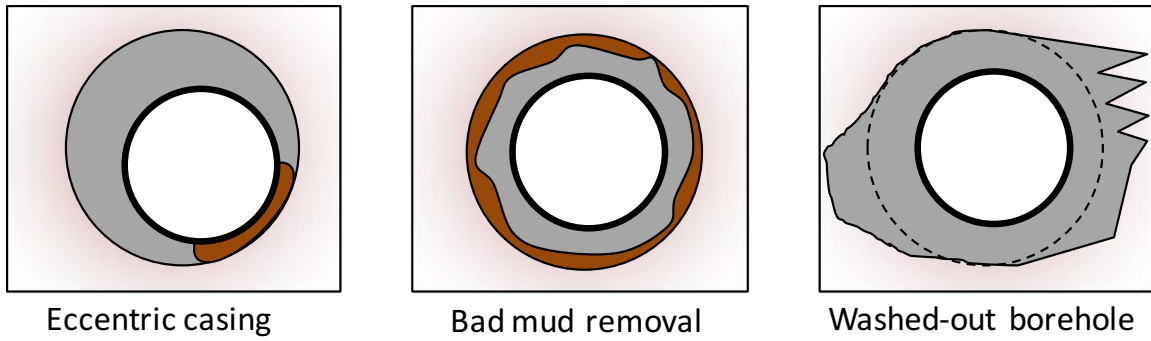


Figure 7.1. Potential events result from poor cement jobs.

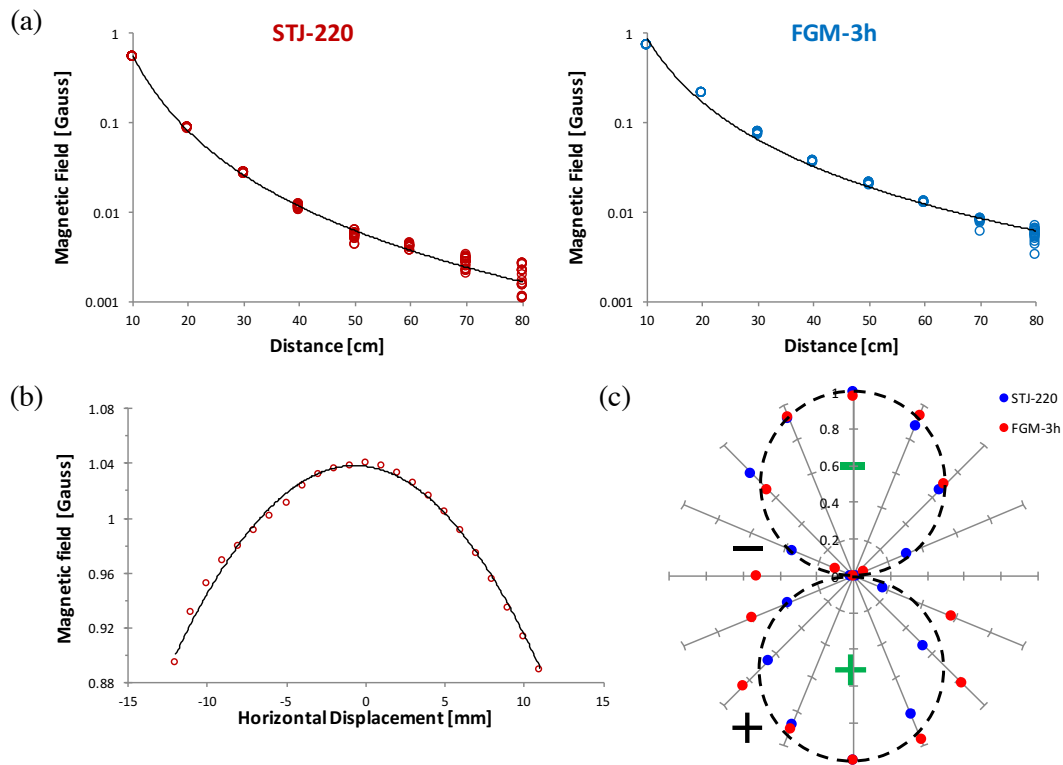
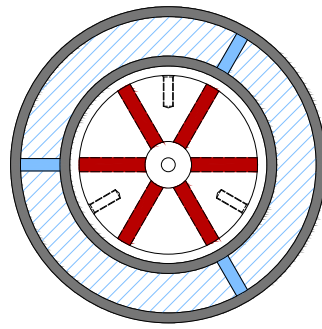
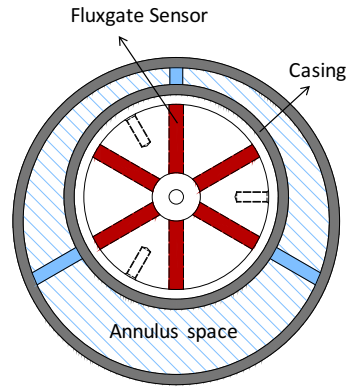


Figure 7.2. Sensitivity of fluxgate and magnetic tunnel junction. (a) Along the main axis. (b) Transverse to the main axis. (c) Directivity.



Eccentric casing



Concentric casing

Figure 7.3. The multi-sensor probe.

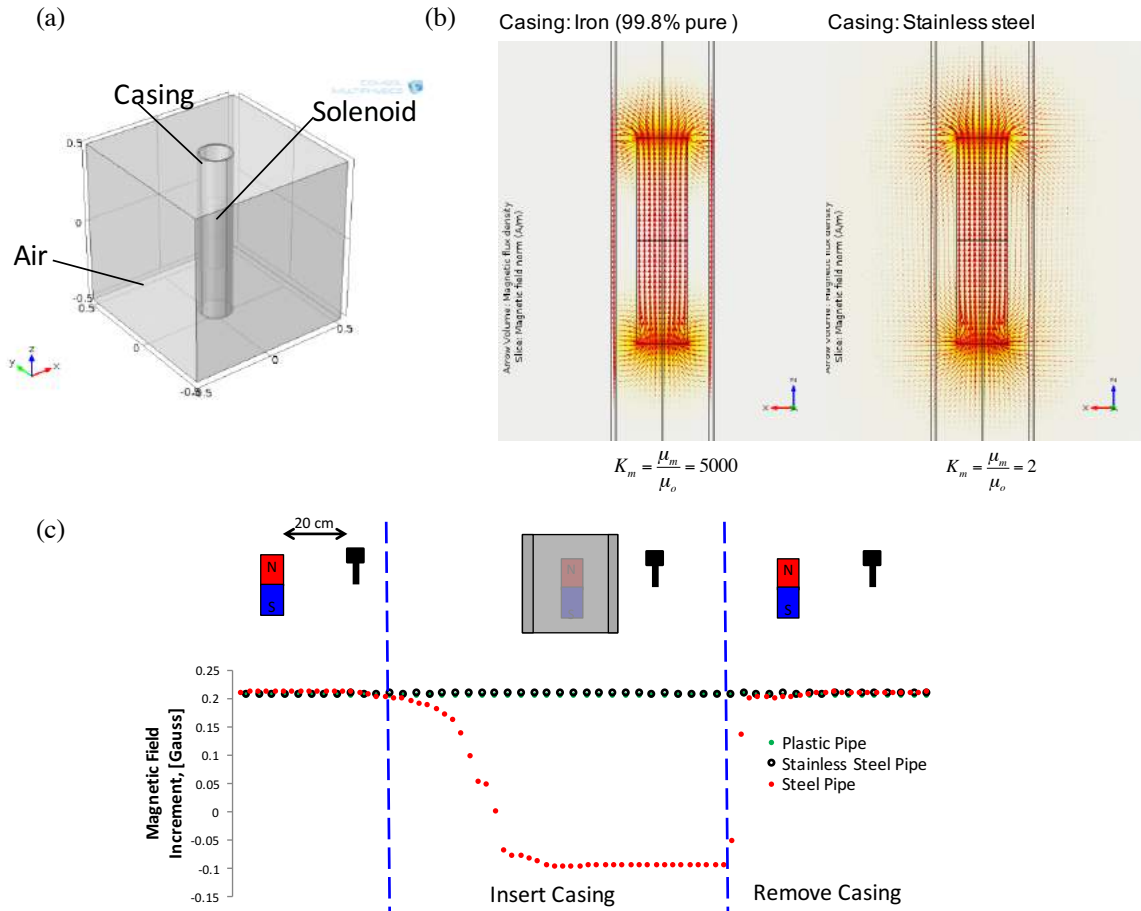


Figure 7.4. Shield effect. (a) 3-D modeling of the shield effect of a casing. (b) Numerical simulation: the influence of casing material on the projection of the magnetic field generated by a solenoid. The iron casing completely shields the internal magnetic field. The stainless steel casing has a negligible influence. (c) Lab experiments.

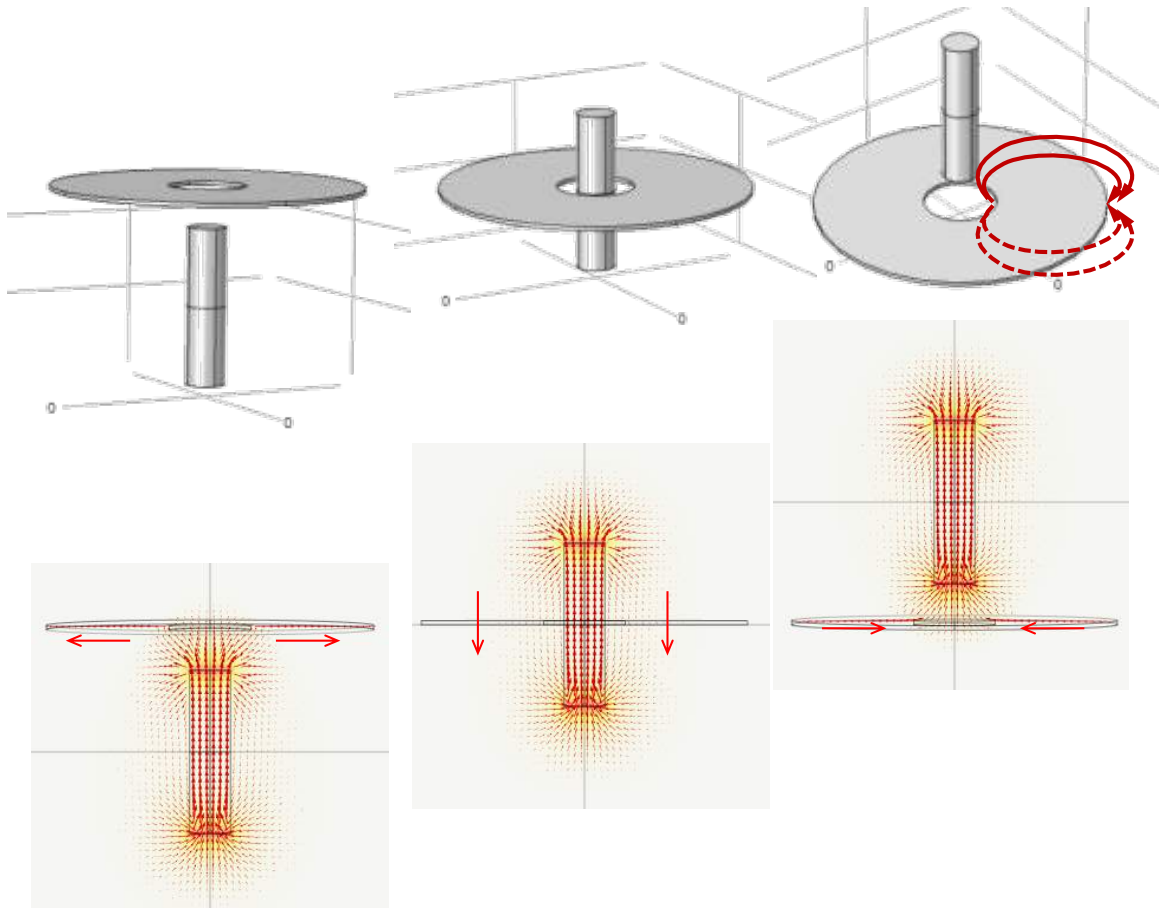


Figure 7.5. Magnetization of a fracture filled with a ferromagnetic tracer. From left to right: a permanent magnet travels upward through the fracture.

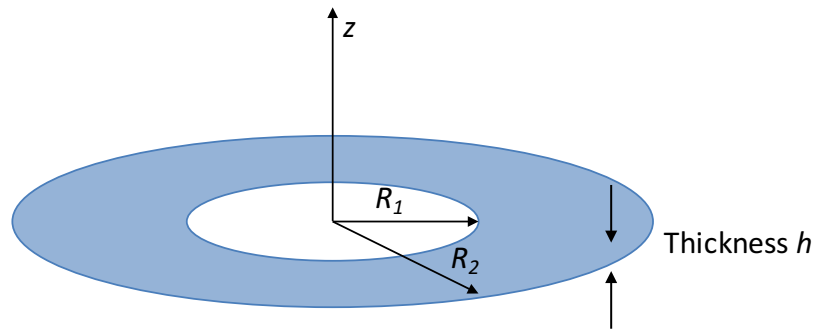


Figure 7.6. Geometric definition of a fracture.

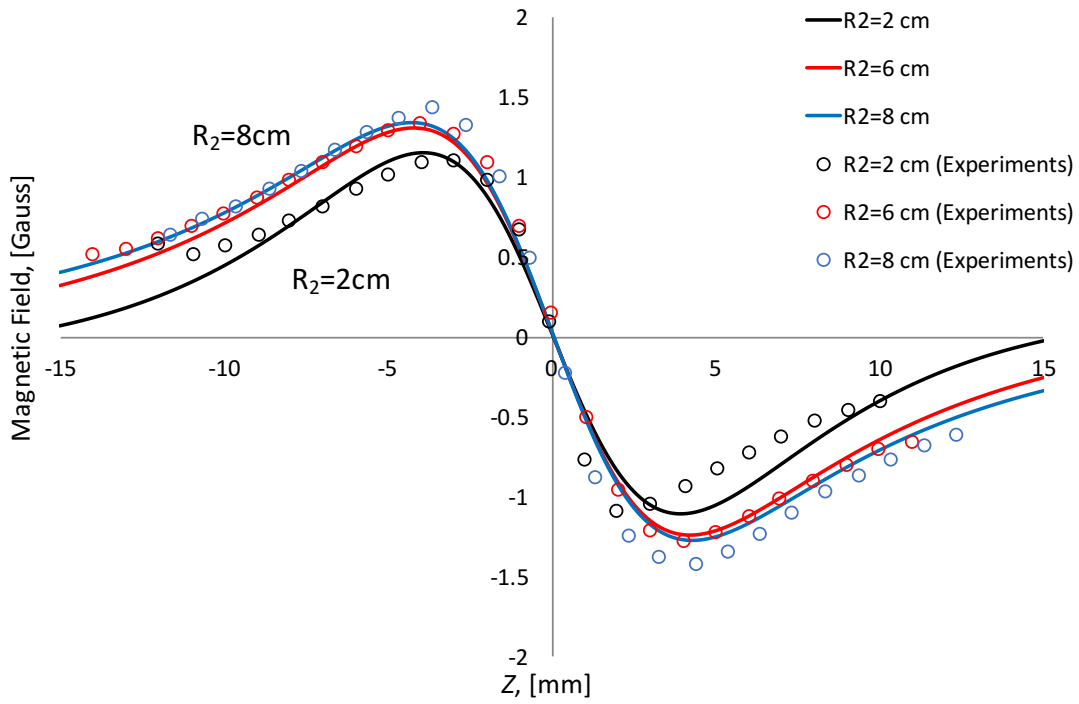


Figure 7.7. Magnetic field strength along the center axis of fractures access a well of varying radius  $R_2$ . Solid lines are analytical solutions and dots are experimental results.

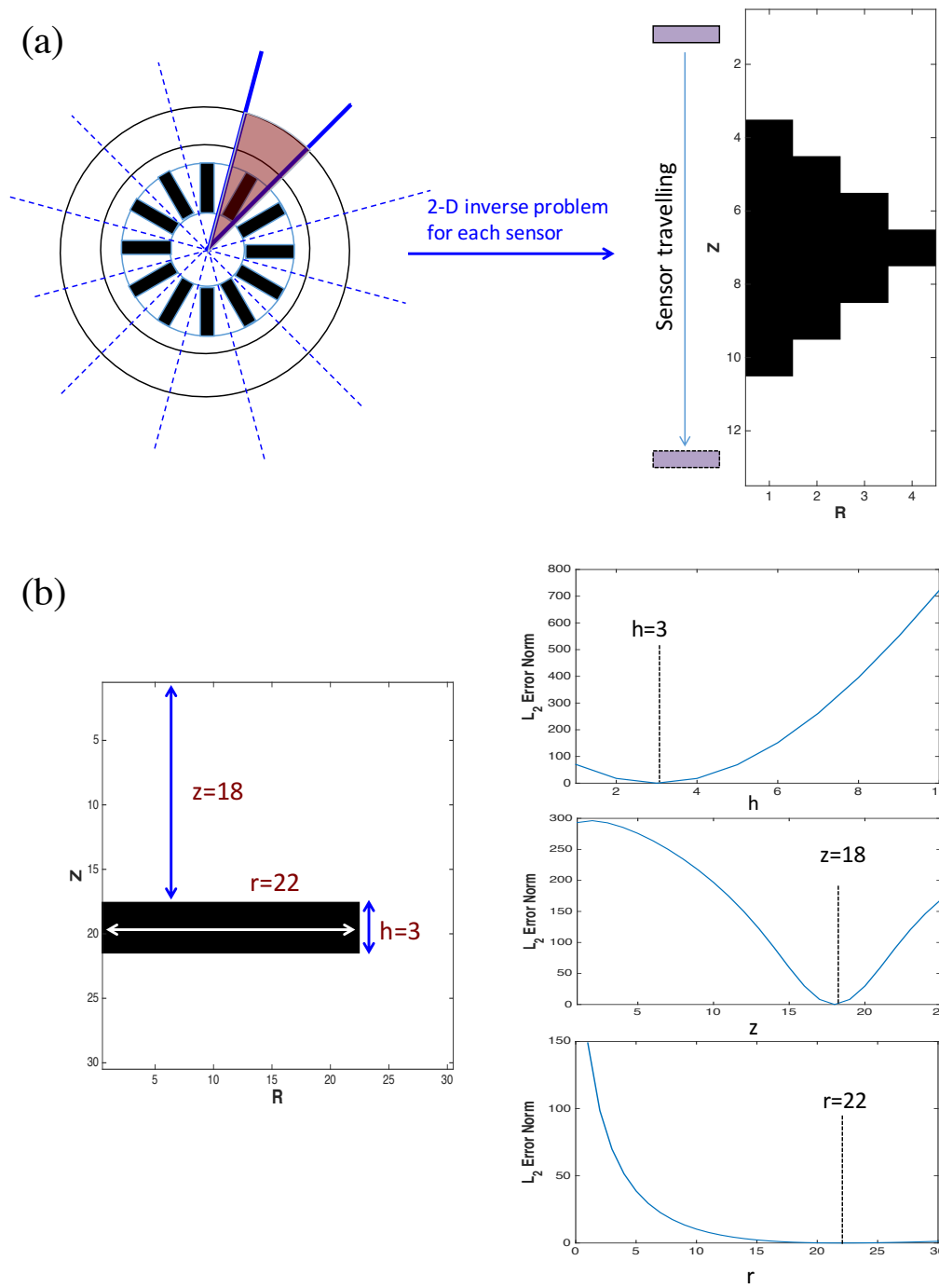


Figure 7.8. Inverse solution. (a) 3D-2D simplification. (b) Residuals determined with  $L_2$  error norm.

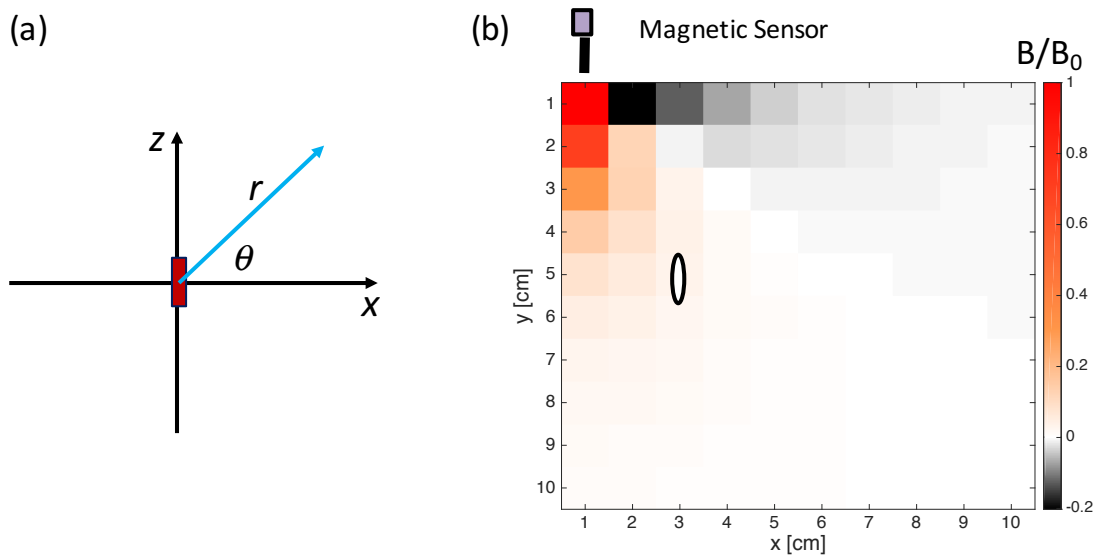


Figure 7.9. Magnetic field strength of a dipole. (a) Coordinate system. (b) Response map.

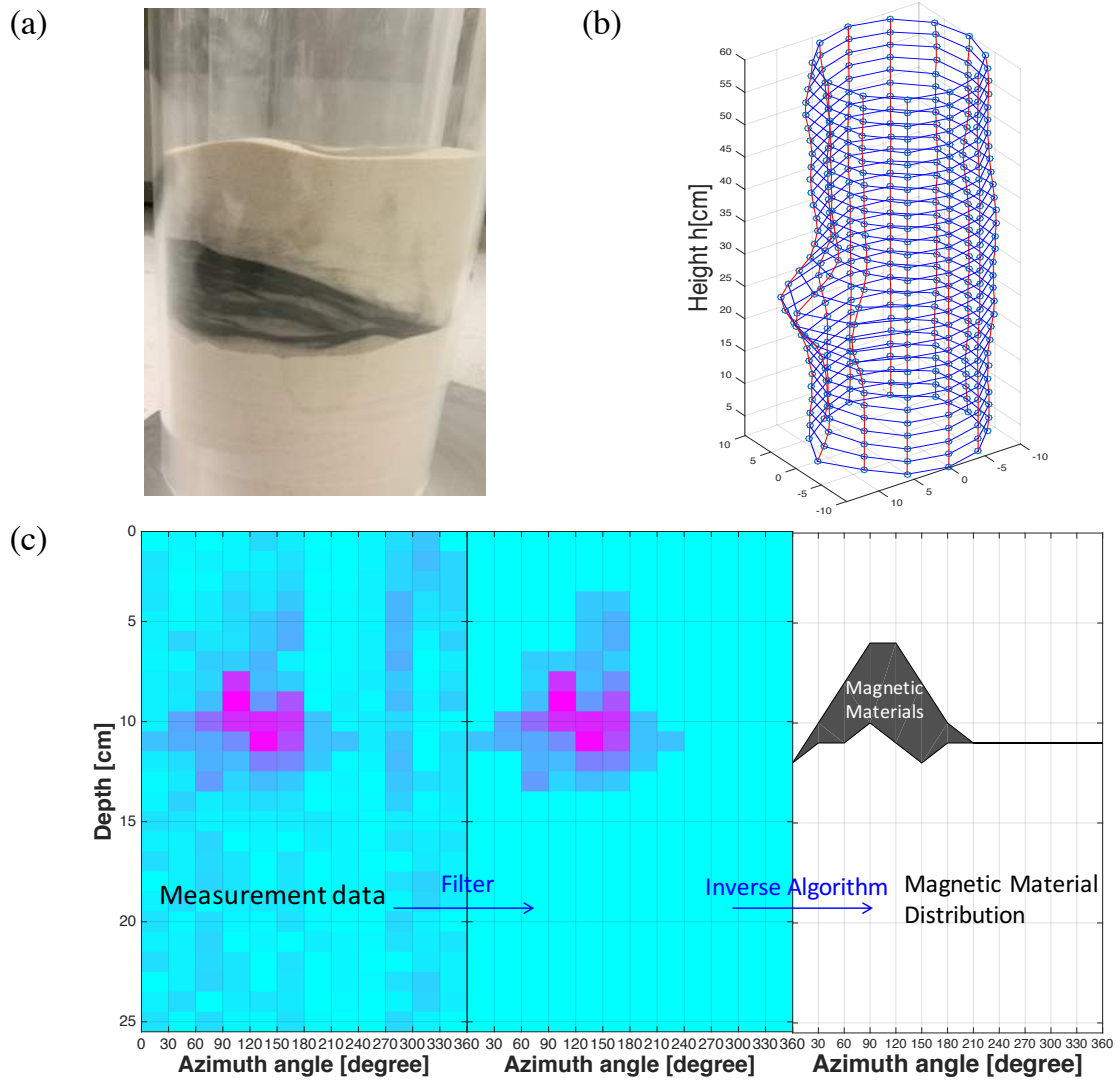


Figure 7.10. Magnetic logging of an asymmetric accumulation. (a) Model and magnetic material distribution. (b) Raw data. (c) Inversion of raw data to determine the spatial distribution of the magnetic material.



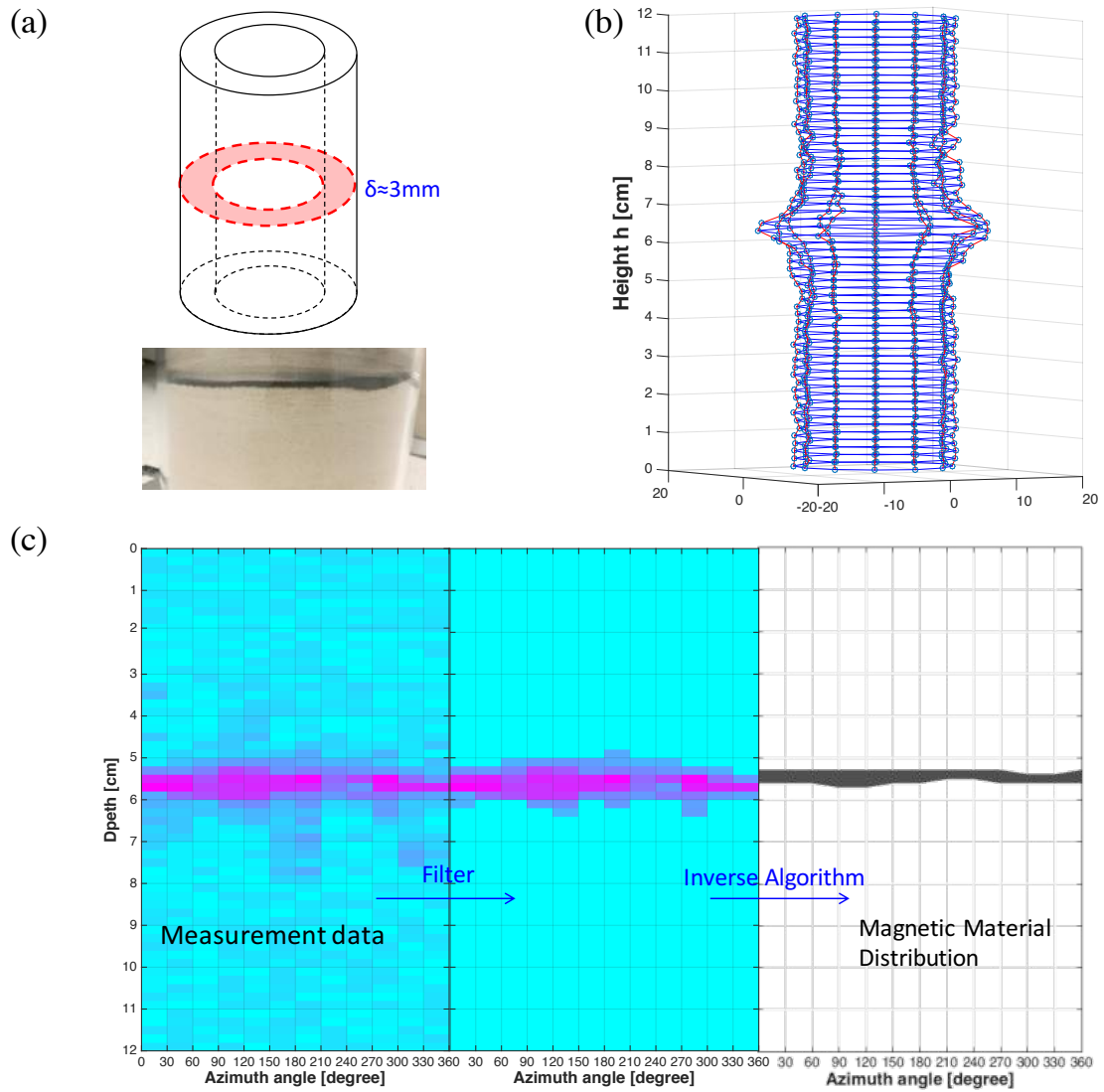


Figure 7.11. Magnetic logging of a thin fracture. (a) Model and magnetic material distribution. (b) Raw data. (c) Inversion of raw measurement data to determine the spatial distribution of the magnetic material.

## CHAPTER 8. CONCLUSIONS

Particle-laden fluids are pervasive in the oil and gas industry during drilling and production. Examples include drilling fluids, fracturing fluids, and migrating fines in the reservoir formation. Particle species include nanoparticle, clay mineral, and fines, with particle size spanning from nanometer to millimeter. Particles may interact among themselves, with other particles, the porous medium, and the liquid-fluid interface.

The purposes of this research were to enhance the fundamental understanding of particle-laden fluids and to explore their engineering applications. The main conclusions from this research follow.

### Nanoparticle-coated interface

- The nanoparticle-coated interface undergoes a transition from fluid-like to shell-like with the increases in surface coverage. Further compression of the closely packed particles results in the buckling of the particle-coated interface.
- The particle-coated interface exhibits an asymmetric, curvature-dependent mechanical behavior.
- The slip and no-slip boundary conditions lead to distinct buckling and crumpling patterns. In addition, the initial surface coverage manipulates the number of depressions during buckling.
- The nanoparticle-coated interface has a wide impact on immiscible displacement, e.g. capillary pressure across a pore throat and viscous fingering.

### Nanoparticle transport in porous media

- The zeta potential of silica is pH dependent; however, the zeta potential of carbonate is determined by other PDIs, e.g.  $\text{Ca}^{2+}$ ,  $\text{Mg}^{2+}$  and  $\text{CO}_3^{2-}$  rather than the pH.
- The reduction of the surface potential and the increase in ionic concentration inhibit the electrostatic double layer repulsion and lower the energy barrier for adsorption.
- Alkaline and low salinity conditions (especially PDIs) favor nanoparticles transport in carbonate reservoirs.
- A high adsorption tendency increases the equilibrium adsorption constant and the multi-layer adsorption increases the kinetic adsorption rate.

#### Fines migration in porous media

- Non-buoyant glass particles experience retardation due to gravity and inertial effects. The large local volume fraction of particles promotes the formation of a multi-grain particulate arch at constrictions.
- Quasi-neutrally-buoyant latex particles interact with the PDMS walls by direct interception. The capture of latex particles by PDMS walls and further aggregates of latex particles at constrictions reduce the constriction size and eventually plug pore constrictions.
- High flow rates inhibit the formation of clogging of glass particles, but promote the clogging of latex particles.
- The higher occurring probability of dependent clogging leads to the localized clogging patterns. The dependent clogging is dominant for the clogging of glass

particles, while it has a limited influence on the clogging of latex particles in PDMS microfluidic chips.

#### Filtration: mudcake growth

- Wide stress-range constitutive models are adopted to avoid numerical discontinuities.
- Environmental factors such as temperature, pH, ionic concentration and cation contamination have a significant influence on cake formation.
- Long filtration time, high permeability, and low viscosity exacerbate fluid loss and increase the cake thickness.
- Mud removal: effective stress dependent mudcake formation and the time-dependent mud thixotropy. Thixotropy dominates the mud yield stress at high void ratios, e.g.  $e > 20$ .
- Stuck pipe: the offsetting force increases sub-linearly as a power function.

#### Magnetic mud

- Low-cost magnetic mud developed in this research uses micro-size  $\text{Fe}_3\text{O}_4$  particles to magnetize the bentonite suspension and surfactants to stabilize the suspension.
- The anionic surfactant SDS is most effective at improving the suspension stability as compared to the other surfactants (Tween 20, CTAB). The optimal SDS concentration is between 4~8mM which is close to its critical micelle concentration.

- The magnetic drilling mud shows typical ferromagnetic behavior. The saturation and residual magnetization are proportional to the concentration of  $\text{Fe}_3\text{O}_4$  particles.

#### Magnetic tool

- This study develops a well logging method which consists of high-resolution magnetic sensors, non-magnetic casings, and magnetic mud.
- A stainless steel casing has a negligible shield effect on the magnetic field.
- Radially magnetized fractures provide a noticeable signal to accurately determine the location of fractures. However, the evaluation of the fracture size remains a challenge.
- The multi-sensor torpedo provides a high-resolution 3-D measurement of the magnetic field strength of cased boreholes. An efficient inverse algorithm successfully solves the spatial distribution of magnetic materials.

## REFERENCES

- Abend, S. and G. Lagaly (2000). "Sol–gel transitions of sodium montmorillonite dispersions." *Applied Clay Science* 16(3): 201-227.
- Abkarian, M., Subramaniam, A. B., Kim, S. H., Larsen, R. J., Yang, S. M., & Stone, H. A. (2007). Dissolution arrest and stability of particle-covered bubbles. *Physical review letters*, 99(18), 188301.
- Abu-Jdayil, B., Ghannam, M., & Nasser, M. S. (2016). The Modification of Rheological Properties of Bentonite-Water Dispersions with Cationic and Anionic Surfactants. *International Journal of Chemical Engineering and Applications*, 7(2), 75.
- Adamczyk, Z. (2003). Particle adsorption and deposition: role of electrostatic interactions. *Advances in Colloid and Interface Science*, 100, 267-347.
- Aderibigbe, A., Cheng, K., Heidari, Z., Killough, J., & Fuss-Dezelic, T. (2016). Application of magnetic nanoparticles mixed with propping agents in enhancing near-wellbore fracture detection. *Journal of Petroleum Science and Engineering*, 141, 133–143.
- Adler, E., Reppel, G. W., Rodewald, W., & Warlimont, H. (1990). Matching P/M and the physics of magnetic materials. *ChemInform*, 21(16).
- Aitchison, G. D., & Wood, C. C. (1965). Some interactions of compaction, permeability and post-construct ion deflocculation affecting the probability of piping failure in small earth dams.
- Al Mahrouqi, D., Vinogradov, J., & Jackson, M. D. (2016). Zeta potential of artificial and natural calcite in aqueous solution. *Advances in colloid and interface science*.
- Al-Anssari, S., Barifcani, A., Wang, S., & Iglauer, S. (2016). Wettability alteration of oil-wet carbonate by silica nanofluid. *Journal of colloid and interface science*, 461, 435-442.
- Alderman, N., A. Gavignet, D. Guillot and G. Maitland (1988). High-temperature, high-pressure rheology of water-based muds. SPE Annual Technical Conference and Exhibition, Society of Petroleum Engineers.
- An, C., Yan, B., Alfi, M., Mi, L., Killough, J. E., & Heidari, Z. (2017). Estimating spatial distribution of natural fractures by changing NMR T2 relaxation with magnetic nanoparticles. *Journal of Petroleum Science and Engineering*, 157, 273–287.
- Annis, M. and P. Monaghan (1962). "Differential pressure sticking-laboratory studies of friction between steel and mud filter cake." *Journal of Petroleum Technology* 14(05): 537-543.

- Annis, M. R. (1967). "High-temperature flow properties of water-base drilling fluids." *Journal of Petroleum Technology* 19(08): 1,074-071,080.
- Arthur, K. and J. Peden (1988). The evaluation of drilling fluid filter cake properties and their influence on fluid loss. International Meeting on Petroleum Engineering, Society of Petroleum Engineers.
- Asekomhe, S. O., Chiang, R., Masliyah, J. H., & Elliott, J. A. (2005). Some observations on the contraction behavior of a water-in-oil drop with attached solids. *Industrial & engineering chemistry research*, 44(5), 1241-1249.
- Aumaitre, E., Vella, D., & Cicuti, P. (2011). On the measurement of the surface pressure in Langmuir films with finite shear elasticity. *Soft Matter*, 7(6), 2530-2537.
- Aussillous, P., & Quéré, D. (2001). Liquid marbles. *Nature*, 411(6840), 924-927.
- Ayatollahi, S., & Zerafat, M. M. (2012, January). Nanotechnology-assisted EOR techniques: New solutions to old challenges. In SPE International Oilfield Nanotechnology Conference and Exhibition. Society of Petroleum Engineers.
- Bacchin, P., Derekx, Q., Veyret, D., Glucina, K., & Moulin, P. (2014). Clogging of microporous channels networks: Role of connectivity and tortuosity. *Microfluidics and Nanofluidics*, 17(1), 85–96. <https://doi.org/10.1007/s10404-013-1288-4>
- Bateman, R. M. (2016). *Cased-hole log analysis and reservoir performance monitoring*. Springer.
- Berhanu, M., & Kudroli, A. (2010). Heterogeneous structure of granular aggregates with capillary interactions. *Physical review letters*, 105(9), 098002.
- Bhattacharjee, S., & Elimelech, M. (1997). Surface element integration: a novel technique for evaluation of DLVO interaction between a particle and a flat plate. *Journal of colloid and interface science*, 193(2), 273-285.
- Binks, B. P. (2002). Particles as surfactants—similarities and differences. *Current Opinion in Colloid & Interface Science*, 7(1–2), 21–41.
- Binks, B. P., & Murakami, R. (2006). Phase inversion of particle-stabilized materials from foams to dry water. *Nature materials*, 5(11), 865-869.
- Bleam, W. F. (1990). The nature of cation-substitution sites in phyllosilicates. *Clays Clay Miner*, 38, 527–536.
- Böker, A., He, J., Emrick, T., & Russell, T. P. (2007). Self-assembly of nanoparticles at interfaces. *Soft matter*, 3(10), 1231-1248.
- Bonett, A. and D. Pafitis (1996). "Getting to the root of gas migration." *Oilfield Review* 8(1): 36-49.

- Bordács, S., Agod, A., & Hórvölgyi, Z. (2006). Compression of Langmuir films composed of fine particles: collapse mechanism and wettability. *Langmuir*, 22(16), 6944-6950.
- Boyce, J. I., Reinhardt, E. G., Raban, A., & Pozza, M. R. (2004). Marine magnetic survey of a submerged Roman harbour, Caesarea Maritima, Israel. *International Journal of Nautical Archaeology*, 33(1), 122–136.
- Bresme, F., & Oettel, M. (2007). Nanoparticles at fluid interfaces. *Journal of Physics: Condensed Matter*, 19(41), 413101.
- Broding, R. A., Zimmerman, C. W., Somers, E. V, Wilhelm, E. S., & Stripling, A. A. (1952). Magnetic well logging. *Geophysics*, 17(1), 1–26.
- Caenn, R., Darley, H. C. H., & Gray, G. R. (2011). *Composition and properties of drilling and completion fluids*. Gulf professional publishing.
- Cameron, D. R., & Klute, A. (1977). Convective-dispersive solute transport with a combined equilibrium and kinetic adsorption model. *Water Resources Research*, 13(1), 183-188.
- Carman, P. C. (1937). "Fluid flow through granular beds." *Transactions-Institution of Chemical Engineeres* 15: 150-166.
- Carrier, W. and J. Beckman (1984). "Correlations between index tests and the properties of remoulded clays." *Geotechnique* 34(2): 211-228.
- Cejas, C. M., Monti, F., Truchet, M., Burnouf, J.-P., & Tabeling, P. (2017). Particle deposition kinetics of colloidal suspensions in microchannels at high ionic strength. *Langmuir*, 33(26), 6471–6480.
- Chang, F.-R. C., & Sposito, G. (1996). The electrical double layer of a disk-shaped clay mineral particle: Effects of electrolyte properties and surface charge density. *Journal of Colloid and Interface Science*, 178(2), 555–564.
- Chapuis, R. P., & Aubertin, M. (2003). On the use of the Kozeny Carman equation to predict the hydraulic conductivity of soils. *Canadian Geotechnical Journal*, 40(3), 616-628.
- Chen, L., Zhou, C. H., Fiore, S., Tong, D. S., Zhang, H., Li, C. S., ... Yu, W. H. (2016). Functional magnetic nanoparticle/clay mineral nanocomposites: preparation, magnetism and versatile applications. *Applied Clay Science*, 127, 143–163.
- Chenevert, M. and J. Dewan (2001). "A model for filtration of water-base mud during drilling: determination of mudcake parameters." *Petrophysics* 42(03).
- Chevalier, Y., & Bolzinger, M. A. (2013). Emulsions stabilized with solid nanoparticles: Pickering emulsions. *Colloids and Surfaces A: Physicochemical and Engineering Aspects*, 439, 23-34.



- Chong, S.-H. and J. C. Santamarina (2016). "Soil Compressibility Models for a Wide Stress Range." *Journal of Geotechnical and Geoenvironmental Engineering* 142(6): 06016003.
- Cicuta, P., & Vella, D. (2009). Granular character of particle rafts. *Physical review letters*, 102(13), 138302.
- Cicuta, P., Stancik, E. J., & Fuller, G. G. (2003). Shearing or compressing a soft glass in 2D: time-concentration superposition. *Physical review letters*, 90(23), 236101.
- Cook, J., Growcock, F., Guo, Q., Hodder, M., & van Oort, E. (2011). Stabilizing the wellbore to prevent lost circulation. *Oilfield Review*, 23(4), 26–35.
- Cooke Jr, C. E. (1979). Radial Differential Temperature (RDT) Logging-A New Tool for Detecting and Treating Flow Behind Casing. *Journal of Petroleum Technology*, 31(6), 676–682.
- Cundy, A. B., Hopkinson, L., & Whitby, R. L. (2008). Use of iron-based technologies in contaminated land and groundwater remediation: a review. *Science of the total environment*, 400(1), 42-51.
- Dasgupta, S., Auth, T., & Gompper, G. (2017). Nano-and microparticles at fluid and biological interfaces. *Journal of Physics: Condensed Matter*, 29(37), 373003.
- Datta, S. S., Shum, H. C., & Weitz, D. A. (2010). Controlled buckling and crumpling of nanoparticle-coated droplets. *Langmuir*, 26(24), 18612-18616.
- Deák, A., Hild, E., Kovács, A. L., & Hórvölgyi, Z. (2007). Contact angle determination of nanoparticles: film balance and scanning angle reflectometry studies. *Physical Chemistry Chemical Physics*, 9(48), 6359-6370.
- Dehghan Monfared, A., Ghazanfari, M. H., Jamialahmadi, M., & Helalizadeh, A. (2016). Potential Application of Silica Nanoparticles for Wettability Alteration of Oil–Wet Calcite: A Mechanistic Study. *Energy & Fuels*, 30(5), 3947-3961.
- Derganc, J., Antonny, B., & Čopič, A. (2013). Membrane bending: the power of protein imbalance. *Trends in biochemical sciences*, 38(11), 576-584.
- Deshmukh, O. S., van den Ende, D., Stuart, M. C., Mugele, F., & Duits, M. H. (2015). Hard and soft colloids at fluid interfaces: Adsorption, interactions, assembly & rheology. *Advances in colloid and interface science*, 222, 215-227.
- Dominik, C., & Tielens, A. G. G. M. (1995). Resistance to rolling in the adhesive contact of two elastic spheres. *Philosophical Magazine A*, 72(3), 783-803.
- Donovan, T. J., Forgey, R. L., & Roberts, A. A. (1979). Aeromagnetic Detection of Diagenetic Magnetite over Oil Fields: GEOLOGIC NOTES. *AAPG Bulletin*, 63(2), 245–248.

- Dressaire, E., & Sauret, A. (2017). Clogging of microfluidic systems. *Soft Matter*, 13(1), 37–48.
- Du, K., Glogowski, E., Emrick, T., Russell, T. P., & Dinsmore, A. D. (2010). Adsorption energy of nano-and microparticles at liquid– liquid interfaces. *Langmuir*, 26(15), 12518-12522.
- Dunphy Guzman, K. A., Finnegan, M. P., & Banfield, J. F. (2006). Influence of surface potential on aggregation and transport of titania nanoparticles. *Environmental Science & Technology*, 40(24), 7688-7693.
- Dupriest, F. E., W. C. Elks and S. Ottesen (2011). "Design Methodology and Operational Practices Eliminate Differential Sticking." *SPE Drilling & Completion* 26(01): 115-123.
- El Mohtar, C. and J. Yoon (2013). "Disturbance effect on time-dependent yield stress measurement of bentonite suspensions." *Geotechnical Testing Journal*, Vol. 36, No. 1, 2013, pp. 78-87
- Elimelech, M., & O'Melia, C. R. (1990). Effect of electrolyte type on the electrophoretic mobility of polystyrene latex colloids. *Colloids and Surfaces*, 44, 165-178.
- Elimelech, M., Gregory, J., & Jia, X. (2013). Particle deposition and aggregation: measurement, modelling and simulation. Butterworth-Heinemann.
- Elkatatny, S., M. A. Mahmoud and H. A. Nasr-El-Din (2012). "Characterization of filter cake generated by water-based drilling fluids using CT scan." *SPE Drilling & Completion* 27(02): 282-293.
- Esfandiyari Bayat, A., Junin, R., Samsuri, A., Piroozian, A., & Hokmabadi, M. (2014). Impact of metal oxide nanoparticles on enhanced oil recovery from limestone media at several temperatures. *Energy & Fuels*, 28(10), 6255-6266.
- Espinosa-Gayosso, A., Ghisalberti, M., Ivey, G. N., & Jones, N. L. (2012). Particle capture and low-Reynolds-number flow around a circular cylinder. *Journal of Fluid Mechanics*, 710, 362–378.
- Ferdous, S., Ioannidis, M. A., & Henneke, D. (2011). Adsorption kinetics of alkanethiol-capped gold nanoparticles at the hexane–water interface. *Journal of Nanoparticle Research*, 13(12), 6579-6589.
- Feynman, R. P., Leighton, R. B., & Sands, M. (1979). *The Feynman lectures on physics, vol. 2: Mainly electromagnetism and matter*. Addison-Wesley.
- Flagg, A. H., Myers, J. P., Campbell, J. L. P., Terry, J. M., & Mardock, E. S. (1955). Radioactive tracers in oil production problems.
- Frelichowska, J., Bolzinger, M. A., Valour, J. P., Mouaziz, H., Pelletier, J., & Chevalier,

- Y. (2009). Pickering w/o emulsions: drug release and topical delivery. *International Journal of Pharmaceutics*, 368(1), 7-15.
- Friedlander, S. K. (1967). Particle diffusion in low-speed flows. *Journal of Colloid and Interface Science*, 23(2), 157–164.
- Fu, F., Dionysiou, D. D., & Liu, H. (2014). The use of zero-valent iron for groundwater remediation and wastewater treatment: a review. *Journal of hazardous materials*, 267, 194-205.
- Gadeke, L. L., Gartner, M. L., Sharbak, D. E., & Wyatt, D. F. (1991). The Interpretation of Radioactive-Tracer Logs Using Gamma-Ray Spectroscopy Measurements. *The Log Analyst*, 32(1).
- Gai, Y., Kim, M., Pan, M., & Tang, S. K. (2017). Amphiphilic nanoparticles suppress droplet break-up in a concentrated emulsion flowing through a narrow constriction. *Biomicrofluidics*, 11(3), 034117.
- Gao, S., Moran, K., Xu, Z., & Masliyah, J. (2009). Role of bitumen components in stabilizing water-in-diluted oil emulsions. *Energy & Fuels*, 23(5), 2606-2612.
- Garcimartín, A., Zuriguel, I., Pagnaloni, L. A., & Janda, A. (2010). Shape of jamming arches in two-dimensional deposits of granular materials. *Physical Review E*, 82(3), 031306.
- Gooneratne, C. P., Li, B., & Moellendick, T. E. (2017). Downhole Applications of Magnetic Sensors. *Sensors*, 17(10), 2384.
- Gudipaty, T., Stamm, M. T., Cheung, L. S. L., Jiang, L., & Zohar, Y. (2011). Cluster formation and growth in microchannel flow of dilute particle suspensions. *Microfluidics and Nanofluidics*, 10(3), 661–669.
- Guillot, D., & Nelson, E. (2006). Well Cementing. *Schlumberger Educational Services, Sugar Land Google Scholar*.
- Guo, D., Xie, G., & Luo, J. (2013). Mechanical properties of nanoparticles: basics and applications. *Journal of physics D: applied physics*, 47(1), 013001.
- Hartmann, A., M. Özerler, C. Marx and H.-J. Neumann (1988). "Analysis of mudcake structures formed under simulated borehole conditions." *SPE drilling engineering* 3(04): 395-402.
- He, L., Lin, F., Li, X., Sui, H., & Xu, Z. (2015). Interfacial sciences in unconventional petroleum production: from fundamentals to applications. *Chemical Society Reviews*, 44(15), 5446-5494.
- Heim, L. O., Blum, J., Preuss, M., & Butt, H. J. (1999). Adhesion and friction forces between spherical micrometer-sized particles. *Physical Review Letters*, 83(16), 3328.

- Hendraningrat, L., Li, S., & Torsæter, O. (2013). A coreflood investigation of nanofluid enhanced oil recovery. *Journal of Petroleum Science and Engineering*, 111, 128-138.
- Holdich, R. (1993). "Prediction of solid concentration and height in a compressible filter cake." *International journal of mineral processing* 39(3): 157-171.
- Holtzman, R., & Segre, E. (2015). Wettability stabilizes fluid invasion into porous media via nonlocal, cooperative pore filling. *Physical review letters*, 115(16), 164501.
- Horozov, T. S., Binks, B. P., Aveyard, R., & Clint, J. H. (2006). Effect of particle hydrophobicity on the formation and collapse of fumed silica particle monolayers at the oil–water interface. *Colloids and Surfaces A: Physicochemical and Engineering Aspects*, 282, 377-386.
- Hosseini, S. M., & Tosco, T. (2013). Transport and retention of high concentrated nano-Fe/Cu particles through highly flow-rated packed sand column. *Water research*, 47(1), 326-338.
- Israelachvili, J. N. (2011). *Intermolecular and surface forces*. Academic press.
- Jaklevic, R. C., Lambe, J., Silver, A. H., & Mercereau, J. E. (1964). Quantum interference effects in Josephson tunneling. *Physical Review Letters*, 12(7), 159.
- Jambon-Puillet, E., & Protière, S. (2016). Drop floating on a granular raft. *Physical Review Fluids*, 1(5), 050501.
- Jambon-Puillet, E., Josserand, C., & Protière, S. (2017). Wrinkles, folds, and plasticity in granular rafts. *Physical Review Materials*, 1(4), 042601.
- Jang, J., Narsilio, G. A., & Santamarina, J. C. (2011). Hydraulic conductivity in spatially varying media-a pore-scale investigation. *Geophysical Journal International*, 184(3), 1167–1179. <https://doi.org/10.1111/j.1365-246X.2010.04893.x>
- Jang, J., Sun, Z., & Santamarina, J. C. (2016). Capillary pressure across a pore throat in the presence of surfactants. *Water Resources Research*, 52(12), 9586-9599.
- Johansson, C. and H. Theliander (2007). "Validation of predicted local profiles in cake filtration." *Chemical Engineering Research and Design* 85(2): 220-228.
- Jones, A. (1971). Soil Piping and Stream Channel Initiation. *Water Resources Research*, 7(3), 602–610. <https://doi.org/10.1029/WR007i003p00602>
- Juang, R.-S., Lin, S.-H., & Tsao, K.-H. (2004). Sorption of phenols from water in column systems using surfactant-modified montmorillonite. *Journal of Colloid and Interface Science*, 269(1), 46–52.
- Júnior, J. A. A., & Baldo, J. B. (2014). The behavior of zeta potential of silica suspensions. *New Journal of Glass and Ceramics*, 4(02), 29.

- Kampel, G., Goldsztein, G. H., & Santamarina, J. C. (2009). Particle transport in porous media: The role of inertial effects and path tortuosity in the velocity of the particles. *Applied Physics Letters*, 95(19), 1–4. <https://doi.org/10.1063/1.3263718>
- Kang, Z., Yeung, A., Foght, J. M., & Gray, M. R. (2008). Mechanical properties of hexadecane–water interfaces with adsorbed hydrophobic bacteria. *Colloids and Surfaces B: Biointerfaces*, 62(2), 273–279.
- Karimi, A., Fakhroueian, Z., Bahramian, A., Pour Khiabani, N., Darabad, J. B., Azin, R., & Arya, S. (2012). Wettability alteration in carbonates using zirconium oxide nanofluids: EOR implications. *Energy & Fuels*, 26(2), 1028–1036.
- Karn, B., Kuiken, T., & Otto, M. (2009). Nanotechnology and in situ remediation: a review of the benefits and potential risks. *Environmental health perspectives*, 117(12), 1813.
- Kenney, T. C., & Lau, D. (1986). Internal stability of granular filters: Reply. *Canadian Geotechnical Journal*, 23(3), 420–423. <https://doi.org/10.1139/t86-068>
- Kenouche, S., Larionova, J., Bezzi, N., Guari, Y., Bertin, N., Zanca, M., ... Morrot, G. (2014). NMR investigation of functionalized magnetic nanoparticles Fe<sub>3</sub>O<sub>4</sub> as T1–T2 contrast agents. *Powder Technology*, 255, 60–65.
- Khalifeh, M., Gardner, D., & Haddad, M. Y. (2017). Technology Trends in Cement Job Evaluation Using Logging Tools. In *SPE Abu Dhabi International Petroleum Exhibition & Conference*. Society of Petroleum Engineers.
- Khilar, K. C., & Fogler, H. S. (1983). Water Sensitivity of Sandstones. *Society of Petroleum Engineers Journal*, 23(1), 55–64. <https://doi.org/10.2118/10103-PA>
- Khin, M. M., Nair, A. S., Babu, V. J., Murugan, R., & Ramakrishna, S. (2012). A review on nanomaterials for environmental remediation. *Energy & Environmental Science*, 5(8), 8075–8109.
- Kim, J. K., Rühs, P. A., Fischer, P., & Hong, J. S. (2013). Interfacial localization of nanoclay particles in oil-in-water emulsions and its reflection in interfacial moduli. *Rheologica Acta*, 52(4), 327–335
- Klein, K. and J. C. Santamarina (2005). "Soft sediments: Wave-based characterization." *International Journal of Geomechanics* 5(2): 147–157.
- Klein, K., & Santamarina, J. C. (2000). Ferromagnetic inclusions in geomaterials: Implications. *Journal of Geotechnical and Geoenvironmental Engineering*, 126(2), 167–179.
- Kozeny, J. (1927). Über kapillare leitung des wassers im boden:(aufstieg, versickerung und anwendung auf die bewässerung), Hölder-Pichler-Tempsky.
- Kralchevsky, P. A., Ivanov, I. B., Ananthapadmanabhan, K. P., & Lips, A. (2005). On the

- thermodynamics of particle-stabilized emulsions: curvature effects and catastrophic phase inversion. *Langmuir*, 21(1), 50-63.
- Krueger, R. F. (1988). SPE 17459 An Overview of Formation Damage and Well Productivity in Oilfield Operations: An Update. *Society of Petroleum Engineers*, (February), 535–553. <https://doi.org/10.2118/10029-PA>
- Kutuzov, S., He, J., Tangirala, R., Emrick, T., Russell, T. P., & Böker, A. (2007). On the kinetics of nanoparticle self-assembly at liquid/liquid interfaces. *Physical Chemistry Chemical Physics*, 9(48), 6351-6358.
- Larsen, D. (1938). "Determining the filtration Characteristics of drilling muds." *J. Petrol. Eng.* 42-48.
- Leahy, B. D., Pocivavsek, L., Meron, M., Lam, K. L., Salas, D., Viccaro, P. J., ... & Lin, B. (2010). Geometric stability and elastic response of a supported nanoparticle film. *Physical review letters*, 105(5), 058301.
- Lecoanet, H. F., Bottero, J. Y., & Wiesner, M. R. (2004). Laboratory assessment of the mobility of nanomaterials in porous media. *Environmental science & technology*, 38(19), 5164-5169.
- Lenz, J., & Edelstein, S. (2006). Magnetic sensors and their applications. *IEEE Sensors Journal*, 6(3), 631–649.
- Levine, S., Bowen, B. D., & Partridge, S. J. (1989). Stabilization of emulsions by fine particles I. Partitioning of particles between continuous phase and oil/water interface. *Colloids and Surfaces*, 38(2), 325-343.
- Lian, L., Cao, X., Wu, Y., Sun, D., & Lou, D. (2014). A green synthesis of magnetic bentonite material and its application for removal of microcystin-LR in water. *Applied Surface Science*, 289, 245–251.
- Llandro, J., Lee, D., Mitrelias, T., Palfreyman, J. J., Hayward, T. J., Cooper, J., ... Lees, M. (2009). Magnetic measurements of suspended functionalised ferromagnetic beads under DC applied fields. *Journal of Magnetism and Magnetic Materials*, 321(14), 2129–2134.
- Lønøy, A. (2006). Making sense of carbonate pore systems. *AAPG bulletin*, 90(9), 1381-1405.
- Lozano, C., Lumay, G., Zuriguel, I., Hidalgo, R. C., & Garcimartín, A. (2012). Breaking arches with vibrations: the role of defects. *Physical review letters*, 109(6), 068001.
- Luo, D., Wang, F., Zhu, J., Cao, F., Liu, Y., Li, X., ... & Ren, Z. (2016). Nanofluid of graphene-based amphiphilic Janus nanosheets for tertiary or enhanced oil recovery: High performance at low concentration. *Proceedings of the National Academy of Sciences*, 201608135.

- Luu, X. C., Yu, J., & Striolo, A. (2013). Nanoparticles adsorbed at the water/oil interface: coverage and composition effects on structure and diffusion. *Langmuir*, 29(24), 7221-7228.
- Luyendyk, A. P. J. (1997). Processing of airborne magnetic data. *AGSO Journal of Australian Geology and Geophysics*, 17, 31–38.
- Maestro, A., Guzmán, E., Santini, E., Ravera, F., Liggieri, L., Ortega, F., & Rubio, R. G. (2012). Wettability of silica nanoparticle–surfactant nanocomposite interfacial layers. *Soft Matter*, 8(3), 837-843.
- Maestro, A., Rio, E., Drenckhan, W., Langevin, D., & Salonen, A. (2014). Foams stabilised by mixtures of nanoparticles and oppositely charged surfactants: relationship between bubble shrinkage and foam coarsening. *Soft Matter*, 10(36), 6975-6983.
- Maus, S., & Kuvshinov, A. (2004). Ocean tidal signals in observatory and satellite magnetic measurements. *Geophysical Research Letters*, 31(15).
- Maus, S., Yin, F., Lühr, H., Manoj, C., Rother, M., Rauberg, J., ... Müller, R. D. (2008). Resolution of direction of oceanic magnetic lineations by the sixth-generation lithospheric magnetic field model from CHAMP satellite magnetic measurements. *Geochemistry, Geophysics, Geosystems*, 9(7).
- Mazutis, L., Gilbert, J., Ung, W. L., Weitz, D. A., Griffiths, A. D., & Heyman, J. A. (2013). Single-cell analysis and sorting using droplet-based microfluidics. *Nature Protocols*, 8(5), 870.
- McDowell-Boyer, L. M., Hunt, J. R., & Sitar, N. (1986). Particle transport through porous media. *Water Resources Research*, 22(13), 1901-1921.
- McKinley, R. M., Bower, F. M., & Rumble, R. C. (1973). The structure and interpretation of noise from flow behind cemented casing. *Journal of Petroleum Technology*, 25(3), 329–338.
- Meeten, G. (1993). "A dissection method for analysing filter cakes." *Chemical engineering science* 48(13): 2391-2398.
- Mei, Y., Li, G., Moldenaers, P., & Cardinaels, R. (2016). Dynamics of particle-covered droplets in shear flow: unusual breakup and deformation hysteresis. *Soft matter*, 12(47), 9407-9412.
- Melanson, J. E., Baryla, N. E., & Lucy, C. A. (2001). Dynamic capillary coatings for electroosmotic flow control in capillary electrophoresis. *TrAC Trends in Analytical Chemistry*, 20(6), 365-374.
- Mendoza, A. J., Guzmán, E., Martínez-Pedrero, F., Ritacco, H., Rubio, R. G., Ortega, F., ... & Miller, R. (2014). Particle laden fluid interfaces: dynamics and interfacial rheology. *Advances in colloid and interface science*, 206, 303-319.

- Meyer, E. E., Rosenberg, K. J., & Israelachvili, J. (2006). Recent progress in understanding hydrophobic interactions. *Proceedings of the National Academy of Sciences*, 103(43), 15739–15746.
- Mockovčiaková, A., Orolínová, Z., & Škvarla, J. (2010). Enhancement of the bentonite sorption properties. *Journal of Hazardous Materials*, 180(1–3), 274–281.
- Mohajeri, M., Hemmati, M., & Shekarabi, A. S. (2015). An experimental study on using a nanosurfactant in an EOR process of heavy oil in a fractured micromodel. *Journal of Petroleum Science and Engineering*, 126, 162–173.
- Monfared, A. D., Ghazanfari, M. H., Jamialahmadi, M., & Helalizadeh, A. (2015). Adsorption of silica nanoparticles onto calcite: Equilibrium, kinetic, thermodynamic and DLVO analysis. *Chemical Engineering Journal*, 281, 334–344.
- Monteux, C., Kirkwood, J., Xu, H., Jung, E., & Fuller, G. G. (2007). Determining the mechanical response of particle-laden fluid interfaces using surface pressure isotherms and bulk pressure measurements of droplets. *Physical Chemistry Chemical Physics*, 9(48), 6344–6350.
- Muecke, T. W. (1979). Formation Fines and Factors Controlling Their Movement in Porous Media. *Journal of Petroleum Technology*, 31(2), 1979. <https://doi.org/10.2118/7007-PA>
- Mungan, N. (1965). Permeability Reduction Through Changes in pH and Salinity. *Journal of Petroleum Technology*, 17(12), 1965. <https://doi.org/10.2118/1283-PA>
- Muqem, M. A., A. E. Weekse and A. A. Al-Hajji (2012). Stuck Pipe Best Practices-A Challenging Approach to Reducing Stuck Pipe Costs. SPE Saudi Arabia Section Technical Symposium and Exhibition, Society of Petroleum Engineers.
- Nabighian, M. N., Grauch, V. J. S., Hansen, R. O., LaFehr, T. R., Li, Y., Peirce, J. W., ... Ruder, M. E. (2005). The historical development of the magnetic method in exploration. *Geophysics*, 70(6), 33ND–61ND.
- Nazari Moghaddam, R., Bahramian, A., Fakhroueian, Z., Karimi, A., & Arya, S. (2015). Comparative study of using nanoparticles for enhanced oil recovery: wettability alteration of carbonate rocks. *Energy & Fuels*, 29(4), 2111–2119.
- Niezdgodzinski, T., & Swiniarski, J. (2010). Numerical calculations of stability of spherical shells. *Mechanics and Mechanical Engineering*, 14(2), 325–337.
- Nikolov, A., & Zhang, H. (2015). The dynamics of capillary-driven two-phase flow: The role of nanofluid structural forces. *Journal of colloid and interface science*, 449, 92–101.
- Oliveira, L. C. A., Rios, R. V. R. A., Fabris, J. D., Sapag, K., Garg, V. K., & Lago, R. M. (2003). Clay–iron oxide magnetic composites for the adsorption of contaminants in



- water. *Applied Clay Science*, 22(4), 169–177.
- Outmans, H. (1958). "Mechanics of differential pressure sticking of drill collars." *Petroleum Transactions, AIME*, Vol. 213, 1958, 265-274
- Outmans, H. (1963). "Mechanics of static and dynamic filtration in the borehole." *Society of Petroleum Engineers Journal* 3(03): 236-244.
- Palmer, M. R., Nepf, H. M., Pettersson, T. J. R., & Ackerman, J. D. (2004). Observations of particle capture on a cylindrical collector: Implications for particle accumulation and removal in aquatic systems. *Limnology and Oceanography*, 49(1), 76–85.
- Palomino, A. M., & Santamarina, J. C. (2005). Fabric map for kaolinite: effects of pH and ionic concentration on behavior. *Clays and Clay minerals*, 53(3), 211-223.
- Parks, G. A., & Bruyn, P. L. De. (1962). The Zero Point of Charge of Oxides<sup>1</sup>. *The Journal of Physical Chemistry*, 66(6), 967–973.
- Pecini, E. M., & Avena, M. J. (2013). Measuring the isoelectric point of the edges of clay mineral particles: The case of montmorillonite. *Langmuir*, 29(48), 14926–14934.
- Peck, R. B. and K. Terzaghi (1948). *Soil mechanics in engineering practice*.
- Peng, Q. L., McMurry, S. M., & Coey, J. M. D. (2004). Axial magnetic field produced by axially and radially magnetized permanent rings. *Journal of Magnetism and Magnetic Materials*, 268(1–2), 165–169.
- Petosa, A. R., Jaisi, D. P., Quevedo, I. R., Elimelech, M., & Tufenkji, N. (2010). Aggregation and deposition of engineered nanomaterials in aquatic environments: role of physicochemical interactions. *Environmental science & technology*, 44(17), 6532-6549.
- Planchette, C., Lorenceau, E., & Biance, A. L. (2012). Surface wave on a particle raft. *Soft Matter*, 8(8), 2444-2451.
- Pocivavsek, L., Frey, S. L., Krishan, K., Gavrilov, K., Ruchala, P., Waring, A. J., ... & Lee, K. Y. C. (2008). Lateral stress relaxation and collapse in lipid monolayers. *Soft Matter*, 4(10), 2019-2029.
- Primdahl, F. (1979). The fluxgate magnetometer. *Journal of Physics E: Scientific Instruments*, 12(4), 241.
- Rapacchietta, A. V., & Neumann, A. W. (1977). Force and free-energy analyses of small particles at fluid interfaces: II. Spheres. *Journal of Colloid and Interface Science*, 59(3), 555-567.
- Ravera, F., Santini, E., Loglio, G., Ferrari, M., & Liggieri, L. (2006). Effect of nanoparticles on the interfacial properties of liquid/liquid and liquid/air surface

- layers. *The Journal of Physical Chemistry B*, 110(39), 19543-19551.
- Razavi, S., Cao, K. D., Lin, B., Lee, K. Y. C., Tu, R. S., & Kretzschmar, I. (2015). Collapse of particle-laden interfaces under compression: buckling vs particle expulsion. *Langmuir*, 31(28), 7764-7775.
- Reddi, L. N., Xiao, M., Hajra, M. G., & Lee, I. M. (2000). Permeability Reduction of Soil Filters due to Physical Clogging. *Journal of Geotechnical and Geoenvironmental Engineering*, 126(3), 236–246. [https://doi.org/10.1061/\(ASCE\)1090-0241\(2000\)126:3\(236\)](https://doi.org/10.1061/(ASCE)1090-0241(2000)126:3(236))
- Reid, P., G. Meeten, P. Way, P. Clark, B. Chambers and A. Gilmour (1996). Mechanisms of differential sticking and a simple well site test for monitoring and optimizing drilling mud properties. SPE/IADC Drilling Conference, Society of Petroleum Engineers.
- Ren, X-W. and Santamarina, J.C. (2017). Hydraulic Conductivity in Sediments, *J. Engineering Geology*, in print.
- Rouillac, D. (1994). *Cement evaluation logging handbook*. Éditions Technip.
- Roustaei, A., & Bagherzadeh, H. (2015). Experimental investigation of SiO<sub>2</sub> nanoparticles on enhanced oil recovery of carbonate reservoirs. *Journal of Petroleum Exploration and Production Technology*, 5(1), 27-33.
- Rühs, P. A., Böni, L., Fuller, G. G., Inglis, R. F., & Fischer, P. (2013). In-situ quantification of the interfacial rheological response of bacterial biofilms to environmental stimuli. *PloS one*, 8(11), e78524.
- Ryan, J. N., & Elimelech, M. (1996). Colloid mobilization and transport in groundwater. In *Colloids and Surfaces A: Physicochemical and Engineering Aspects* (Vol. 107, pp. 1–56). [https://doi.org/10.1016/0927-7757\(95\)03384-X](https://doi.org/10.1016/0927-7757(95)03384-X)
- Saffman, P. G., & Taylor, G. (1958, June). The penetration of a fluid into a porous medium or Hele-Shaw cell containing a more viscous liquid. In *Proceedings of the Royal Society of London A: Mathematical, Physical and Engineering Sciences* (Vol. 245, No. 1242, pp. 312-329). The Royal Society.
- Saien, J., & Gorji, A. M. (2017). Simultaneous adsorption of CTAB surfactant and magnetite nanoparticles on the interfacial tension of n-hexane–water. *Journal of Molecular Liquids*, 242, 1027–1034.
- Sakthivadivel, R., & Einstein, H. A. (1970). Clogging of porous column of spheres by sediment. *Journal of the Hydraulics Division*, 96(2), 461–472.
- Santagata, M., Dalmazzo, D., & Santagata, E. (2008). Deformation behavior of clay-water suspensions from rheological tests. In *4th International Symposium on Deformation Characteristics of Geomaterials (IS-Atlanta)*. IOS Press, Netherlands (pp. 453-459).

- Santamarina, J. C. (2003). Soil behavior at the microscale: particle forces. In *Soil behavior and soft ground construction* (pp. 25-56).
- Santamarina, J. C., A. Klein and M. A. Fam (2001). "Soils and waves: Particulate materials behavior, characterization and process monitoring." *Journal of Soils and Sediments* 1(2): 130-130.
- Santini, E., Krägel, J., Ravera, F., Liggieri, L., & Miller, R. (2011). Study of the monolayer structure and wettability properties of silica nanoparticles and CTAB using the Langmuir trough technique. *Colloids and Surfaces A: Physicochemical and Engineering Aspects*, 382(1), 186-191.
- Schlumberger (2007), Carbonate reservoirs: meeting unique challenges to maximize recovery
- Schmitz, R.M. and van Paassen, L.A. (2002). The decay of the liquid limit of clays with increasing salt concentration, *Newsletter IngeoKring*, vol. 10(1), pp. 10-14
- Schofield, A., and Wroth, P. (1968). Critical state soil mechanics.
- Schwertmann, U., & Cornell, R. M. (2007). The iron oxides. *Iron Oxides in the Laboratory: Preparation and Characterization*, 5–18.
- Scott, M. P., Johnson, R. L., Datey, A., Vandeborn, C. B., & Woodroof, R. A. (2010). Evaluating hydraulic fracture geometry from sonic anisotropy and radioactive tracer logs. In *SPE Asia Pacific Oil and Gas Conference and Exhibition*. Society of Petroleum Engineers.
- Sharma, M. M. and L. Zongming (1991). "A model for clay filter cake properties." *Colloids and surfaces* 56: 357-381.
- Sheldon, K. F. (2000). *Smoke, Dust, and Haze: Fundamentals of Aerosol Dynamics*. Oxford Univ. Press, New York.
- Sherard, J. L., Dunnigan, L. P., & Talbot, J. R. (1984). Basic properties of sand and gravel filters. *Journal of Geotechnical Engineering*, 110(6), 684–700.
- Sherwood, J. (1998). "Differential pressure sticking of drill string." *AIChE journal* 44(3): 711-721.
- Sherwood, J. and G. Meeten (1997). "The filtration properties of compressible mud filtercakes." *Journal of Petroleum Science and Engineering* 18(1): 73-81.
- Sherwood, J. D., G. H. Meeten, C. A. Farrow and N. J. Alderman (1991). "Concentration profile within non-uniform mudcakes." *Journal of the Chemical Society, Faraday Transactions* 87(4): 611-618.
- Sicard, F. X., & Striolo, A. (2017). Buckling in Armored Droplets. *Nanoscale*.

- Silva, J. B. C., & Hohmann, G. W. (1981). Interpretation of three-component borehole magnetometer data. *Geophysics*, 46(12), 1721–1731.
- Sivapullaiah, P., A. Sridharan and V. Stalin (2000). "Hydraulic conductivity of bentonite-sand mixtures." *Canadian Geotechnical Journal* 37(2): 406-413.
- Smiles, D. (1970). "A theory of constant pressure filtration." *Chemical Engineering Science* 25(6): 985-996.
- Sørensen, P. B., P. Moldrup and J. Hansen (1996). "Filtration and expression of compressible cakes." *Chemical Engineering Science* 51(6): 967-979.
- Stachowiak, J. C., Schmid, E. M., Ryan, C. J., Ann, H. S., Sasaki, D. Y., Sherman, M. B., ... & Hayden, C. C. (2012). Membrane bending by protein–protein crowding. *Nature cell biology*, 14(9), 944.
- Stamatakis, K. and C. Tien (1991). "Cake formation and growth in cake filtration." *Chemical Engineering Science* 46(8): 1917-1933.
- Stucki, J. W., Goodman, B. A., & Schwertmann, U. (2012). *Iron in soils and clay minerals* (Vol. 217). Springer Science & Business Media.
- Subramaniam, A. B., Abkarian, M., Mahadevan, L., & Stone, H. A. (2006). Mechanics of interfacial composite materials. *Langmuir*, 22(24), 10204-10208.
- Suchomel, B. J., Chen, B. M., & Allen Iii, M. B. (1998). Network Model of Flow, Transport and Biofilm Effects in Porous Media. *Transport in Porous Media*, 30, 1–23. <https://doi.org/10.1023/A:1006560705680>
- Suleimanov, B. A., Ismailov, F. S., & Veliyev, E. F. (2011). Nanofluid for enhanced oil recovery. *Journal of Petroleum Science and Engineering*, 78(2), 431-437.
- Tadros, T. F., & Lyklema, J. (1968). Adsorption of potential-determining ions at the silica-aqueous electrolyte interface and the role of some cations. *Journal of Electroanalytical Chemistry and Interfacial Electrochemistry*, 17(3), 267-275.
- Taylor, D. W. (1948). *Fundamentals of soil mechanics*, LWW.
- Theliander, H. and M. Fathi-Najafi (1996). "Simulation of the build-up of a filter cake." *Filtration & separation* 33(5): 417-421.
- Tien, C. and R. Bai (2003). "An assessment of the conventional cake filtration theory." *Chemical Engineering Science* 58(7): 1323-1336.
- Tiller, F. and W. Leu (1980). "Basic data fitting in filtration." *J. Chin. Inst. Chem. Eng* 11(61): 61-70.
- Tiller, F. M. and H. Cooper (1962). "The role of porosity in filtration: Part V. Porosity

- variation in filter cakes." *AIChE Journal* 8(4): 445-449.
- Vail, W. B., Momii, S. T., Woodhouse, R., Alberty, M. W., Peveraro, R. C. A., & Klein, J. D. (1993). Formation resistivity measurements through metal casing. In *SPWLA 34th Annual Logging Symposium*. Society of Petrophysicists and Well-Log Analysts.
- Valdes, J. R., & Santamarina, J. (2007). Particle transport in a nonuniform flow field: Retardation and clogging. *Applied Physics Letters*, 90(24). <https://doi.org/10.1063/1.2748850>
- Valdes, J. R., & Santamarina, J. C. (2006). Particle Clogging in Radial Flow: Microscale Mechanisms. *SPE Journal*, 11(2), 193–198. <https://doi.org/10.2118/88819-PA>
- Valdes, J. R., & Santamarina, J. C. (2008). Clogging: bridge formation and vibration-based destabilization. *Canadian Geotechnical Journal*, 45(2), 177–184.
- Van Olphen, H. (1977). Introduction to clay colloid chemistry. Wiley.
- Vella, D., Aussillous, P., & Mahadevan, L. (2004). Elasticity of an interfacial particle raft. *EPL (Europhysics Letters)*, 68(2), 212.
- Vipulanandan, C., Mohammed, A., & Samuel, R. G. (2017). Smart Bentonite drilling muds modified with iron oxide nanoparticles and characterized based on the electrical resistivity and rheological properties with varying magnetic field strengths and temperatures. In *Offshore Technology Conference*. Offshore Technology Conference.
- Vliegenthart, G. A., & Gompper, G. (2011). Compression, crumpling and collapse of spherical shells and capsules. *New Journal of Physics*, 13(4), 45020.
- Wakeman, R. (1981). "The formation and properties of apparently incompressible filter cakes under vacuum on downward facing surfaces." *Trans. I. Chem. Eng.* 59: 260-270.
- Wang, H., Zhao, X., Meng, W., Wang, P., Wu, F., Tang, Z., ... Giesy, J. P. (2015). Cetyltrimethylammonium bromide-coated Fe<sub>3</sub>O<sub>4</sub> magnetic nanoparticles for analysis of 15 trace polycyclic aromatic hydrocarbons in aquatic environments by ultraperformance, liquid chromatography with fluorescence detection. *Analytical Chemistry*, 87(15), 7667–7675.
- Ward, A. F. H., & Tordai, L. (1946). Time-dependence of boundary tensions of solutions I. The role of diffusion in time-effects. *The Journal of Chemical Physics*, 14(7), 453-461.
- Wasan, D. T., & Nikolov, A. D. (2003). Spreading of nanofluids on solids. *Nature*, 423(6936), 156.
- Wei, B., Li, Q., Jin, F., Li, H., & Wang, C. (2016). The potential of a novel nanofluid in enhancing oil recovery. *Energy & Fuels*, 30(4), 2882-2891.

- Wikswow, J. P. (2004). SQUIDS remain best tools for measuring brain's magnetic field. *Physics Today*, 57(2), 15.
- Williams, F. J., Neznayko, M., & Weintritt, D. J. (1953). The effect of exchangeable bases on the colloidal properties of bentonite. *The Journal of Physical Chemistry*, 57(1), 6-10.
- Wu, D., Zhu, C., Chen, Y., Zhu, B., Yang, Y., Wang, Q., & Ye, W. (2012). Preparation, characterization and adsorptive study of rare earth ions using magnetic GMZ bentonite. *Applied Clay Science*, 62, 87–93.
- Wyss, H. M., Blair, D. L., Morris, J. F., Stone, H. A., & Weitz, D. A. (2006). Mechanism for clogging of microchannels. *Physical Review E - Statistical, Nonlinear, and Soft Matter Physics*, 74(6). <https://doi.org/10.1103/PhysRevE.74.061402>
- Yazhgur, P. A., Noskov, B. A., Liggieri, L., Lin, S. Y., Loglio, G., Miller, R., & Ravera, F. (2013). Dynamic properties of mixed nanoparticle/surfactant adsorption layers. *Soft Matter*, 9(12), 3305-3314.
- Zang, D. Y., Rio, E., Langevin, D., Wei, B., & Binks, B. P. (2010). Viscoelastic properties of silica nanoparticle monolayers at the air-water interface. *The European Physical Journal E: Soft Matter and Biological Physics*, 31(2), 125-134.
- Zeinijahromi, A., Vaz, A., Bedrikovetsky, P., & Borazjani, S. (2012). Effects of fines migration on well productivity during steady state production. *Journal of Porous Media*, 15(7).
- Zhang, H., Nikolov, A., & Wasan, D. (2014). Enhanced oil recovery (EOR) using nanoparticle dispersions: underlying mechanism and imbibition experiments. *Energy & Fuels*, 28(5), 3002–3009.
- Zhang, H., Ramakrishnan, T. S., Nikolov, A., & Wasan, D. (2016). Enhanced Oil Recovery Driven by Nanofilm Structural Disjoining Pressure: Flooding Experiments and Microvisualization. *Energy & Fuels*, 30(4), 2771-2779.
- Zhang, T., Davidson, D., Bryant, S. L., & Huh, C. (2010, January). Nanoparticle-stabilized emulsions for applications in enhanced oil recovery. In SPE improved oil recovery symposium. Society of Petroleum Engineers.
- Zhang, W. X. (2003). Nanoscale iron particles for environmental remediation: an overview. *Journal of nanoparticle Research*, 5(3), 323-332.
- Zuriguel, I., Parisi, D. R., Hidalgo, R. C., Lozano, C., Janda, A., Gago, P. A., ... Clément, E. (2014). Clogging transition of many-particle systems flowing through bottlenecks. *Scientific Reports*, 4, 7324.